Applications in Engineering Science 27 (2026) 100345

Contents lists available at ScienceDirect

Applications in Engineering Science

journal homepage: www.elsevier.com/locate/apples

Dynamics of a charged Ziegler double pendulum with a nonholonomic constraint under the joint action of a dead force and a Lorentz force[☆]

Andrea Pastore[a,b,1], Joel C. Harrop[c,1], Davide Bigoni[c,1], Alfio Grillo[a,1,*]

[a] Dipartimento di Scienze Matematiche (DISMA) 'G.L. Lagrange', Politecnico di Torino, Corso Duca degli Abruzzi 24, Torino, 10129, Italy
[b] Mechano-X Institute, Applied Mechanics Laboratory, Department of Engineering Mechanics, Tsinghua University, Beijing, 100084, China
[c] Instabilities Lab, University of Trento, Via Mesiano 77, Trento, 38123, Italy

ARTICLE INFO

MSC:
00A69
37G15
37J20
37J60
70E50
70F25
74F15

Keywords:
Ziegler double pendulum
Floquet theory
Nonholonomic constraints
Flutter instability
Hopf bifurcation
Ideal solenoid
Lorentz force
Maxwell–Lodge effect
Microrobotics

ABSTRACT

A variant of the viscoelastic Ziegler double pendulum is investigated in which an electric charge is concentrated at one end of the device, at which a structural element imposing a nonholonomic constraint is attached. The obtained device is called 'charged Ziegler double pendulum' and is subjected to the influence of a dead force and a Lorentz force. The latter results from an electric field and a magnetic induction field generated by an ideal solenoid. The mechanical system models a self-propelled microrobot and, in the absence of damping, is conservative up to the energy variation induced by the Lorentz force in the case of explicitly time dependent electric field. Within this framework, two situations are analyzed: Case I, in which the device is placed inside the solenoid and experiences a Lorentz force featuring both electric and magnetic parts; Case II, in which the device is placed outside the solenoid and undergoes a Lorentz force due to the sole electric field. After determining the equilibrium for the system under study, a stability analysis is performed, and the conditions are obtained for flutter instability and Hopf-type bifurcation. In addition, the post-critical behavior of the structure is examined, focusing on the interaction between the Lorentz force and the other forces characterizing its dynamics. We investigate the possibility of revisiting, in the mechanical context provided by the Ziegler double pendulum, a phenomenology known in electromagnetism as Maxwell–Lodge effect.

1. Introduction

The double pendulum is a mechanical device that, because of its simplicity, is often employed to exemplify more complicated structures, which appear in various mechanical contexts, ranging from different branches of engineering (Kirillov, 2010; Bigoni and Noselli, 2011) to robotics (D'Annibale et al., 2015; Cazzolli et al., 2020), and biomechanics (Alouges et al., 2015).

One variant of the double pendulum is the Ziegler double pendulum (Ziegler, 1977), constructed by two homogeneous and rigid bars, of equal length ℓ and equal mass m, connected one to the other via a hinge. The masses of the bars are considered to be concentrated at their midpoints. One of the two bars is hinged on a fixed frame, and the other is subjected to a force directed parallel to it, known as a follower force. Moreover, the hinges are regarded as viscoelastic, with angular stiffness $k > 0$, and damping $c > 0$. These coefficients lump the viscoelastic properties of the structure into the joints connecting the double pendulum to the fixed frame and the two bars to each other (Ziegler, 1977; Wang et al., 2024). An important feature of the Ziegler double pendulum is that it can exhibit flutter instability due to the non-conservative nature of the follower force (Ziegler, 1977; Kirillov, 2010; Kirillov and Verhulst, 2010; Kirillov, 2013; Bigoni and Kirillov, 2019).

Cazzolli et al. (2020) introduced a modification of the Ziegler double pendulum that reproduces the same bifurcation and instability landscape as the original structure, but *under a conservative load*. In particular, one end of the first bar is pinned to a moving cart (Fig. 1); at the tip of the second bar, a nonholonomic constraint enforces orthogonality between the tip velocity and the bar. This system is designed in a way that it can allow a translational motion of the cart, when the latter is loaded with a dead force, possible through an oscillatory motion of the arms of the pendulum, a dynamics resembling

☆ This article is part of a Special issue entitled: 'APPLES_Rajagopal Legacy' published in Applications in Engineering Science.

* Corresponding author.
E-mail address: alfio.grillo@polito.it (A. Grillo).

[1] All authors contributed equally to the manuscript.

https://doi.org/10.1016/j.apples.2026.100345
Received 9 March 2026; Received in revised form 20 July 2026; Accepted 11 August 2026

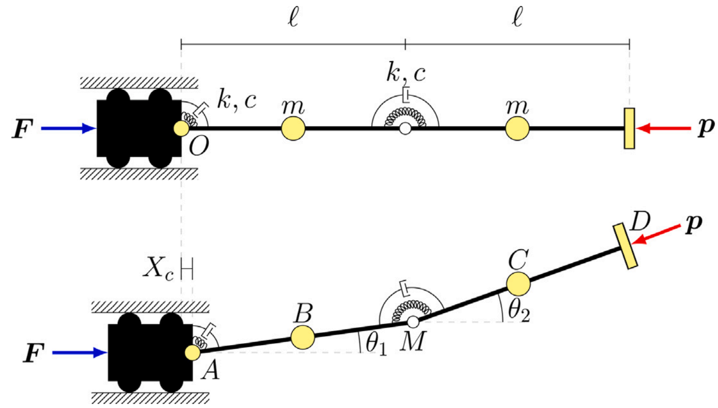

Fig. 1. Sketch of the device introduced by Cazzolli et al. (2020). Upper part: the straight configuration ($\theta_1 = \theta_2 = 0$) with the cart located on the origin O, so that $X_c = 0$. Lower part: a deformed, or displaced, configuration ($\theta_1 \neq 0, \theta_2 \neq 0$), with the cart positioned at a point differing from the origin ($X_c \neq 0$). The hinges are characterized by an elastic stiffness $k > 0$ and a viscous damping coefficient $c > 0$. The reaction force $\boldsymbol{p}$ associated with the nonholonomic constraint (the 'wheel' or the 'skate') is directed along the axis of the bar $\mathscr{B}_2$.

those of a certain family of microrobots or micro-structures used in biomechanics (Zhang et al., 2009; Brown and Poon, 2014; Alouges et al., 2015; Kim et al., 2019; Shen et al., 2023). One example of these microrobots is provided by a *'magnetic flexible filament attached to a red blood cell'*, as presented by Dreyfus et al. (2005), where the dead load plays the role of the propulsion thrust in aqueous environment at low Reynolds numbers. This device prompted the present investigation of analogous systems in microrobotics through a generalization of the loads considered by Cazzolli et al. (2020).

Microrobots for biomedical or biomechanical applications are often susceptible to electromagnetic interactions, because they feature magnetized (Dreyfus et al., 2005; Kim et al., 2019; Shen et al., 2023) or electrically polarized parts (Katzmeier and Simmel, 2023). Therefore, also Lorentz-type forces contribute to determine the overall dynamics of such devices in addition to self-propulsion (Brown and Poon, 2014) or other stimuli (Alouges et al., 2015).

Despite its fundamental role in physics, certain foundational aspects of electromagnetism have remained the subject of debate until recently. This applies, for instance, to the true role and *'physical meaning'* (Rousseaux et al., 2008) within classical electromagnetism of the vector potential $\boldsymbol{A}$, by which the magnetic induction field $\boldsymbol{B}$ is expressed as $\boldsymbol{B} = \mathrm{curl}\boldsymbol{A}$. Indeed, whereas the electric and the magnetic fields both have 'tangible' meaning, the vector potential works 'behind the scenes' of the classical theory of electromagnetism. This issue has been thoroughly investigated in a work by Rousseaux et al. (2008), who conclude that there exist effects which cannot be understood *'without the intervention of'* $\boldsymbol{A}$ (Rousseaux et al., 2008). As an example for pursuing their goals, Rousseaux et al. (2008) took the paradigmatic problem of the ideal solenoid to unveil the Maxwell–Lodge effect (Lodge, 1889). This phenomenon predicts that a current is generated in a wire wound around the solenoid in response to the electric field induced outside it by the variation in time of the vector potential (not of the magnetic induction field, which is zero outside the ideal solenoid). Although the purpose of this work is not to address the intricacies of the debate surrounding the vector potential, we embrace the viewpoint of Rousseaux et al. (2008) and apply it to our mechanical device.

In light of the above considerations, the device investigated here can be regarded as a model of an electrically charged microrobot, with dimensions comparable to those of eukaryotic cells. It consists of a continuous viscoelastic rod attached to a small mass and subjected to the Lorentz force generated by a solenoid (Zhang et al., 2009; Brown and Poon, 2014; Alouges et al., 2015; Kim et al., 2019; Shen et al., 2023). The rod is idealized as a viscoelastic double pendulum, following the approach of Cazzolli et al. (2020). Compared to that approach, two substantial differences are introduced: (i) the dead load is interpreted as a self-propulsion force; (ii) the device carries a concentrated electric charge located in the structural element imposing the nonholonomic constraint (similar problems were formulated by Maruskin et al. (2012), Pastore et al. (2024)).

Within this setting, the main objectives of our work are twofold:

1. We aim to assess the extent to which the Lorentz force modifies the results reported by Cazzolli et al. (2020) concerning stability, the onset of a Hopf-type bifurcation (e.g., a secondary Hopf or Neimark–Sacker bifurcation), and the overall dynamical behavior of the device.
2. We revisit the Maxwell–Lodge effect (Rousseaux et al., 2008) by placing it in the mechanical context of the device under study. More specifically, we show that our theoretical framework predicts a Lorentz force on the charged structural element, even when it is located outside the solenoid. This result is achieved by placing the device first inside and then outside the solenoid. This may provide a possible — albeit presently theoretical — experimental setup to detect the Maxwell–Lodge effect, based on microrobotics and serving as an alternative to the experiment by Rousseaux et al. (2008).

Outline of the work. The features of the device introduced by Cazzolli et al. (2020) are outlined in Section 2, while in Section 3 the main electromagnetic aspects of our work are addressed (Section 3.1), including the way in which they affect the Lagrangian formalism of the Ziegler double pendulum (Section 3.2). Section 3.3 presents the governing dynamic equations, incorporating the Lorentz force, while Section 3.4 addresses the corresponding static equilibrium. Based on the determination of the static equilibrium, a stability analysis is carried out for neighboring configurations (Section 4). Specifically, after linearizing the dynamic equations around equilibrium (Section 4.1), and employing Floquet theory to determine the fundamental Floquet exponents (Section 4.2), the presence of a Hopf-type bifurcation is shown (Section 4.3). Finally, Section 5 presents numerical simulations of two virtual experimental tests in the context of microrobotics.

2. Basic problem description, Lagrangian function and the 'skate' constraint

The version of the Ziegler double pendulum introduced by Cazzolli et al. (2020) and used in the present investigation consists of two homogeneous and rigid bars, denoted by $\mathscr{B}_1$ and $\mathscr{B}_2$, each of length ℓ and mass m, connected by a hinge that links the right end of $\mathscr{B}_1$ to left end of $\mathscr{B}_2$. The left end of the bar $\mathscr{B}_1$ is hinged on a cart, which is free to move along a straight line on a fixed plane. A wheel is mounted at the right end of bar $\mathscr{B}_2$, the bar acting as its axle, and rolls without slipping on a fixed plane. The non-slipping wheel is the realization of a nonholonomic constraint of the 'skate' type. Overall, the device may experience only planar motions, parallel to the fixed plane, Fig. 1.

In a fixed Cartesian reference frame with origin O and axes aligned with the orthonormal vectors $\boldsymbol{e}_1$, $\boldsymbol{e}_2$, and $\boldsymbol{e}_3$, the motion of the device is confined to the plane spanned by $\boldsymbol{e}_1$ and $\boldsymbol{e}_2$. Angles θ_1 and θ_2 measure the time-dependent inclinations of the bars $\mathscr{B}_1$ and $\mathscr{B}_2$ with the axis parallel to $\boldsymbol{e}_1$, respectively. Moreover, $X_{\rm c}$ denotes the instantaneous position, measured from O along $\boldsymbol{e}_1$, of the point of the cart to which $\mathscr{B}_1$ is hinged, Fig. 1. The Lagrangian parameters θ_1, θ_2, and $X_{\rm c}$, together with their velocities and accelerations, are collected in the arrays $q := (\theta_1, \theta_2, X_{\rm c})$, $\dot{q} := (\dot\theta_1, \dot\theta_2, \dot X_{\rm c})$, and $\ddot{q} := (\ddot\theta_1, \ddot\theta_2, \ddot X_{\rm c})$. Moreover, we introduce the following points of interest, whose spatial positions are expressed as functions of the Lagrangian coordinates as

$$x_A = \hat{x}_A(q) = (X_{\rm c}, 0, 0), \tag{1a}$$

$$x_B = \hat{x}_B(q) = (X_{\rm c} + \tfrac{1}{2}\ell\cos\theta_1, \tfrac{1}{2}\ell\sin\theta_1, 0), \tag{1b}$$

$$x_M = \hat{x}_M(q) = (X_{\rm c} + \ell\cos\theta_1, \ell\sin\theta_1, 0), \tag{1c}$$

$$x_C = \hat{x}_C(q) = (X_{\rm c} + \ell\cos\theta_1 + \tfrac{1}{2}\ell\cos\theta_2, \ell\sin\theta_1 + \tfrac{1}{2}\ell\sin\theta_2, 0), \tag{1d}$$

$$x_D = \hat{x}_D(q) = (X_{\rm c} + \ell\cos\theta_1 + \ell\cos\theta_2, \ell\sin\theta_1 + \ell\sin\theta_2, 0), \tag{1e}$$

which represent, in order: the position of the cart (point A); the midpoint of $\mathscr{B}_1$ (point B); the position of the hinge connecting $\mathscr{B}_1$ to $\mathscr{B}_2$ (point M); the midpoint of $\mathscr{B}_2$ (point C); and the position of the massless skate (point D). Accordingly, the instantaneous orientations of the bars $\mathscr{B}_1$ and $\mathscr{B}_2$ are given by the unit vectors

$$\boldsymbol{n}_1 \equiv \hat{\boldsymbol{n}}_1(q) = (\cos\theta_1)\,\boldsymbol{e}_1 + (\sin\theta_1)\,\boldsymbol{e}_2, \boldsymbol{n}_2 \equiv \hat{\boldsymbol{n}}_2(q) = (\cos\theta_2)\,\boldsymbol{e}_1 + (\sin\theta_2)\,\boldsymbol{e}_2, \tag{2}$$

while the velocities of the points of interest are

$$\boldsymbol{v}_A = \hat{\boldsymbol{v}}_A(q,\dot q) = \dot X_{\rm c}\,\boldsymbol{e}_1, \tag{3a}$$

$$\boldsymbol{v}_B = \hat{\boldsymbol{v}}_B(q,\dot q) = \left[\dot X_{\rm c} - \tfrac{1}{2}\ell\,\dot\theta_1\sin\theta_1\right]\boldsymbol{e}_1 + \left[\tfrac{1}{2}\ell\dot\theta_1\cos\theta_1\right]\boldsymbol{e}_2, \tag{3b}$$

$$\boldsymbol{v}_M = \hat{\boldsymbol{v}}_M(q,\dot q) = \left[\dot X_{\rm c} - \ell\,\dot\theta_1\sin\theta_1\right]\boldsymbol{e}_1 + \left[\ell\,\dot\theta_1\cos\theta_1\right]\boldsymbol{e}_2, \tag{3c}$$

$$\boldsymbol{v}_C = \hat{\boldsymbol{v}}_C(q,\dot q) = \left[\dot X_{\rm c} - \ell\,\dot\theta_1\sin\theta_1 - \tfrac{1}{2}\ell\,\dot\theta_2\sin\theta_2\right]\boldsymbol{e}_1 + \left[\ell\dot\theta_1\cos\theta_1 + \tfrac{1}{2}\ell\,\dot\theta_2\cos\theta_2\right]\boldsymbol{e}_2, \tag{3d}$$

$$\boldsymbol{v}_D = \hat{\boldsymbol{v}}_D(q,\dot q) = \left[\dot X_{\rm c} - \ell\,\dot\theta_1\sin\theta_1 - \ell\,\dot\theta_2\sin\theta_2\right]\boldsymbol{e}_1 + \left[\ell\,\dot\theta_1\cos\theta_1 + \ell\,\dot\theta_2\cos\theta_2\right]\boldsymbol{e}_2. \tag{3e}$$

The presence of the skate and the postulate on its motion impose a *nonholonomic constraint*: the velocity $\boldsymbol{v}_D$ of the end-point of $\mathscr{B}_2$ connected to the skate is compelled to be at all times orthogonal to $\mathscr{B}_2$ (see Cazzolli et al. (2020) for details). In the considered reference frame, this constraint is described by the relation $\boldsymbol{n}_2 \cdot \boldsymbol{v}_D = 0$, which, in terms of the Lagrangian parameters and up to the sign, reads

$$\mathcal{C} \equiv \hat{\mathcal{C}}(q,\dot q) = \dot\theta_1\ell\sin(\theta_1 - \theta_2) - \dot X_{\rm c}\cos\theta_2 = 0, \tag{4}$$

and is referred to as the *"skate' constraint'* (Cazzolli et al., 2020).

To simplify the analysis of the dynamics of the considered device, we prescribe that the mass of each bar is concentrated at its midpoint, that the cart can be modeled as a material point of mass $m_{\rm c}$, and that the skate's mass is negligible (*'massless skate'* (Cazzolli et al., 2020)). Moreover, we assume that the cart and $\mathscr{B}_1$ as well as $\mathscr{B}_1$ and $\mathscr{B}_2$ are connected to each other by means of viscoelastic spring-like elements of angular stiffness $k > 0$ and damping coefficient $c > 0$. Finally, a constant force $\boldsymbol{F} = F\boldsymbol{e}_1$ of magnitude $F > 0$ (*'dead load'* (Cazzolli et al., 2020)) is applied to the cart, while a *'follower force'* (Cazzolli et al., 2020), generated by the nonholonomic constraint, acts on the skate parallel to the bar $\mathscr{B}_2$, as shown in Fig. 1.

Under the assumptions above, the system admits the Lagrangian function (Cazzolli et al., 2020)

$$\begin{aligned}\mathcal{L}_{\rm o} \equiv \hat{\mathcal{L}}_{\rm o}(q,\dot q) =& \tfrac{1}{2}\left[\tfrac{5}{4}m\ell^2\dot\theta_1^2 + \tfrac{1}{4}m\ell^2\dot\theta_2^2 + (2m + m_{\rm c})\dot X_{\rm c}^2\right] \\ &+ \tfrac{1}{2}m\ell^2\,\dot\theta_1\dot\theta_2\cos(\theta_2 - \theta_1) - \tfrac{3}{2}m\ell\,\dot\theta_1\dot X_{\rm c}\sin\theta_1 \\ &- \tfrac{1}{2}m\ell\,\dot\theta_2\dot X_{\rm c}\sin\theta_2 \\ &- \tfrac{1}{2}k\,\theta_1^2 - \tfrac{1}{2}k(\theta_2 - \theta_1)^2 + F\,X_{\rm c},\end{aligned} \tag{5}$$

which accounts for all of the interactions to which the system is subjected, with the exception of the damping and of the nonholonomic constraint (4). Following Cazzolli et al. (2020), damping is described through the Rayleigh dissipation function

$$\mathcal{R} = \hat{\mathcal{R}}(\dot q) = \tfrac{1}{2}c\,\dot\theta_1^2 + \tfrac{1}{2}c(\dot\theta_2 - \dot\theta_1)^2, \tag{6}$$

which yields the generalized dissipative forces

$$-\frac{\partial\hat{\mathcal{R}}}{\partial\dot\theta_1}(\dot q) = -c(2\dot\theta_1 - \dot\theta_2), \qquad -\frac{\partial\hat{\mathcal{R}}}{\partial\dot\theta_2}(\dot q) = -c(\dot\theta_2 - \dot\theta_1), \qquad -\frac{\partial\hat{\mathcal{R}}}{\partial\dot X_{\rm c}}(\dot q) = 0. \tag{7}$$

The Lagrangian function $\mathcal{L}_{\rm o}$ defined by Eq. (5) describes, up to the dissipative terms, the 'original' device (whence the subscript 'o') as it was conceived by Cazzolli et al. (2020). Thus, it features the external potential $FX_{\rm c}$. Moreover, it does not depend explicitly on time.

To determine the equations of motion for the considered system, we apply the *Extended Hamilton Method*, following Lanczos (1970),

$$\delta\int_{t_{\rm in}}^{t_{\rm fin}}\hat{\mathcal{L}}_{\rm o}(q,\dot q)\,{\rm d}t = \int_{t_{\rm in}}^{t_{\rm fin}}\left(\textstyle\sum_{\alpha=1}^{3}\dfrac{\partial\hat{\mathcal{R}}}{\partial\dot q_\alpha}(\dot q)\delta q_\alpha - \sum_{\alpha=1}^{3}\mu\dfrac{\partial\hat{\mathcal{C}}}{\partial\dot q_\alpha}(q,\dot q)\,\delta q_\alpha\right){\rm d}t, \tag{8}$$

where the integral on the left-hand side is referred to as the *action functional*, $t_{\rm in}$ and $t_{\rm fin}$ denote an initial and a final instant of time, and the function of time μ on the right-hand side is a Lagrange multiplier introduced to account for the nonholonomic constraint (4), see Pars (1965), Lanczos (1970), Neimark and Fufaev (1972), Gantmacher (1975) for details.

The variation of the action functional, performed as predicted by the Hamilton Principle, and under the hypothesis $\delta q_\alpha(t_{\rm in}) = \delta q_\alpha(t_{\rm fin}) = 0$ for $\alpha = 1, 2, 3$, leads to

$$\delta\int_{t_{\rm in}}^{t_{\rm fin}}\hat{\mathcal{L}}_{\rm o}(q,\dot q)\,{\rm d}t = \int_{t_{\rm in}}^{t_{\rm fin}}\textstyle\sum_{\alpha=1}^{3}(\mathscr{E}_\alpha\hat{\mathcal{L}}_{\rm o})\,\delta q_\alpha\,{\rm d}t, \tag{9}$$

with $\mathscr{E}_\alpha\hat{\mathcal{L}}_{\rm o}$ being the Euler–Lagrange operator applied to $\hat{\mathcal{L}}_{\rm o}$,

$$\mathscr{E}_\alpha\hat{\mathcal{L}}_{\rm o} := \frac{\partial\hat{\mathcal{L}}_{\rm o}}{\partial q_\alpha}(q,\dot q) - \frac{\rm d}{{\rm d}t}\left(\frac{\partial\hat{\mathcal{L}}_{\rm o}}{\partial\dot q_\alpha}(q,\dot q)\right), \qquad \alpha = 1, 2, 3. \tag{10}$$

Then, the local form of Eq. (8) reads

$$\mathscr{E}_\alpha\hat{\mathcal{L}}_{\rm o} - \frac{\partial\hat{\mathcal{R}}}{\partial\dot q_\alpha}(\dot q) + \mu\frac{\partial\hat{\mathcal{C}}}{\partial\dot q_\alpha}(q,\dot q) = 0, \qquad \alpha = 1, 2, 3. \tag{11}$$

The third term on the left-hand side of Eq. (11) identifies, for $\alpha = 1, 2, 3$, the Lagrangian components of the reaction force due to the constraint, which are given by

$$\mu\frac{\partial\hat{\mathcal{C}}}{\partial\dot\theta_1}(q,\dot q) = \mu\ell\,\sin(\theta_1 - \theta_2) \equiv \left\{\ell\,\hat{\boldsymbol{n}}_1(q)\times\hat{\boldsymbol{p}}(q)\right\}\cdot\boldsymbol{e}_3, \tag{12a}$$

$$\mu\frac{\partial\hat{\mathcal{C}}}{\partial\dot\theta_2}(q,\dot q) \equiv \left\{\ell\,\hat{\boldsymbol{n}}_2(q)\times\hat{\boldsymbol{p}}(q)\right\}\cdot\boldsymbol{e}_3 = 0, \tag{12b}$$

$$\mu\frac{\partial\hat{\mathcal{C}}}{\partial\dot X_{\rm c}}(q,\dot q) = -\mu\cos\theta_2 \equiv \hat{\boldsymbol{p}}(q)\cdot\boldsymbol{e}_1, \tag{12c}$$

where '$\times$' denotes the cross product and $\boldsymbol{p} = \hat{\boldsymbol{p}}(q) = -\mu\boldsymbol{n}_2$ is referred to as a *follower force* (Cazzolli et al., 2020). We notice that, in a generic configuration of the device, Eq. (12a) is the (scalar) torque that the follower force exerts on $\mathscr{B}_1$ around the instantaneous position x_A of the point A. Similarly, Eq. (12b) is the *null* (scalar) torque that $\boldsymbol{p}$ exerts on $\mathscr{B}_2$, since $\boldsymbol{p}$ is parallel to $\mathscr{B}_2$ by design. Moreover, Eq. (12c) provides the $\boldsymbol{e}_1$-component of $\boldsymbol{p}$ acting on the cart.

3. Charged Ziegler double pendulum interacting with Lorentz force

With reference to the mechanical system described in the previous section and, in particular, to the Lagrangian function reported in Eq. (5), we introduce here two *major modifications*:

(1) The massless skate, concentrated at the point D (see Fig. 1), carries an *electric charge* $\mathfrak{e} \neq 0$ (it will be assumed $\mathfrak{e} > 0$ in the following);

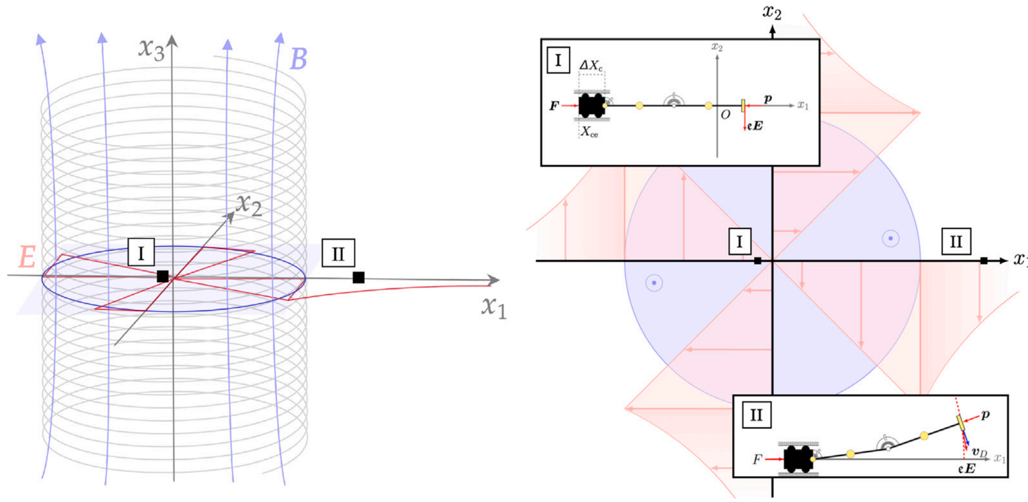

Fig. 2. Sketch of the solenoid, illustrating the electric field $\boldsymbol{E}$ (red) and the magnetic induction field $\boldsymbol{B}$ (blue). The system is shown both in a three-dimensional perspective and in a vertical cross-section, with the device positions for Case I and Case II indicated in both views. In the position referring to Case I, $\Delta X_{\mathrm{c}} := X_{\mathrm{c}0} - X_{\mathrm{ce}}$, with $X_{\mathrm{c}0}$ being the initial position of the cart. The images correspond to assuming $B_{\mathrm{h}}(t) > 0$ and $\dot{B}_{\mathrm{h}}(t) > 0$. In the zoomed-in image referring to Case II, $\mathfrak{c}\boldsymbol{E}$ is directed tangentially to the circumference centered in O and passing through D. To emphasize this, both the direction of $\mathfrak{c}\boldsymbol{E}$ and the circumference trait to which $\mathfrak{c}\boldsymbol{E}$ is tangential (dashed line in red) are *not* drawn to scale. Note that, if $\mathfrak{c}\boldsymbol{E}$ were drawn to scale, it would appear approximately parallel to the x_2-axis because the device is placed at a relatively large distance from O.

(2) A solenoid $\mathscr{S}$ as described in detail in Section 3.1 is considered and two separate cases are analyzed: the device is placed in the interior of the solenoid (*Case I*); the device is placed in the exterior of the solenoid (*Case II*).

We refer the reader to Fig. 2 for a graphical representation of the solenoid and of the device.

3.1. The paradigmatic solenoid problem and the Maxwell–Lodge effect

The solenoid $\mathscr{S}$ has virtually infinite height, axis parallel to $\boldsymbol{e}_3$, and circular cross section $\mathscr{C}$ of radius R_{s} much larger than 2ℓ. An electric current flowing in the wire constituting the solenoid generates a magnetic field $\boldsymbol{H}$, which, given the magnetic permeability of the vacuum μ_0, yields the magnetic induction field $\boldsymbol{B} = \mu_0 \boldsymbol{H}$.

Assuming appropriate regularity, the magnetic induction field $\boldsymbol{B}$ and the electric field $\boldsymbol{E}$ must fulfill the equations

$$\operatorname{div}\boldsymbol{B} = 0 \qquad \text{and} \qquad \operatorname{curl}\boldsymbol{E} = -\partial_t \boldsymbol{B}, \tag{13}$$

which constitute two of the four Maxwell equations written in local form. These conditions make it possible to express $\boldsymbol{B}$ and $\boldsymbol{E}$ in terms of a vector potential $\boldsymbol{A}$ and of a scalar potential Φ — both at least of class C^2 — through the relations $\boldsymbol{B} = \operatorname{curl}\boldsymbol{A}$ and $\boldsymbol{E} = -\operatorname{grad}\Phi - \partial_t \boldsymbol{A}$ (Felsager, 1998). Because of the differential structure of these relations, the potentials $\boldsymbol{A}$ and Φ are not unique. Indeed, for any scalar field χ at least of class C^2, $\boldsymbol{B}$ and $\boldsymbol{E}$ remain invariant under transformations of the type

$$\boldsymbol{A} \mapsto \tilde{\boldsymbol{A}} = \boldsymbol{A} + \operatorname{grad}\chi, \qquad \Phi \mapsto \tilde{\Phi} = \Phi - \partial_t \chi, \tag{14}$$

known as *gauge transformations* (Felsager, 1998). The field χ is the *generator* of the gauge transformations and allows for obtaining new forms of the vector potential and of the scalar potential, therefore also referred to as *gauge potentials*.

Although the ideal solenoid considered in this section constitutes a paradigmatic and widely studied physical problem, we review it to contextualize it within the mechanical framework of the device presented in Section 2.

The solenoid problem is grounded on the fundamental hypothesis that the magnetic induction field $\boldsymbol{B}$ is non-null and homogeneous in the interior of $\mathscr{S}$ and identically null outside it, whence

$$\boldsymbol{B}(x,t) = B_{\mathrm{h}}(t)\,\boldsymbol{e}_3, \quad \text{for } x \in \operatorname{Int}(\mathscr{S}) \quad \text{and} \quad \boldsymbol{B}(x,t) = \boldsymbol{0}, \quad \text{for } x \in \mathbb{R}^3 \setminus \mathscr{S}, \tag{15}$$

where x is a spatial point of Cartesian coordinates (x_1, x_2, x_3), enumerated coherently with $\boldsymbol{e}_1$, $\boldsymbol{e}_2$, and $\boldsymbol{e}_3$, $B_{\mathrm{h}}(t)$ is a prescribed function of time t, and $\operatorname{Int}(\mathscr{S})$ is the set of internal points of $\mathscr{S}$ (Felsager, 1998).

We notice that the vanishing of $\boldsymbol{B}$ in the exterior of an ideal solenoid is exact *'in the stationary regime'* (Rousseaux et al., 2008), although it can be maintained also under the hypothesis that the current flowing in the solenoid *'varies slowly in time'* (Rousseaux et al., 2008). The latter condition is fundamental in our setting and will be kept throughout the remainder of our work.

Within the so-called *temporal gauge* (Haller, 1987), which prescribes a vanishing scalar potential, the distribution of $\boldsymbol{B}$ given in Eq. (15) and the relation $\boldsymbol{B} = \operatorname{curl}\boldsymbol{A}$ imply (Felsager, 1998)

$$\boldsymbol{A}(x,t) = -\frac{1}{2} B_{\mathrm{h}}(t) x_2\, \boldsymbol{e}_1 + \frac{1}{2} B_{\mathrm{h}}(t) x_1\, \boldsymbol{e}_2, \qquad \Phi(x,t) = 0, \quad \text{in } \operatorname{Int}(\mathscr{S}), \tag{16a}$$

$$\boldsymbol{A}(x,t) = -\frac{1}{2} B_{\mathrm{h}}(t) R_{\mathrm{s}}^2 \frac{x_2}{x_1^2 + x_2^2}\, \boldsymbol{e}_1 + \frac{1}{2} B_{\mathrm{h}}(t) R_{\mathrm{s}}^2 \frac{x_1}{x_1^2 + x_2^2}\, \boldsymbol{e}_2, \qquad \Phi(x,t) = 0, \quad \text{in } \mathbb{R}^3 \setminus \mathscr{S}. \tag{16b}$$

Therefore, $\boldsymbol{A}$ is continuous on the boundary of the solenoid, $\partial\mathscr{S}$. Moreover, it is divergence free both in the interior and in the exterior of the solenoid, since the equality $\operatorname{div}\boldsymbol{A} = 0$ is identically satisfied both in $\operatorname{Int}(\mathscr{S})$ and in $\mathbb{R}^3 \setminus \mathscr{S}$, and it is irrotational outside the solenoid, since $\operatorname{curl}\boldsymbol{A} = \boldsymbol{0}$ in $\mathbb{R}^3 \setminus \mathscr{S}$.

It is worth recalling that the Euclidean norm of $\boldsymbol{A}(x,t)$ reads

$$\|\boldsymbol{A}(x,t)\| = \frac{1}{2}|B_{\mathrm{h}}(t)|\sqrt{x_1^2 + x_2^2} = \frac{1}{2}|B_{\mathrm{h}}(t)|\,\|\boldsymbol{r}(x)\|, \qquad \text{in } \operatorname{Int}(\mathscr{S}), \tag{17a}$$

$$\|\boldsymbol{A}(x,t)\| = \frac{1}{2}|B_{\mathrm{h}}(t)| R_{\mathrm{s}}^2 \frac{1}{\sqrt{x_1^2 + x_2^2}} = \frac{1}{2}|B_{\mathrm{h}}(t)| \frac{R_{\mathrm{s}}^2}{\|\boldsymbol{r}(x)\|}, \qquad \text{in } \mathbb{R}^3 \setminus \mathscr{S}, \tag{17b}$$

with $\boldsymbol{r}(x) = x_1 \boldsymbol{e}_1 + x_2 \boldsymbol{e}_2$, thereby increasing linearly with $\varrho = \|\boldsymbol{r}(x)\|$ until $\varrho = R_{\mathrm{s}}$, and then decreasing asymptotically towards zero as ϱ^{-1} for $\varrho > R_{\mathrm{s}}$ (Felsager, 1998; Rousseaux et al., 2008).

According to Eqs. (15), (16a), and (16b), for any open surface Σ with piecewise regular contour $\partial\Sigma$ lying on a plane that intersects transversely the solenoid, and either containing the cross section $\mathscr{C}$ of the solenoid or being equal to $\mathscr{C}$, the magnetic flux is

$$\Phi_{\mathrm{M}}(\Sigma;t)=\int_{\Sigma}\boldsymbol{B}(x,t)\cdot\boldsymbol{e}_3\,\mathrm{d}a(x)=\int_{\partial\Sigma}\boldsymbol{A}(x,t)\cdot\boldsymbol{\tau}(x)\,\mathrm{d}s(x)=B_{\mathrm{h}}(t)\pi R_{\mathrm{s}}^2, \quad (18)$$

where $\boldsymbol{\tau}(x)$ is the unit vector tangent to $\partial\Sigma$ at x. When Σ contains $\mathscr{C}$, the magnetic induction field $\boldsymbol{B}$ is null in $\Sigma\setminus\mathscr{C}$ and the first integral in Eq. (18) reduces to a surface integral over $\mathscr{C}$, whence $\Phi_{\mathrm{M}}(\Sigma;t)=B_{\mathrm{h}}(t)\pi R_{\mathrm{s}}^2$, with $\pi R_{\mathrm{s}}^2=\mathrm{Area}(\mathscr{C})$. Since $\Phi_{\mathrm{M}}(\Sigma;t)$ must be independent of $\Sigma\supseteq\mathscr{C}$, the magnetic flux can be obtained by directly computing the contour integral in Eq. (18), with $\boldsymbol{A}$ given by Eq. (16b) (Felsager, 1998).

By employing Eqs. (16a) and (16b) for the calculation of the electric field within the *temporal gauge* ($\Phi=0$), which implies $\boldsymbol{E}=-\mathrm{grad}\Phi-\partial_t\boldsymbol{A}=-\partial_t\boldsymbol{A}$, we obtain

$$\boldsymbol{E}(x,t)=\frac{1}{2}\dot{B}_{\mathrm{h}}(t)x_2\,\boldsymbol{e}_1-\frac{1}{2}\dot{B}_{\mathrm{h}}(t)x_1\,\boldsymbol{e}_2, \qquad \text{in } \mathrm{Int}(\mathscr{S}), \quad (19a)$$

$$\boldsymbol{E}(x,t)=\frac{1}{2}\dot{B}_{\mathrm{h}}(t)R_{\mathrm{s}}^2\frac{x_2}{x_1^2+x_2^2}\,\boldsymbol{e}_1-\frac{1}{2}\dot{B}_{\mathrm{h}}(t)R_{\mathrm{s}}^2\frac{x_1}{x_1^2+x_2^2}\,\boldsymbol{e}_2, \qquad \text{in } \mathbb{R}^3\setminus\mathscr{S}. \quad (19b)$$

A consequence of Eqs. (19a) and (19b) is the Lorentz force exerted on the charged skate placed at the end-point D of the bar $\mathscr{B}_2$ of the device under analysis. As mentioned at the beginning of this section, we consider the following two different cases (Fig. 2):

Case I: Device inside the solenoid. If the cross section of the solenoid is big enough to host the device, and if we assume that the motion of the device remains confined to this cross section, so that the skate does not transit through the lateral boundary of the solenoid, then the Lorentz force acting on the skate in $\mathrm{Int}(\mathscr{S})$ reads

$$\begin{aligned}\boldsymbol{F}_{\mathrm{L}}(x_D(t),t)=&\,\mathfrak{e}\,[\boldsymbol{E}(x_D(t),t)+\boldsymbol{v}_D(t)\times\boldsymbol{B}(x_D(t),t)]\\=&\left(\frac{\mathfrak{e}\dot{B}_{\mathrm{h}}(t)}{2}\,x_{D2}(t)+\mathfrak{e}B_{\mathrm{h}}(t)\dot{x}_{D2}(t)\right)\boldsymbol{e}_1\\&-\left(\frac{\mathfrak{e}\dot{B}_{\mathrm{h}}(t)}{2}\,x_{D1}(t)+\mathfrak{e}B_{\mathrm{h}}(t)\dot{x}_{D1}(t)\right)\boldsymbol{e}_2,\end{aligned} \quad (20)$$

meaning that it consists both of an electric and of a magnetic contribution. Note that the fields $\boldsymbol{E}$ and $\boldsymbol{B}$ are defined at all spatial points, and, consequently, they couple dynamically with the system through their evaluation at time t and at the spatial point $x=x_D(t)$ occupied by the material point D at the same time.

For this reason, the Lorentz force is evaluated at $x=x_D(t)$, with velocity $\boldsymbol{v}_D(t)$ at time t. The same considerations apply to the vector potential $\boldsymbol{A}$.

Case II: Device outside the solenoid. The nontrivial electric field present also in the exterior of the solenoid, as given by Eq. (19b), generates a Lorentz force acting on the charged skate, even in the case in which the skate is located outside the solenoid. In this setting, the Lorentz force in $\mathbb{R}^3\setminus\mathscr{S}$ reads

$$\begin{aligned}\boldsymbol{F}_{\mathrm{L}}(x_D(t),t)=&\,\mathfrak{e}\,\boldsymbol{E}(x_D(t),t)\\=&\frac{\mathfrak{e}\dot{B}_{\mathrm{h}}(t)R_{\mathrm{s}}^2}{2}\frac{x_{D2}(t)}{[x_{D1}(t)]^2+[x_{D2}(t)]^2}\,\boldsymbol{e}_1\\&-\frac{\mathfrak{e}\dot{B}_{\mathrm{h}}(t)R_{\mathrm{s}}^2}{2}\frac{x_{D1}(t)}{[x_{D1}(t)]^2+[x_{D2}(t)]^2}\,\boldsymbol{e}_2.\end{aligned} \quad (21)$$

Remark 1 (*The Maxwell–Lodge effect revisited*).
Eqs. (16b) and (19b) evidence that the vector potential $\boldsymbol{A}$ and the electric field $\boldsymbol{E}=-\partial_t\boldsymbol{A}$ are non-null also outside the solenoid, where the magnetic induction field $\boldsymbol{B}$ is null. This result has many important physical consequences, one of which is known as *Maxwell–Lodge effect* (Lodge, 1889): by positioning a coil of given electric conductivity around the solenoid, but not in contact with it, an electric current flowing in this coil is observed in response to the electromotive force generated by the negative of the time derivative of the magnetic flux $B_{\mathrm{h}}(t)\pi R_{\mathrm{s}}^2$, due to $\boldsymbol{B}$ inside the solenoid (Rousseaux et al., 2008). While this result is exactly the Faraday–Neumann–Lenz law, with the electromotive force being $\mathscr{E}(t):=\int_{\partial\Sigma}\boldsymbol{E}(x,t)\cdot\boldsymbol{\tau}(x)\,\mathrm{d}s(x)=-\dot{B}_{\mathrm{h}}(t)\pi R_{\mathrm{s}}^2$, and $\partial\Sigma$ representing the coil — assumed filiform —, the fact that the current in the coil occurs in the region of space in which the magnetic flux is null (but $\boldsymbol{E}=-\partial_t\boldsymbol{A}$ is non-null) constitutes the essence of the Maxwell–Lodge effect. This has generated considerable debate aiming at clarifying the role and intrinsic meaning of the vector potential $\boldsymbol{A}$ in classical physics. Although reviewing the *'paradoxes and controversies around the Maxwell–Lodge effect'* (Rousseaux et al., 2008) is out of the scopes of our work (the interested reader is referred to Rousseaux et al. (2008)), we argue here that the Maxwell–Lodge effect manifests itself also in the dynamics of the charged Ziegler double pendulum in Case II, when the pendulum is placed outside the solenoid. Indeed, because of the electric charge $\mathfrak{e}$ concentrated at the point D of the device, this point is subjected to the Lorentz force $\boldsymbol{F}_{\mathrm{L}}(x_D(t),t)$ as prescribed by Eq. (21) when the device is in $\mathbb{R}^3\setminus\mathscr{S}$. In turn, $\boldsymbol{F}_{\mathrm{L}}(x_D(t),t)$ influences the dynamics of the device and interacts with the dead load F applied to the cart, at least until the device exceeds a certain distance from the solenoid's boundary, beyond which the amplitude of $\boldsymbol{F}_{\mathrm{L}}(x_D(t),t)$, decreasing radially as $\{[x_{D1}(t)]^2+[x_{D2}(t)]^2\}^{-1/2}$, becomes negligible compared to F.

On the basis of well documented results on the gauge transformations presented in Eq. (14) (Felsager, 1998), one can choose the generators

$$\chi(x,t)=\tfrac{1}{2}B_{\mathrm{h}}(t)x_1x_2, \qquad \text{in } \mathrm{Int}(\mathscr{S}), \quad (22a)$$

$$\chi(x,t)=\tfrac{1}{2}B_{\mathrm{h}}(t)R_{\mathrm{s}}^2\arctan(x_1/x_2), \qquad \text{in } \mathbb{R}^3\setminus\mathscr{S} \text{ and for } x_2\neq 0, \quad (22b)$$

thereby moving out from the temporal gauge and switching to the transformed gauge potentials

$$\tilde{\boldsymbol{A}}(x,t)=B_{\mathrm{h}}(t)x_1\,\boldsymbol{e}_2, \qquad \tilde{\Phi}(x,t)=-\tfrac{1}{2}\dot{B}_{\mathrm{h}}(t)x_1x_2, \qquad \text{in } \mathrm{Int}(\mathscr{S}), \quad (23a)$$

$$\tilde{\boldsymbol{A}}(x,t)=\boldsymbol{0}, \qquad \tilde{\Phi}(x,t)=-\tfrac{1}{2}\dot{B}_{\mathrm{h}}(t)R_{\mathrm{s}}^2\arctan(x_1/x_2), \qquad \text{in } \mathbb{R}^3\setminus\mathscr{S} \text{ and for } x_2\neq 0 \quad (23b)$$

(note that χ has null Laplacian in the region in which it is defined). The new gauge potentials, however, yield exactly the same Lorentz forces as those reported in Eqs. (20) and (21), with the only (irrelevant) technical difference being that $\boldsymbol{B}$ and $\boldsymbol{E}$ are now to be computed as $\boldsymbol{B}=\mathrm{curl}\tilde{\boldsymbol{A}}$ and $\boldsymbol{E}=-\mathrm{grad}\,\tilde{\Phi}-\partial_t\tilde{\boldsymbol{A}}$. In particular, outside the solenoid, $\boldsymbol{E}=-\mathrm{grad}\,\tilde{\Phi}$ holds at all points $x\in\mathbb{R}^3\setminus\mathscr{S}$ such that $x_2\neq 0$. Therefore, for any open surface $\Sigma\supset\mathscr{C}$ having piecewise regular contour $\partial\Sigma$, $\boldsymbol{E}$ is undefined at both points in which $\partial\Sigma$ intersects the x_1-axis. However, since these two points constitute a set of null measure, the electromotive force $\mathscr{E}(t)=-\int_{\partial\Sigma}\mathrm{grad}\,\tilde{\Phi}(x,t)\cdot\boldsymbol{\tau}(x)\,\mathrm{d}s(x)$ remains unchanged and delivers $-\dot{B}_{\mathrm{h}}(t)\pi R_{\mathrm{s}}^2$, as is the case of the temporal gauge.

3.2. The Lagrangian function of the charged Ziegler double pendulum

The Lagrangian function of the device subjected to the additional magnetic interaction is obtained from the Lagrangian function $\mathcal{L}_{\mathrm{o}}$ in Eq. (5) by adding the generalized, velocity-dependent potential $\mathfrak{e}\boldsymbol{A}(x_D(t),t)\cdot\boldsymbol{v}_D(t)$, in which $\boldsymbol{A}$ is evaluated at time t and at the spatial point $x_D(t)$ that is instantaneously occupied by the moving charge at time t (Felsager, 1998; Pastore et al., 2024). In terms of the system's Lagrangian parameters and generalized velocities, this yields (see also Maruskin et al. (2012) for the case of the *'knife edge with a dipole moment in a magnetic field'*)

$$\mathcal{L}\equiv\hat{\mathcal{L}}(q,\dot{q},t)=\hat{\mathcal{L}}_{\mathrm{o}}(q,\dot{q})+\mathfrak{e}\left[\mathcal{A}_1(q,t)\dot{\theta}_1+\mathcal{A}_2(q,t)\dot{\theta}_2+\mathcal{A}_3(q,t)\dot{X}_{\mathrm{c}}\right], \quad (24)$$

where, for $\beta=1,2,3$, the functions $\mathcal{A}_\beta(q,t)=\frac{1}{2}B_{\mathrm{h}}(t)\mathcal{U}_\beta(q)\ell^2$ express explicitly how the device interacts with the vector potential and are defined by the auxiliary quantities

$$\mathcal{U}_1(q) := \begin{cases} 1+\cos(\theta_2-\theta_1)+(X_c/\ell)\cos\theta_1 & \text{Case I} \\ \dfrac{R_s^2}{\ell^2}\dfrac{1+\cos(\theta_2-\theta_1)+(X_c/\ell)\cos\theta_1}{[\cos\theta_1+\cos\theta_2+(X_c/\ell)]^2+[\sin\theta_1+\sin\theta_2]^2} & \text{Case II} \end{cases} \tag{25a}$$

$$\mathcal{U}_2(q) := \begin{cases} 1+\cos(\theta_2-\theta_1)+(X_c/\ell)\cos\theta_2 & \text{Case I} \\ \dfrac{R_s^2}{\ell^2}\dfrac{1+\cos(\theta_2-\theta_1)+(X_c/\ell)\cos\theta_2}{[\cos\theta_1+\cos\theta_2+(X_c/\ell)]^2+[\sin\theta_1+\sin\theta_2]^2} & \text{Case II} \end{cases} \tag{25b}$$

$$\mathcal{U}_3(q) := \begin{cases} -\dfrac{\sin\theta_1+\sin\theta_2}{\ell} & \text{Case I} \\ -\dfrac{R_s^2}{\ell^3}\dfrac{\sin\theta_1+\sin\theta_2}{[\cos\theta_1+\cos\theta_2+(X_c/\ell)]^2+[\sin\theta_1+\sin\theta_2]^2} & \text{Case II.} \end{cases} \tag{25c}$$

More in detail, it can be shown that, both in Case I and in Case II, the following identifications apply:

$$\mathcal{A}_1(q(t),t) = [\ell \boldsymbol{n}_1(t)\times \boldsymbol{A}(x_D(t),t)]\cdot \boldsymbol{e}_3, \tag{26a}$$

$$\mathcal{A}_2(q(t),t) = [\ell \boldsymbol{n}_2(t)\times \boldsymbol{A}(x_D(t),t)]\cdot \boldsymbol{e}_3, \tag{26b}$$

$$\mathcal{A}_3(q(t),t) = \boldsymbol{A}(x_D(t),t)\cdot \boldsymbol{e}_1. \tag{26c}$$

We remark that the vector potential $\boldsymbol{A}$, although having only two nonzero components, generates the three nonzero components $\mathcal{A}_1$, $\mathcal{A}_2$, and $\mathcal{A}_3$, with the first two being conjugate to the angular velocities of the bars $\dot\theta_1$ and $\dot\theta_2$, and the last one being conjugate to the linear velocity $\dot X_c$ of the cart along the $\boldsymbol{e}_1$-axis. In addition, functions $\mathcal{A}_1$, $\mathcal{A}_2$, and $\mathcal{A}_3$, explained in Eqs. (26a)–(26c), describe how the vector potential couples at each instant of time t with the configuration $q(t)$ assumed by the system as a whole at time t.

We emphasize that the charge of the skate is assumed to be sufficiently weak so that the magnetic and the electric fields that it generates can be neglected.

A major difference with respect to the work by Cazzolli et al. (2020) is that, in addition to the dead load applied to the cart, the system is also subjected to the *Lorentz force* $\boldsymbol{F}_L(x_D(t),t)$, which assumes the expression given in Eq. (20) or in Eq. (21), depending on whether the device is inside or outside the solenoid, respectively.

In Case I, and when $\boldsymbol{A}$ does not depend explicitly on time, the Lorentz force reduces to $\boldsymbol{F}_L(x_D(t),t) = \mathfrak{e}\,\boldsymbol{v}_D(t)\times \boldsymbol{B}(x_D(t))$ and, because of the constraint (4), it remains parallel to the bar $\mathscr{B}_2$, and thus to the follower force $\boldsymbol{p} = -\mu \boldsymbol{n}_2$, at all times. In addition, the Lorentz force vanishes whenever $\boldsymbol{v}_D(t)$ is null.

In Case II, the Lorentz force features solely the purely electric contribution, which is due to the explicit time dependence of $\boldsymbol{A}$, that is, $\boldsymbol{F}_L(x_D(t),t) = \mathfrak{e}\boldsymbol{E}(x_D(t),t) = -\mathfrak{e}\,\partial_t \boldsymbol{A}(x_D(t),t)$. Therefore, if $\boldsymbol{A}$ is assumed to not be explicitly dependent on time, then the Lorentz force vanishes identically.

3.3. Dynamic equations

If the dynamic equations (11), featuring the Lagrangian function $\hat{\mathcal{L}}_o$, are written explicitly, they lead to the set of equations presented by Cazzolli et al. (2020). In our framework, however, since electromagnetic interactions are considered, the dynamic equations follow from the Lagrangian function $\hat{\mathcal{L}}$ expressed in Eq. (24). They read

$$\mathscr{E}_\alpha \hat{\mathcal{L}} - \frac{\partial \hat{\mathcal{R}}}{\partial \dot q_\alpha}(\dot q) + \mu \frac{\partial \hat{\mathcal{C}}}{\partial \dot q_\alpha}(q,\dot q) = 0, \qquad \alpha = 1,2,3, \tag{27}$$

where, as in Eq. (11), the contributions $-\partial_{\dot q_\alpha}\hat{\mathcal{R}}(\dot q)$ and $\mu\,\partial_{\dot q_\alpha}\hat{\mathcal{C}}(q,\dot q)$ identify the dissipative generalized forces associated with damping and the reaction forces due to the nonholonomic *"skate' constraint'* (Cazzolli et al., 2020), respectively.

Before deriving the new Euler–Lagrange equations, we note that the Euler–Lagrange operator applied to $\hat{\mathcal{L}}$ produces

$$\mathscr{E}_\alpha \hat{\mathcal{L}} = \mathscr{E}_\alpha \hat{\mathcal{L}}_o + \mathfrak{e}\sum_{\beta=1}^3 \mathcal{F}_{\alpha\beta}\,\dot q_\beta + \mathfrak{e}\,\mathcal{E}_\alpha, \qquad \alpha = 1,2,3, \tag{28}$$

where the quantities $\mathcal{F}_{\alpha\beta}$ and $\mathcal{E}_\alpha$ are defined as

$$\mathcal{F}_{\alpha\beta} := \frac{\partial \mathcal{A}_\beta}{\partial q_\alpha} - \frac{\partial \mathcal{A}_\alpha}{\partial q_\beta}, \qquad \mathcal{E}_\alpha := -\frac{\partial \mathcal{A}_\alpha}{\partial t}, \qquad \alpha,\beta = 1,2,3, \tag{29}$$

and represent, in terms of the Lagrangian parameters selected, the components of the *generalized Faraday tensor* and of the *generalized electric field*, respectively. From the discussion in Section 3.1, in which the electric and the magnetic contributions of the Lorentz force have been analyzed in Cartesian coordinates, it follows that the magnetic contribution is active only in the interior of the solenoid. Accordingly, the equations of motion either include or exclude the magnetic contribution of the Lorentz force, depending on whether the device is located inside or outside the solenoid (Case I and Case II, respectively). Since this result must be consistently described when the device is analyzed in terms of the components of the generalized Faraday tensor and of the generalized electric field, defined by Eq. (29), the quantities $\mathcal{F}_{\alpha\beta}$ must vanish identically in Case II, when the device moves outside the solenoid.

Specifically, the generalized Faraday tensor has components

$$\mathcal{F}_{12} = -\ell^2 B_h(t)\sin(\theta_1-\theta_2), \quad \mathcal{F}_{13} = -\ell B_h(t)\cos\theta_1, \quad \mathcal{F}_{23} = -\ell B_h(t)\cos\theta_2, \quad \text{Case I} \tag{30a}$$

$$\mathcal{F}_{12} = 0, \quad \mathcal{F}_{13} = 0, \quad \mathcal{F}_{23} = 0, \quad \text{Case II} \tag{30b}$$

with $\mathcal{F}_{\alpha\beta} = -\mathcal{F}_{\beta\alpha}$ for $\alpha,\beta = 1,2,3$, while the generalized electric field has components

$$\mathcal{E}_\alpha \equiv -\partial_t \mathcal{A}_\alpha = -\tfrac{1}{2}\dot B_h(t)\,\mathcal{U}_\alpha(q)\,\ell^2, \qquad \alpha = 1,2,3, \tag{31}$$

where functions $\mathcal{U}_\alpha(q)$ are given in Eqs. (25a)–(25c) both for Case I and for Case II.

Finally, upon introducing the components of the generalized Lorentz force

$$\mathfrak{F}_{L\alpha} := \mathfrak{e}\sum_{\beta=1}^3 \mathcal{F}_{\alpha\beta}\,\dot q_\beta + \mathfrak{e}\,\mathcal{E}_\alpha, \qquad \alpha = 1,2,3, \tag{32}$$

the dynamic equations (27) read

$$\mathscr{E}_\alpha \hat{\mathcal{L}}_o - \frac{\partial \hat{\mathcal{R}}}{\partial \dot q_\alpha}(\dot q) + \mu \frac{\partial \hat{\mathcal{C}}}{\partial \dot q_\alpha}(q,\dot q) + \mathfrak{F}_{L\alpha} = 0, \qquad \alpha = 1,2,3, \tag{33}$$

and, in explicit form, they become

$$\begin{aligned} &\tfrac{5}{4}m\ell^2\ddot\theta_1 + \tfrac{1}{2}m\ell^2\cos(\theta_1-\theta_2)\ddot\theta_2 - \tfrac{3}{2}m\ell(\sin\theta_1)\ddot X_c + \tfrac{1}{2}m\ell^2\sin(\theta_1-\theta_2)\dot\theta_2^2 \\ &= -k(2\theta_1-\theta_2) - c(2\dot\theta_1-\dot\theta_2) + \mu\ell\sin(\theta_1-\theta_2) + \mathfrak{F}_{L1}, \end{aligned} \tag{34a}$$

$$\begin{aligned} &\tfrac{1}{2}m\ell^2\cos(\theta_1-\theta_2)\ddot\theta_1 + \tfrac{1}{4}m\ell^2\ddot\theta_2 - \tfrac{1}{2}m\ell(\sin\theta_2)\ddot X_c - \tfrac{1}{2}m\ell^2\sin(\theta_1-\theta_2)\dot\theta_1^2 \\ &= -k(\theta_2-\theta_1) - c(\dot\theta_2-\dot\theta_1) + \mathfrak{F}_{L2}, \end{aligned} \tag{34b}$$

$$\begin{aligned} &-\tfrac{3}{2}m\ell(\sin\theta_1)\ddot\theta_1 - \tfrac{1}{2}m\ell(\sin\theta_2)\ddot\theta_2 + M\ddot X_c - \tfrac{3}{2}m\ell(\cos\theta_1)\dot\theta_1^2 - \tfrac{1}{2}m\ell(\cos\theta_2)\dot\theta_2^2 \\ &= -\mu\cos\theta_2 + F + \mathfrak{F}_{L3}, \end{aligned} \tag{34c}$$

where the total mass $M := 2m + m_c$ is introduced. The explicit expressions for the generalized components of the Lorentz force are:

$$\mathfrak{F}_{L1} = \begin{cases} -\tfrac{1}{2}\mathfrak{e}\dot B_h(t)\mathcal{U}_1(q)\ell^2 - \mathfrak{e}B_h(t)[\sin(\theta_1-\theta_2)\dot\theta_2 + (\cos\theta_1)(\dot X_c/\ell)]\ell^2 & \text{Case I} \\ -\tfrac{1}{2}\mathfrak{e}\dot B_h(t)\mathcal{U}_1(q)\ell^2 & \text{Case II} \end{cases} \tag{35a}$$

$$\mathfrak{F}_{L2} = \begin{cases} -\tfrac{1}{2}\mathfrak{e}\dot B_h(t)\mathcal{U}_2(q)\ell^2 + \mathfrak{e}B_h(t)[\sin(\theta_1-\theta_2)\dot\theta_1 - (\cos\theta_2)(\dot X_c/\ell)]\ell^2 & \text{Case I} \\ -\tfrac{1}{2}\mathfrak{e}\dot B_h(t)\mathcal{U}_2(q)\ell^2 & \text{Case II} \end{cases} \tag{35b}$$

$$\mathfrak{F}_{L3} = \begin{cases} -\tfrac{1}{2}\mathfrak{e}\dot B_h(t)\mathcal{U}_3(q)\ell^2 + \mathfrak{e}B_h(t)[(\cos\theta_1)\dot\theta_1 + (\cos\theta_2)\dot\theta_2]\ell & \text{Case I} \\ -\tfrac{1}{2}\mathfrak{e}\dot B_h(t)\mathcal{U}_3(q)\ell^2 & \text{Case II.} \end{cases} \tag{35c}$$

We emphasize that the magnetic part of $\mathfrak{F}_{L2}$ in Eq. (35b) (i.e., the one featuring $B_h(t)$) is zero also in Case I since the terms in square brackets return the constraint (4). This is because the magnetic part of the Lorentz force $\mathfrak{e}\, \boldsymbol{v}_D \times \boldsymbol{B}$ is parallel to the bar $\mathscr{B}_2$, of unit vector $\boldsymbol{n}_2$, and also to the follower force $\boldsymbol{p}$, as explained at the end of Section 2.

Eqs. (34a)–(34c) are to be solved together with the constraint (4), which we differentiate with respect to time and turn into the second-order differential equation

$$-\ell \sin(\theta_1 - \theta_2)\ddot{\theta}_1 + (\cos\theta_2)\ddot{X}_c = \dot{\theta}_2 \dot{X}_c \sin\theta_2 + \ell\dot{\theta}_1 \cos(\theta_1 - \theta_2)(\dot{\theta}_1 - \dot{\theta}_2). \quad (36)$$

Eq. (36), obtained by changing sign to the time derivative of Eq. (4), is necessary to apply the Schur complement technique to the system (34a)–(34c) and (36) (for details, see Zampieri (2000), Pastore et al. (2024) and Section C of the Supplementary Material; the sign change is motivated by convenience in the construction of the Schur matrix).

Alongside the elastic and viscous forces featuring in the right-hand sides of Eqs. (34a)–(34c), the additional generalized Lorentz forces $\mathfrak{F}_{L1}$, $\mathfrak{F}_{L2}$ and $\mathfrak{F}_{L3}$ are present, and, coherently with Eqs. (12a)–(12c), the following identifications apply

$$\mathfrak{F}_{L1} = [\ell \boldsymbol{n}_1(t) \times \boldsymbol{F}_L(x_D(t), t)] \cdot \boldsymbol{e}_3, \quad (37a)$$

$$\mathfrak{F}_{L2} = [\ell \boldsymbol{n}_2(t) \times \boldsymbol{F}_L(x_D(t), t)] \cdot \boldsymbol{e}_3, \quad (37b)$$

$$\mathfrak{F}_{L3} = \boldsymbol{F}_L(x_D(q), t) \cdot \boldsymbol{e}_1. \quad (37c)$$

Eqs. (37a) and (37b) are the torques generated by the Lorentz force acting on the bars $\mathscr{B}_1$ and $\mathscr{B}_2$, respectively, while Eq. (37c) is the component of the Lorentz force acting on the cart.

3.4. Determination of static equilibrium

To study the static equilibrium of the system, we consider an initial instant of time t_0 at which the system occupies the configuration $q(t_0) = q_0$, with null velocity $\dot{q}(t_0) = (0,0,0)$, and, for $t > t_0$, we look for solutions to Eqs. (34a)–(34c) of the type $q(t) = q_e := (\theta_{1e}, \theta_{2e}, X_{ce}) \equiv q_0$, satisfying $\dot{q}(t) = (0,0,0)$ and

$$-\mu_e \ell \sin(\theta_{1e} - \theta_{2e}) = -\tfrac{1}{2}\mathfrak{e}\dot{B}_h(t)\mathcal{U}_1(q_e)\ell^2 - k(2\theta_{1e} - \theta_{2e}), \quad (38a)$$

$$0 = -\tfrac{1}{2}\mathfrak{e}\dot{B}_h(t)\mathcal{U}_2(q_e)\ell^2 - k(\theta_{2e} - \theta_{1e}), \quad (38b)$$

$$\mu_e \cos\theta_{2e} = -\tfrac{1}{2}\mathfrak{e}\dot{B}_h(t)\mathcal{U}_3(q_e)\ell^2 + F, \quad (38c)$$

where μ_e is the (still unknown) Lagrange multiplier at equilibrium (Gantmacher, 1975, p. 25).

Note that the nonholonomic constraint (4) is trivially satisfied when the generalized velocities are all set equal to zero. For this reason, the number of equations characterizing equilibrium reduces to the three force balances (38a)–(38c), which, however, still feature the four unknowns θ_{1e}, θ_{2e}, X_{ce}, and μ_e. We also notice that the torques due to the magnetic part of the Lorentz force are not present in Eqs. (38a)–(38c) because the velocities are set equal to zero.

Assuming $\theta_{1e} = \theta_{2e} = \theta_e$, Eqs. (38a)–(38c) become

$$0 = -\tfrac{1}{2}\mathfrak{e}\dot{B}_h(t)\mathcal{U}_1(q_e)\ell^2 - k\theta_e, \quad (39a)$$

$$0 = -\tfrac{1}{2}\mathfrak{e}\dot{B}_h(t)\mathcal{U}_2(q_e)\ell^2, \quad (39b)$$

$$\mu_e \cos\theta_e = -\tfrac{1}{2}\mathfrak{e}\dot{B}_h(t)\mathcal{U}_3(q_e)\ell^2 + F, \quad (39c)$$

with $\mathcal{U}_1(q_e) = \mathcal{U}_2(q_e)$. Thus, equilibrium in the general case in which $\dot{B}_h(t)$ is different from zero requires from Eq. (39b) $\mathcal{U}_2(q_e) = 0$, which may hold true only in Case I. Hence, we find

$$\mathcal{U}_2(q_e) = 0 \quad \Rightarrow \quad 2 + \frac{X_{ce}}{\ell}\cos\theta_e = 0 \quad \Rightarrow \quad X_{ce} = -\frac{2\ell}{\cos\theta_e}. \quad (40)$$

Moreover, since $\mathcal{U}_1(q_e)$ vanishes too, Eq. (39a) yields the more stringent condition

$$\theta_e = 0. \quad (41)$$

This implies that $\mathcal{U}_3(q_e)$ also vanishes identically, thereby yielding the force balance

$$\mu_e = F. \quad (42)$$

By gathering the results (40)–(42), we find

$$q_e = (\theta_{1e}, \theta_{2e}, X_{ce}) = (0, 0, -2\ell), \qquad \mu_e = F. \quad (43)$$

The condition $\mathcal{U}_1(q_e) = \mathcal{U}_2(q_e) = 0$ for nonzero $\dot{B}_h(t)$ amounts to placing the device in a configuration in which the electric part $\mathfrak{e}\boldsymbol{E}$ of the Lorentz force acting on the massless skate is null (see Fig. 3(a)). Indeed, given the expression $\mathfrak{e}\boldsymbol{E}(\hat{x}_D(q_e), t) = -\frac{1}{2}\mathfrak{e}\dot{B}_h(t)(X_{ce} + 2\ell)\boldsymbol{e}_2$, the requirement of the vanishing of this force means that the skate has to occupy the origin of the considered reference frame, where $\hat{x}_D(q_e) = 0$ and, thus, $X_{ce} = -2\ell$.

We note that no equilibrium configuration exists in Case II, since, when the device is outside the solenoid, Eq. (39b) cannot be satisfied unless the condition $\dot{B}_h(t) = 0$ is considered for all $t \geq t_0$, which means that B_h is constant in time. On the other hand, if $\dot{B}_h(t) = 0$ for all $t \geq t_0$, every triple $(\theta_1(t), \theta_2(t), X_c(t)) = (0, 0, X_{ce})$, with arbitrary $X_{ce} > R_s$, satisfies the equilibrium conditions.

See Fig. 3 for a graphical depiction of the device in the four configurations of interest inside the solenoid (Case I).

Remark 2 (*One static equilibrium configuration extracted from the 'manifold' (Cazzolli et al., 2020)*).

The configuration q_e determined in Eq. (43) is *one* particular configuration of the manifold $\{(0, 0, X_{ce}) : X_{ce} \in \mathbb{R}\}$ of equilibrium configurations obtained by Cazzolli et al. (2020) in the absence of magnetic interactions. Eq. (43) constitutes an important difference from the work by Cazzolli et al. (2020). In our setting, indeed, X_c cannot be arbitrary, since the equilibrium configuration is obtained by imposing the additional condition of null electric part of the Lorentz force acting on the skate. However, we retrieve the same equilibrium manifold as Cazzolli et al. (2020) if we assume that B_h is independent of time, which implies $\dot{B}_h(t) = 0$ at all times. Indeed, under the hypothesis of time-independent B_h, Eq. (39a) returns $\theta_e = 0$, Eq. (39b) is trivially satisfied (thus, there is no counterpart of Eq. (40) to determine X_{ce}, which remains indeterminate), and Eq. (39c) reduces to $\mu_e = F$.

4. Stability analysis: flutter instability and bifurcations in Case I

In this section, we carry out a stability analysis of the system described by Eqs. (34a)–(34c) and (36). To this end, since we need to perturb the system from a static equilibrium configuration, we restrict our study to Case I only.

For the methodologies used hereafter, we refer to Neimark and Fufaev (1972), Ziegler (1977), Guskov and Thouverez (2012), Bentvelsen and Lazarus (2018), Cazzolli et al. (2020), Guillot et al. (2020), Agúndez et al. (2021).

Before proceeding with the stability analysis, we notice that Eqs. (34a)–(34c) feature together six physical parameters to which we add the magnitude F of the dead load applied to the cart and the amplitude $B_M := \max_t |B_h(t)|$ of the $\boldsymbol{e}_3$-component $B_h(t)$ of the magnetic induction field (hereafter, B_h is assumed to be a function defined over a closed and bounded interval of time):

$$\mathcal{P} := \{m_c;\ m, c, k, \ell;\ \mathfrak{e};\ F, B_M\}. \quad (44)$$

Dimensionless quantities are introduced via the mappings

$$X_c \mapsto \frac{X_c}{\ell}, \quad t \mapsto \frac{t}{\sqrt{m\ell^2/k}}, \quad \mu \mapsto \frac{\mu\ell}{k}, \quad F \mapsto \frac{F\ell}{k}, \quad B_M \mapsto \frac{\mathfrak{e}B_M\ell}{\sqrt{mk}}, \quad (45a)$$

$$M \mapsto \frac{M}{m}, \quad c \mapsto \frac{c}{\ell\sqrt{mk}}. \quad (45b)$$

For simplicity, we do not introduce additional notation to indicate the dimensionless quantities in Eqs. (45a) and (45b). Rather, from

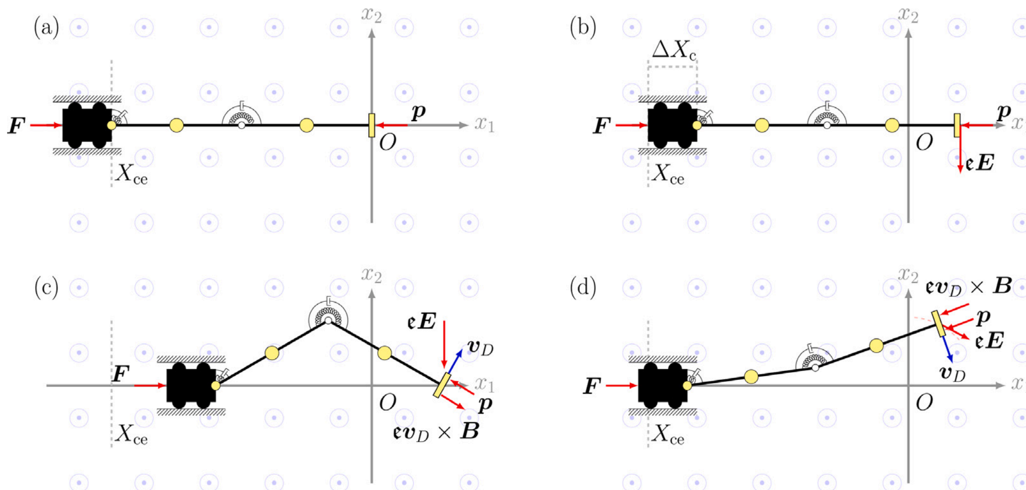

Fig. 3. Body diagram showing the forces acting on the device in the case in which the radius $R_s > 2\ell$ of the solenoid is sufficiently large to fully host the device and its motion (Case I). Four scenarios are depicted: (a) the device is in the static equilibrium configuration determined in Eq. (43); (b) although the device is in a configuration with initial null velocities, such a configuration is not of equilibrium because the Lorentz force, composed only by its electric contribution, produces a non-zero torque, thereby triggering the motion; (c and d) in each case the device is in a deformed configuration with nonzero velocities and, thus, the magnetic part of the Lorentz force acts on the device in addition to the electric part. In particular, we emphasize that, while $\mathfrak{e}\,\boldsymbol{v}_D \times \boldsymbol{B}$ is parallel to $\boldsymbol{n}_2$ by construction, $\mathfrak{e}\boldsymbol{E}$ has to be tangential to the circumference instantaneously centered in the origin and passing through $x_D(t)$ (indeed, $\boldsymbol{E}(x_D(t), t)$ is proportional to $\boldsymbol{e}_3 \times \boldsymbol{r}(x_D(t))$, with $\boldsymbol{r}(x_D(t)) = x_{D1}(t)\,\boldsymbol{e}_1 + x_{D2}(t)\,\boldsymbol{e}_2$).

here on, we simply rename them as $X_{\rm c}$, t, μ, F, $B_{\rm M}$, M, and c, and we differentiate with respect to the dimensionless time variable. We emphasize that dimensionless variables are used throughout Section 4, while physical dimensions are restored in Section 5 to contextualize the numerical results.

4.1. Linearization of the equations governing the dynamics of the structure

To perform the stability analysis in a neighborhood of the pair $(q_{\rm e}; \mu_{\rm e}) = (0, 0, -2; F)$, we consider small *perturbations* around $q_{\rm e}$ and $\mu_{\rm e}$. This is achieved by introducing the homotopies $\tilde{q}$ and $\tilde{\mu}$, which define the perturbed configuration $\tilde{q}(t, \varepsilon)$ and the perturbed Lagrange multiplier $\tilde{\mu}(t, \varepsilon)$, with ε being a smallness parameter, and by requiring them to comply with the conditions $\tilde{q}(t, 0) = q_{\rm e}$ and $\tilde{\mu}(t, 0) = \mu_{\rm e}$. We assume $\tilde{q}$ and $\tilde{\mu}$ to be at least C^2 functions of their arguments.

The first-order expansions of $\tilde{q}$ and $\tilde{\mu}$ around $\varepsilon = 0$ and for all t can be written as:

$$\tilde{q}(t, \varepsilon) = q_{\rm e} + \eta(t)\varepsilon + o(\varepsilon), \quad \varepsilon \to 0, \tag{46a}$$

$$\tilde{\mu}(t, \varepsilon) = \mu_{\rm e} + \varrho(t)\varepsilon + o(\varepsilon), \quad \varepsilon \to 0, \tag{46b}$$

with $\eta(t) := \partial_\varepsilon \tilde{q}(t, 0)$ and $\varrho(t) := \partial_\varepsilon \tilde{\mu}(t, 0)$. In the following, we set $\eta := (\vartheta_1, \vartheta_2, x_{\rm c})$.

By substituting Eqs. (46a) and (46b) into the dimensionless form of Eqs. (34a)–(34c) and (36), and dropping all the terms of order higher than the first in ε, we obtain the dynamic equations linearized around $q_{\rm e}$ and $\mu_{\rm e}$:

$$\tfrac{5}{4}\ddot{\vartheta}_1 + \tfrac{1}{2}\ddot{\vartheta}_2 + c\,(2\dot{\vartheta}_1 - \dot{\vartheta}_2) + (2\vartheta_1 - \vartheta_2) - F(\vartheta_1 - \vartheta_2) + B_{\rm h}(t)\dot{x}_{\rm c} + \tfrac{1}{2}\dot{B}_{\rm h}(t)x_{\rm c} = 0, \tag{47a}$$

$$\tfrac{1}{2}\ddot{\vartheta}_1 + \tfrac{1}{4}\ddot{\vartheta}_2 + c\,(\dot{\vartheta}_2 - \dot{\vartheta}_1) + (\vartheta_2 - \vartheta_1) + B_{\rm h}(t)\dot{x}_{\rm c} + \tfrac{1}{2}\dot{B}_{\rm h}(t)x_{\rm c} = 0, \tag{47b}$$

$$M\ddot{x}_{\rm c} + \varrho - B_{\rm h}(t)(\dot{\vartheta}_1 + \dot{\vartheta}_2) - \tfrac{1}{2}\dot{B}_{\rm h}(t)(\vartheta_1 + \vartheta_2) = 0, \tag{47c}$$

$$\ddot{x}_{\rm c} = 0, \tag{47d}$$

where $B_{\rm h}(t)$ and $\dot{B}_{\rm h}(t)$ are dimensionless functions of the dimensionless time.

Remark 3 (*$\dot{B}_h(t)$ couples the translational and the rotational degrees of freedom*)**.**

In the linearized dynamic Eqs. (47a)–(47c), $\dot{B}_{\rm h}(t)$ makes it impossible to decouple $x_{\rm c}$ from ϑ_1 and ϑ_2. This can be seen by substituting the condition $\ddot{x}_{\rm c} = 0$ in Eq. (47c), and the condition $\dot{x}_{\rm c} = 0$ (representing the linearization of the constraint (4)) in Eqs. (47a) and (47b), because the term $\frac{1}{2}\dot{B}_{\rm h}(t)x_{\rm c}$ does not cancel, as it represents the electric part of the Lorentz force. This is another difference with the case studied by Cazzolli et al. (2020), in which the framework considered allows for decoupling the dynamics of the cart from the dynamics of the double pendulum. Note that the decoupling is recovered also in our study when the electric part of the Lorentz force vanishes, so that $\dot{B}_{\rm h}(t) = 0$ for $t \geq t_0$.

Following Neimark and Fufaev (1972), upon introducing the 3×1 array $\upeta = \{\vartheta_1 \;\; \vartheta_2 \;\; x_{\rm c}\}^{\rm T}$ and the 1×1 array $\uprho = \{\varrho\}$, Eqs. (47a)–(47d) can be recast in matrix formalism as

$$\mathsf{M}_{\rm e}\ddot{\upeta} + \left[\mathsf{C}_{\rm e} + B_{\rm h}\mathsf{L}_{\rm e}\right]\dot{\upeta} + \left[\mathsf{K}_{\rm e} + F\mathsf{G}_{\rm e} + \tfrac{1}{2}\dot{B}_{\rm h}\mathsf{L}_{\rm e}\right]\upeta - \mathsf{A}_{\rm e}^{\rm T}\uprho = 0, \tag{48a}$$

$$-\mathsf{A}_{\rm e}\ddot{\upeta} = 0, \tag{48b}$$

where $\mathsf{M}_{\rm e}$, $\mathsf{K}_{\rm e}$, and $\mathsf{C}_{\rm e}$ represent the mass, stiffness, and damping matrices, respectively, $\mathsf{G}_{\rm e}$ is an auxiliary (singular) matrix introduced to account for the force F, $\mathsf{A}_{\rm e}$ is the constraint matrix, while $\mathsf{L}_{\rm e}$ is the matrix accounting for the contributions due to the Lorentz force. These matrices read

$$\mathsf{M}_{\rm e} := \begin{bmatrix} \frac{5}{4} & \frac{1}{2} & 0 \\ \frac{1}{2} & \frac{1}{4} & 0 \\ 0 & 0 & M \end{bmatrix}, \quad \mathsf{K}_{\rm e} := \begin{bmatrix} 2 & -1 & 0 \\ -1 & 1 & 0 \\ 0 & 0 & 0 \end{bmatrix}, \quad \mathsf{C}_{\rm e} := \begin{bmatrix} 2c & -c & 0 \\ -c & c & 0 \\ 0 & 0 & 0 \end{bmatrix}, \tag{49a}$$

$$\mathsf{G}_{\rm e} := \begin{bmatrix} -1 & 1 & 0 \\ 0 & 0 & 0 \\ 0 & 0 & 0 \end{bmatrix}, \quad \mathsf{A}_{\rm e} := \begin{bmatrix} 0 & 0 & -1 \end{bmatrix}, \quad \mathsf{L}_{\rm e} := \begin{bmatrix} 0 & 0 & 1 \\ 0 & 0 & 1 \\ -1 & -1 & 0 \end{bmatrix}. \tag{49b}$$

Remark 4 (*Faraday tensor in matrix formalism and its coupling with C_e, K_e, and FG_e*).

In the linearized setting, the dead load F, although being applied to the cart, influences the double pendulum through the introduction of the 'apparent' stiffness matrix $F\mathsf{G}_\mathrm{e}$, referred to as *'geometric stiffness matrix'* in the literature (Bigoni and Kirillov, 2019), which adds to the elastic stiffness matrix K_e. Similarly, B_h and $\dot{B}_\mathrm{h}$ yield the 'apparent' damping matrix $B_\mathrm{h}\mathsf{L}_\mathrm{e}$ and the additional 'apparent' stiffness matrix $\frac{1}{2}\dot{B}_\mathrm{h}\mathsf{L}_\mathrm{e}$, both due to the linearization of the Lorentz force. It is worth noticing that $B_\mathrm{h}\mathsf{L}_\mathrm{e}$ is the matrix associated with the generalized Faraday tensor, evaluated at the equilibrium configuration q_e in dimensionless form and in the case in which the device is inside the solenoid (cfr. Eq. (30a)). Analogously, $\frac{1}{2}\dot{B}_\mathrm{h}\mathsf{L}_\mathrm{e}$ is the matrix associated with the electric contribution $\frac{1}{2}\dot{B}_\mathrm{h}\mathsf{L}_\mathrm{e}\eta$ of the Lorentz force. We emphasize that the terms $B_\mathrm{h}\mathsf{L}_\mathrm{e}$ and $\frac{1}{2}\dot{B}_\mathrm{h}\mathsf{L}_\mathrm{e}$ constitute another relevant difference from the work by Cazzolli et al. (2020) and add to the damping matrix C_e and to the stiffness matrix K_e, respectively.

To solve Eqs. (48a) and (48b), it is convenient to apply the Schur complement technique (Zampieri, 2000; Pastore et al., 2024). Hence, Eqs. (48a) and (48b) are rewritten in matrix form as

$$\begin{bmatrix} \mathsf{M}_\mathrm{e} & -\mathsf{A}_\mathrm{e}^\mathrm{T} \\ -\mathsf{A}_\mathrm{e} & \mathsf{O} \end{bmatrix} \begin{Bmatrix} \ddot{\eta} \\ \rho \end{Bmatrix} = \begin{Bmatrix} -\mathsf{C}_\mathrm{eff}(t)\,\dot{\eta} - \mathsf{K}_\mathrm{eff}(t)\,\eta \\ 0 \end{Bmatrix}, \tag{50}$$

where the shorthand notation

$$\mathsf{C}_\mathrm{eff}(t) := \mathsf{C}_\mathrm{e} + B_\mathrm{h}(t)\mathsf{L}_\mathrm{e}, \tag{51a}$$

$$\mathsf{K}_\mathrm{eff}(t) := \mathsf{K}_\mathrm{e} + F\mathsf{G}_\mathrm{e} + \tfrac{1}{2}\dot{B}_\mathrm{h}(t)\mathsf{L}_\mathrm{e} \tag{51b}$$

has been introduced to highlight that the problem at hand naturally yields the *effective* damping matrix $\mathsf{C}_\mathrm{eff}(t)$ and the *effective* stiffness matrix $\mathsf{K}_\mathrm{eff}(t)$, both depending explicitly on time because of the imposed $B_\mathrm{h}(t)$ (see Remark 4).

At this stage, the system (50) is formally solved for $\ddot{\eta}$ and ρ, thereby obtaining

$$\begin{aligned} \ddot{\eta}(t) &= -\left[\mathsf{M}_\mathrm{e}^{-1} - \mathsf{M}_\mathrm{e}^{-1}\mathsf{A}_\mathrm{e}^\mathrm{T}\mathsf{S}_\mathrm{e}^{-1}\mathsf{A}_\mathrm{e}\mathsf{M}_\mathrm{e}^{-1}\right]\left\{\mathsf{C}_\mathrm{eff}(t)\,\dot{\eta}(t) + \mathsf{K}_\mathrm{eff}(t)\,\eta(t)\right\} \\ &\equiv \mathsf{R}_\mathsf{C}(t)\,\dot{\eta}(t) + \mathsf{R}_\mathsf{K}(t)\,\eta(t), \end{aligned} \tag{52a}$$

$$\rho(t) = \left[\mathsf{S}_\mathrm{e}^{-1}\mathsf{A}_\mathrm{e}\mathsf{M}_\mathrm{e}^{-1}\right]\left\{\mathsf{C}_\mathrm{eff}(t)\,\dot{\eta}(t) + \mathsf{K}_\mathrm{eff}(t)\,\eta(t)\right\}, \tag{52b}$$

where the 1×1 (invertible) matrix $\mathsf{S}_\mathrm{e} := \mathsf{A}_\mathrm{e}\mathsf{M}_\mathrm{e}^{-1}\mathsf{A}_\mathrm{e}^\mathrm{T}$ is referred to as *Schur matrix*, and the auxiliary 3×3 matrices $\mathsf{R}_\mathsf{K}(t)$ and $\mathsf{R}_\mathsf{C}(t)$ are defined as

$$\mathsf{R}_\mathsf{K}(t) = -\left[\mathsf{M}_\mathrm{e}^{-1} - \mathsf{M}_\mathrm{e}^{-1}\mathsf{A}_\mathrm{e}^\mathrm{T}\mathsf{S}_\mathrm{e}^{-1}\mathsf{A}_\mathrm{e}\mathsf{M}_\mathrm{e}^{-1}\right]\mathsf{K}_\mathrm{eff}(t), \tag{53a}$$

$$\mathsf{R}_\mathsf{C}(t) = -\left[\mathsf{M}_\mathrm{e}^{-1} - \mathsf{M}_\mathrm{e}^{-1}\mathsf{A}_\mathrm{e}^\mathrm{T}\mathsf{S}_\mathrm{e}^{-1}\mathsf{A}_\mathrm{e}\mathsf{M}_\mathrm{e}^{-1}\right]\mathsf{C}_\mathrm{eff}(t). \tag{53b}$$

It is worth noticing that, although in the present case S_e consists of the single nonzero real number $1/M$ (because there is only one constraint), and is therefore trivially invertible, the Schur matrix is invertible even when more (well-posed) constraints are considered; in that case, S_e is an invertible matrix with number of rows and columns equal to the number of the constraints.

Taking advantage from the property of the Schur complement technique, which allows for decoupling the determination of the Lagrange multiplier $\rho(t)$ from the calculation of the elements of the array $\eta(t)$, we start solving Eq. (52a). To do this, and in view of the linear stability analysis that has to be conducted for the problem under consideration, Eq. (52a) is rewritten in the state-variable formalism by introducing the state variable $\mathsf{Y} = \{\eta_1\, \eta_2\, \eta_3\, \dot{\eta}_1\, \dot{\eta}_2\, \dot{\eta}_3\}^\mathrm{T}$, so as to obtain

$$\dot{\mathsf{Y}}(t) = \mathsf{J}(t)\mathsf{Y}(t), \qquad \mathsf{J}(t) := \begin{bmatrix} \mathsf{O}_{3\times3} & \mathsf{I}_{3\times3} \\ \mathsf{R}_\mathsf{K}(t) & \mathsf{R}_\mathsf{C}(t) \end{bmatrix}, \tag{54}$$

with $\mathsf{J}(t)$ being a 6×6 matrix depending on time through $B_\mathrm{h}(t)$ and $\dot{B}_\mathrm{h}(t)$, and $\mathsf{I}_{n\times n}$ denoting the identity matrix of dimension n. Note that $\mathsf{J}(t)$ can be identified with the Jacobian matrix obtained by linearizing Eqs. (34a)–(34c) and (36), after applying the Schur complement technique and transforming the resulting equations in the state-variable formalism. The expression for $\mathsf{J}(t)$ is reported in Section A of the Supplementary Material.

Eq. (54) is completed with the initial condition $\mathsf{Y}(t=0) = \mathsf{Y}_\mathrm{e} = \{0\,0\,-2\,0\,0\,0\}^\mathrm{T}$. Moreover, from here on we make the important assumption that $B_\mathrm{h}(t)$ is a periodic function of time and, for simplicity, we consider $B_\mathrm{h}(t) = B_\mathrm{M}\sin(\Omega t)$, with $\Omega > 0$ being an assigned frequency. To justify the approach followed in this work of a magnetic induction field *'slowly varying in time'* (Rousseaux et al., 2008), Ω must be chosen small enough (see Section 5.1 below for the contextualization of this assumption in possible biomedical applications).

To properly analyze Eq. (54), Floquet theory is used. However, before proceeding with this analysis, we present an important property of $\mathsf{J}(t)$, connected with the way in which the Lorentz force couples with the elastic structure under consideration in the linearized case. This property is formalized by stating a theorem based on the similarity relation between two matrices. Indeed, it is known that matrices which are similar have the same characteristic polynomial and, thus, the same eigenvalues. Hence, to compute the eigenvalues of a given matrix, such as $\mathsf{J}(t)$, one first determines a similar matrix for which the characteristic polynomial is easier to calculate, and then computes the eigenvalues of this similar matrix.

Theorem 1 (*Lorentz force does not affect the eigenvalues of the Jacobian matrix $J(t)$*).

The characteristic polynomial of the Jacobian matrix $J(t)$ in Eq. (54) is independent of time, and its roots, which are the eigenvalues of $J(t)$, are the same as those characterizing the structure in the absence of $B_h(t)$ and $\dot{B}_h(t)$, which are representative of the Lorentz force, independently of their functional forms.

***Proof*.** Given the Jacobian matrix $\mathsf{J}(t)$ in Eq. (54), one can define a constant-in-time, invertible 6×6 matrix Σ that transforms $\mathsf{J}(t)$ into the similar Jacobian matrix $\tilde{\mathsf{J}}(t) = \Sigma\mathsf{J}(t)\Sigma^{-1}$ characterized by a lower-triangular block-wise structure,

$$\tilde{\mathsf{J}}(t) = \begin{bmatrix} \mathsf{N} & \mathsf{O}_{2\times4} \\ \mathsf{B}(t) & \mathsf{Z} \end{bmatrix}, \tag{55}$$

where the non-zero blocks read as

$$\mathsf{N} = \begin{bmatrix} 0 & 1 \\ 0 & 0 \end{bmatrix}, \qquad \mathsf{Z} = \begin{bmatrix} 0 & 0 & 1 & 0 \\ 0 & 0 & 0 & 1 \\ \frac{2}{5}(2F-7) & \frac{2}{15}(4F-9) & -\frac{14}{5}c & -\frac{6}{5}c \\ \frac{6}{5}(14F-69) & \frac{2}{5}(28F-103) & -\frac{414}{5}c & -\frac{206}{5}c \end{bmatrix}, \tag{56a}$$

$$\mathsf{B}(t) = \begin{bmatrix} 0 & 0 \\ 0 & 0 \\ 0 & 0 \\ 20\dot{B}_\mathrm{h}(t) & 40B_\mathrm{h}(t) \end{bmatrix}. \tag{56b}$$

The 2×2 matrix N and the 4×4 matrix Z in Eq. (56a) are constant in time and equal to the matrices that characterize the Jacobian matrix of the mechanical device in the absence of the Lorentz force, as studied by Cazzolli et al. (2020) (see also Section B of the Supplementary Material). However, the 4×2 matrix $\mathsf{B}(t)$ depends explicitly on time, and, in the transformed Jacobian matrix $\tilde{\mathsf{J}}(t)$, it is the only block collecting the contributions due to the Lorentz force. We call $\mathsf{B}(t)$ *Lorentz block* in the following. The expressions of Σ and Σ^{-1} are reported in Section A of the Supplementary Material.

Since $\tilde{\mathsf{J}}(t)$ is similar to $\mathsf{J}(t)$, both matrices have the same characteristic polynomial and, thus, the same eigenvalues. Because of the simpler structure of $\tilde{\mathsf{J}}(t)$, it is convenient to compute its characteristic polynomial, $P(\lambda) := \det\left[\tilde{\mathsf{J}}(t) - \lambda\mathsf{I}_{6\times6}\right]$. This quantity, in fact, by virtue of standard theorems holding for lower-triangular block-wise matrices, is the product of the determinants of the diagonal blocks $\mathsf{N} - \lambda\mathsf{I}_{2\times2}$ and

$\mathsf{Z}-\lambda\mathsf{I}_{4\times4}$,

$$P(\lambda) := \det\left[\tilde{\mathsf{J}}(t)-\lambda\mathsf{I}_{6\times6}\right] = \det\left[\mathsf{N}-\lambda\mathsf{I}_{2\times2}\right]\det\left[\mathsf{Z}-\lambda\mathsf{I}_{4\times4}\right]. \tag{57}$$

Since the contributions of the Lorentz force are confined to the lower-diagonal block $\mathsf{B}(t)$ of Eq. (55), they do not feature in the characteristic polynomial of $\tilde{\mathsf{J}}(t)$ and $\mathsf{J}(t)$, given in Eq. (57). Consequently, they have no effect on the eigenvalues of $\tilde{\mathsf{J}}(t)$ and $\mathsf{J}(t)$, which are therefore equal to those obtained in the absence of the Lorentz force. This proves the theorem, which holds true independently of the functional form of $B_{\rm h}(t)$ and, thus, of $\dot{B}_{\rm h}(t)$. □

A heuristic evidence for the results summarized in Theorem 1 is provided in Fig. S1 of Section B of the Supplementary Material.

We complete Theorem 1 with the following two remarks.

Remark 5 (*The 'true' degree of the characteristic polynomial of $J(t)$*)**.**

The characteristic polynomial in Eq. (57) coincides with that obtained by Cazzolli et al. (2020) for the Ziegler double pendulum attached to a translating cart. Their model corresponds to the case in which no electric charge is concentrated in the skate and, consequently, the Lorentz force is absent; see Section B of the Supplementary Material. More importantly, with reference to Eq. (56a), the block N describes the linearized nonholonomic 'skate' constraint, while the block Z describes the linearized version of the classical Ziegler double pendulum. Since N and Z are a 2×2 matrix and a 4×4 matrix, respectively, the characteristic polynomial $P(\lambda)$ is of degree six in λ. In particular, the structures of N and Z are such that, as shown in Eq. (57), they contribute to $P(\lambda)$ through the determinants

$$\det[\mathsf{N}-\lambda\mathsf{I}_{2\times2}] = \lambda^2, \tag{58a}$$

$$\det[\mathsf{Z}-\lambda\mathsf{I}_{4\times4}] = 16+32c\,\lambda+4(11+4c^2-3F)\lambda^2+44c\,\lambda^3+\lambda^4 =: Q(\lambda). \tag{58b}$$

Hence, N contributes to $P(\lambda)$ with a factor λ^2, which implies that $\lambda=0$ is an eigenvalue of algebraic multiplicity two. As explained by Neimark and Fufaev, 1972, p.265–267, the inclusion or the exclusion of this zero root does not affect the overall stability properties of the system. Thus, to proceed with the stability analysis, the roots of the fourth-degree polynomial $Q(\lambda)$ can be analyzed. Note that the coefficients of $Q(\lambda)$ encode all the information on stiffness, damping, and the dead load F required to investigate the stability of the Ziegler double pendulum. It is emphasized that the procedure by which the analysis is reduced to $Q(\lambda)$ is indeed a *reduction procedure*, grounded in clear mathematical properties of the system under study: the Lorentz block $\mathsf{B}(t)$ does not affect the determination of the system's eigenvalues, and the zero root of $P(\lambda)$, with algebraic multiplicity two, can be disregarded. It is precisely these properties that allow the stability information on the system to be condensed into the polynomial $Q(\lambda)$. Since the roots of $Q(\lambda)$ determine the occurrence of bifurcations and unstable behaviors in response to variations of F, $Q(\lambda)$ is expressed as a parametric function of F and is denoted as $Q(\lambda;F)$ from here on. The roots of $Q(\lambda;F)$ are denoted by $\lambda_1,\lambda_2,\lambda_3,\lambda_4$. By including also the roots $\lambda_5=\lambda_6=0$ (which replace the null root with algebraic multiplicity 2), the six roots of $P(\lambda)$ are obtained.

Remark 6 (*Necessity for the Floquet theory*)**.**

The 'heart' of Theorem 1 is the similarity transformation that relates $\mathsf{J}(t)$ to $\tilde{\mathsf{J}}(t)=\Sigma\mathsf{J}(t)\Sigma^{-1}$, from which if follows that $\tilde{\mathsf{J}}(t)$ has the same eigenvalues as $\mathsf{J}(t)$, a consequence of the fact that $\mathsf{J}(t)$ and $\tilde{\mathsf{J}}(t)$ belong to the same class of equivalence generated by similarity. In turn, $\tilde{\mathsf{J}}(t)$ has the same eigenvalues as $\mathrm{diag}\{\mathsf{N},\mathsf{Z}\}$, the diagonal and block-wise matrix that describes the structure under study when both $B_{\rm h}(t)$ and $\dot{B}_{\rm h}(t)$ are identically zero (thereby recovering the case analyzed by Cazzolli et al. (2020)). However, since there exists no similarity transformation that relates $\tilde{\mathsf{J}}(t)$ to $\mathrm{diag}\{\mathsf{N},\mathsf{Z}\}$, these two matrices do not belong to the same class of equivalence and, accordingly, the systems that they describe are not equivalent to each other. This result is reflected by the type of solutions that pertain to these two nonequivalent systems: for the system described by the state equation $\dot{\tilde{\mathsf{Y}}}(t)=\mathrm{diag}\{\mathsf{N},\mathsf{Z}\}\tilde{\mathsf{Y}}(t)$, the tentative solution has the form $\tilde{\mathsf{Y}}(t)=\tilde{\mathsf{Y}}_0\mathrm{e}^{\lambda t}$; for the system described by the state equation $\dot{\tilde{\mathsf{Y}}}(t)=\tilde{\mathsf{J}}(t)\tilde{\mathsf{Y}}(t)$, the previous tentative solution is impossible and, if $\tilde{\mathsf{J}}(t)$ is periodic in time, as is the case in our work, the Floquet theory becomes necessary, which will be discussed below. It is recalled that the periodicity of $\tilde{\mathsf{J}}(t)$ follows from the choice $B_{\rm h}(t)=B_{\rm M}\sin(\Omega t)$.

4.2. Floquet theory: $B_h(t)$ and $\dot{B}_h(t)$ are assumed to be time periodic

The functional form of $B_{\rm h}(t)$, which is sinusoidal in time with period $T=2\pi/\Omega$ and fixed frequency $\Omega>0$, allows us to write

$$B_{\rm h}(t) = \quad B_{\rm M}\sin(\Omega t) \equiv \frac{B_{\rm M}}{2i}\mathrm{e}^{i\Omega t}-\frac{B_{\rm M}}{2i}\mathrm{e}^{-i\Omega t}=\frac{iB_{\rm M}}{2}\mathrm{e}^{-i\Omega t}-\frac{iB_{\rm M}}{2}\mathrm{e}^{i\Omega t}, \tag{59a}$$

$$\dot{B}_{\rm h}(t) = \Omega B_{\rm M}\cos(\Omega t) \equiv \frac{B_{\rm M}\Omega}{2}\mathrm{e}^{i\Omega t}+\frac{B_{\rm M}\Omega}{2}\mathrm{e}^{-i\Omega t}=\frac{B_{\rm M}\Omega}{2}\mathrm{e}^{-i\Omega t}+\frac{B_{\rm M}\Omega}{2}\mathrm{e}^{i\Omega t}. \tag{59b}$$

Under Eqs. (59a) and (59b), $\mathsf{C}_{\rm eff}(t)$ and $\mathsf{K}_{\rm eff}(t)$ are periodic functions of time with period $T=2\pi/\Omega$. Therefore, the Jacobian $\mathsf{J}(t)$ in Eq. $(54)_2$ is periodic with the same period, and can be decomposed into a finite number of harmonics as follows (Bentvelsen and Lazarus, 2018):

$$\mathsf{J}(t)=\mathsf{J}_{-1}\mathrm{e}^{-1(i\Omega t)}+\mathsf{J}_0\mathrm{e}^{0(i\Omega t)}+\mathsf{J}_{+1}\mathrm{e}^{+1(i\Omega t)}=\mathsf{J}_{-1}\mathrm{e}^{-i\Omega t}+\mathsf{J}_0+\mathsf{J}_{+1}\mathrm{e}^{i\Omega t}, \tag{60}$$

where J_{-1}, J_0, and J_{+1} are constant-in-time complex matrices, representing the contributions to $\mathsf{J}(t)$ related to the fundamental harmonics $\mathrm{e}^{-1(i\Omega t)}$, $\mathrm{e}^{0(i\Omega t)}$, and $\mathrm{e}^{+1(i\Omega t)}$, respectively. Note that $\mathsf{J}_{-1}=\bar{\mathsf{J}}_{+1}$ (the overbar denotes the operation of complex conjugation), and that J_0 is a real matrix. For problems more involved than the one analyzed here, it becomes necessary to expand $\mathsf{J}(t)$ in a Fourier series.

Given the structure of Eq. (54) and the periodicity of the Jacobian $\mathsf{J}(t)$ in Eq. (60), the generic entry of the unknown array $\mathsf{Y}(t)$ can be expanded in Floquet form as (Guskov and Thouverez, 2012; Bentvelsen and Lazarus, 2018)

$$Y_\alpha(t)=\mathrm{e}^{\lambda t}p_\alpha(t)=\mathrm{e}^{\lambda t}\textstyle\sum_{\nu=-\infty}^{+\infty}p_{\alpha,\nu}\mathrm{e}^{i\nu\Omega t}=\sum_{\nu=-\infty}^{+\infty}p_{\alpha,\nu}\mathrm{e}^{(\lambda+i\nu\Omega)t},\quad \alpha=1,\dots,6, \tag{61}$$

where λ is an unknown complex number referred to as *Floquet exponent* (Bentvelsen and Lazarus, 2018), and $p_1(t),\dots,p_6(t)$ are periodic functions with period $T=2\pi/\Omega$ and Fourier series $p_\alpha(t)=\sum_{\nu=-\infty}^{+\infty}p_{\alpha,\nu}\mathrm{e}^{i\nu\Omega t}$. For each $\alpha=1,\dots,6$, and for all integers $\nu\in\mathbb{Z}$, the coefficients $p_{\alpha,\nu}$ are complex numbers satisfying the property $p_{\alpha,-\nu}=\bar{p}_{\alpha,\nu}$. For future use, the arrays $\mathsf{p}(t)=\{p_1(t)\cdots p_6(t)\}^{\rm T}$ and $\mathsf{p}_\nu:=\{p_{1,\nu}\cdots p_{6,\nu}\}^{\rm T}$, with $\nu\in\mathbb{Z}$, are introduced, so that Eq. (61) can be rewritten in compact form as $\mathsf{Y}(t)=\mathrm{e}^{\lambda t}\mathsf{p}(t)$, with $\mathsf{p}(t)=\sum_{\nu=-\infty}^{+\infty}\mathsf{p}_\nu\mathrm{e}^{i\nu\Omega t}$.

It is worth recalling that $\mathsf{Y}(t)=\mathrm{e}^{\lambda t}\mathsf{p}(t)$ is referred to as the *fundamental solution* (Bentvelsen and Lazarus, 2018). It represents the periodic-case generalization of the solution $\mathsf{Y}(t)=\mathrm{e}^{\lambda t}\mathsf{p}_0$, with constant p_0, which arises when the Jacobian is independent of time.

In general, λ can be written as $\lambda=\mathrm{Re}[\lambda]+i\,\mathrm{Im}[\lambda]$, and, for a given $\mathrm{Im}[\lambda]$, there exists a real number r such that $\mathrm{Im}[\lambda]$ can be expressed as $\mathrm{Im}[\lambda]=r\Omega$. Such a number r, in turn, can be decomposed as $r=\lfloor r\rfloor+\mathfrak{m}(r)$, where $\lfloor\cdot\rfloor:\mathbb{R}\to\mathbb{Z}$ denotes the *floor function* and $\mathfrak{m}:\mathbb{R}\to[0,1[$ is the *sawtooth wave*. A substitution of this representation of λ back into Eq. (61), rewritten in terms of the arrays $\mathsf{Y}(t)$ and $\mathsf{p}(t)$, leads to

$$\mathsf{Y}(t)=\mathrm{e}^{\lambda t}\mathsf{p}(t)=\mathrm{e}^{\lambda t}\textstyle\sum_{\nu=-\infty}^{+\infty}\mathsf{p}_\nu\mathrm{e}^{i\nu\Omega t}=\mathrm{e}^{\mathrm{Re}[\lambda]t}\mathrm{e}^{i\lfloor r\rfloor\Omega t}\mathrm{e}^{i\mathfrak{m}(r)\Omega t}\sum_{\nu=-\infty}^{+\infty}\mathsf{p}_\nu\mathrm{e}^{i\nu\Omega t}. \tag{62}$$

Since $\lfloor r\rfloor$ is an integer number, the phase factor $\mathrm{e}^{i\lfloor r\rfloor\Omega t}$ is periodic with period $T=2\pi/\Omega$. Indeed, $\mathrm{e}^{i\lfloor r\rfloor\Omega(t+T)}=\mathrm{e}^{i\lfloor r\rfloor\Omega t}$, because $\mathrm{e}^{i\lfloor r\rfloor\Omega\frac{2\pi}{\Omega}}=\mathrm{e}^{i2\pi\lfloor r\rfloor}=1$. Thus, the possible non-periodicity of $\mathsf{Y}(t)$ is due to $\mathrm{Re}[\lambda]$ and $\mathfrak{m}(r)$, whenever at least one of them is nonzero. However, the origin of the non-periodicity of $\mathsf{Y}(t)$ connected to $\mathrm{Re}[\lambda]$ is different from that connected to $\mathfrak{m}(r)$. Indeed, the non-periodicity due to $\mathrm{Re}[\lambda]\neq0$ is related to the presence of the damping c in the viscoelastic hinges, and to the dead load F (in fact, even for $c = 0$ there is a nonzero $\mathrm{Re}[\lambda]$ for values of F above the critical load for flutter). The non-periodicity associated with $\mathfrak{m}(r) \neq 0$ is an intrinsic property of the system and of the considered interactions, reflected in the nature of the computed Floquet exponent.

It is also important to note that, since the dimension of the array $\mathsf{Y}(t)$ is equal to 6, it is possible to determine six *fundamental Floquet exponents* $\lambda_{f1}, \dots, \lambda_{f6}$, each of which is representable as $\lambda_{f\alpha} = \mathrm{Re}[\lambda_{f\alpha}] + i\,\mathrm{Im}[\lambda_{f\alpha}] = \mathrm{Re}[\lambda_{f\alpha}] + i\mathfrak{m}(r_{f\alpha})\Omega$, for $\alpha = 1, \dots, 6$, and, thus, with $\lfloor r_{f\alpha} \rceil = 0$, for all $\alpha = 1, \dots, 6$.

As shown below, substituting Eq. (62) into Eq. (54) leads to an eigenvalue problem whose eigenvalues are the Floquet exponents. Among these eigenvalues, the nonzero fundamental Floquet exponents are those that break the discrete time-translation symmetry associated with the periodic functions $B_h(t)$ and $\dot{B}_h(t)$ featuring in the Lorentz force.

Substituting the Fourier expansion of $\mathsf{p}(t)$ given in Eq. (62) into $\mathsf{Y}(t) = e^{\lambda t}\mathsf{p}(t)$ yields

$$\mathsf{Y}(t) = \sum_{\nu=-\infty}^{+\infty} \mathsf{p}_\nu e^{(\lambda + i\nu\Omega)t}. \tag{63}$$

Thus, upon the assumption of uniform convergence of the Fourier series of $\mathsf{p}(t)$, differentiation with respect to time leads to

$$\dot{\mathsf{Y}}(t) = \sum_{\nu=-\infty}^{+\infty} (\lambda + i\nu\Omega)\mathsf{p}_\nu e^{(\lambda + i\nu\Omega)t}. \tag{64}$$

Next, a substitution of $\mathsf{Y}(t)$ and $\dot{\mathsf{Y}}(t)$ into Eq. $(54)_1$ produces an algebraic system for the infinitely many unknown Fourier coefficients p_ν of $\mathsf{p}(t)$. To emphasize the properties of this system, we start considering the more general case in which $\mathsf{J}(t)$ is a periodic function of time that, instead of the simple expression given in Eq. (60), has Fourier series $\mathsf{J}(t) = \sum_{\nu=-\infty}^{+\infty} \mathsf{J}_\nu e^{i\nu\Omega t}$. Then, the product $\mathsf{J}(t)\mathsf{Y}(t)$ on the right-hand side of Eq. $(54)_1$ becomes the Fourier series of the discrete convolution product, multiplied by $e^{\lambda t}$, between the sequences $\{\mathsf{J}_\nu\}_{\nu\in\mathbb{Z}}$ and $\{\mathsf{p}_\nu\}_{\nu\in\mathbb{Z}}$ of the Fourier expansions of $\mathsf{J}(t)$ and $\mathsf{p}(t)$, respectively. In fact, it is possible to show that $\mathsf{J}(t)\mathsf{p}(t)$ becomes $\mathsf{J}(t)\mathsf{p}(t) = \sum_{\nu=-\infty}^{+\infty}[\sum_{\kappa=-\infty}^{+\infty} \mathsf{J}_{\nu-\kappa}\mathsf{p}_\kappa] e^{(\lambda+i\nu\Omega)t}$. Consequently, Eq. $(54)_1$ becomes

$$\begin{aligned} &\sum_{\nu=-\infty}^{+\infty}\Big\{\sum_{\kappa=-\infty}^{+\infty} \mathsf{J}_{\nu-\kappa}\mathsf{p}_\kappa - (\lambda + i\nu\Omega)\mathsf{p}_\nu\Big\} e^{(\lambda+i\nu\Omega)t} \\ &= e^{\lambda t}\sum_{\nu=-\infty}^{+\infty}\Big\{\sum_{\kappa=-\infty}^{+\infty}[\mathsf{J}_{\nu-\kappa} - \delta_{\nu\kappa} i\kappa\Omega\,\mathsf{I}_{6\times6}]\mathsf{p}_\kappa - \lambda\mathsf{p}_\nu\Big\} e^{i\nu\Omega t} = 0, \end{aligned} \tag{65}$$

where $\delta_{\nu\kappa}$ is the Kronecker Delta. Furthermore, by exploiting the orthonormality of the Fourier basis functions $\{\sqrt{\Omega/2\pi}\, e^{i\nu\Omega t}\}_{\nu\in\mathbb{Z}}$, the algebraic system for the infinitely many unknown Fourier coefficients $\{\mathsf{p}_\nu\}_{\nu\in\mathbb{Z}}$ is obtained

$$\sum_{\kappa=-\infty}^{+\infty}[\mathsf{J}_{\nu-\kappa} - \delta_{\nu\kappa} i\kappa\Omega\,\mathsf{I}_{6\times6}]\mathsf{p}_\kappa - \lambda\mathsf{p}_\nu = 0, \qquad \nu \in \mathbb{Z}. \tag{66}$$

The infinite matrix $[\mathsf{J}_{\nu-\kappa} - \delta_{\nu\kappa} i\kappa\Omega\,\mathsf{I}_{6\times6}]_{\nu,\kappa\in\mathbb{Z}}$ is referred to as the *Hill matrix* (Bentvelsen and Lazarus, 2018; Guillot et al., 2020). This is a block matrix in which the generic $\nu\kappa$ block is given by the 6×6 matrix $[\mathsf{J}_{\nu-\kappa} - \delta_{\nu\kappa} i\kappa\,\Omega\,\mathsf{I}_{6\times6}]$.

Finally, the change of variable $\nu - \kappa = \gamma$ leads to

$$\sum_{\gamma=-\infty}^{+\infty}[\mathsf{J}_\gamma - \delta_{\nu(\nu-\gamma)} i(\nu-\gamma)\Omega\,\mathsf{I}_{6\times6}]\mathsf{p}_{\nu-\gamma} - \lambda\mathsf{p}_\nu = 0, \qquad \nu \in \mathbb{Z}. \tag{67}$$

Eqs. (66) and (67) are equivalent forms of the *extended eigenvalue problem* (Bentvelsen and Lazarus, 2018; Guillot et al., 2020). Note that Eq. (67) is the frequency-domain analogue of the Bloch–Floquet problem in wave-vector space. In solid-state physics, this problem provides the formal basis for the Bloch theory of conduction in metals (Ashcroft and Mermin, 1976).

The case of interest in the present work, in which $\mathsf{J}(t)$ is given in Eq. (60), is recovered by identically setting $\mathsf{J}_\nu = 0$ for $|\nu| \geq 2$. Under this hypothesis, Eq. (67) can be rewritten as

$$\mathsf{J}_{+1}\mathsf{p}_{\nu-1} + (\mathsf{J}_0 - i\nu\Omega\,\mathsf{I}_{6\times6})\mathsf{p}_\nu + \mathsf{J}_{-1}\mathsf{p}_{\nu+1} - \lambda\mathsf{p}_\nu = 0, \qquad \nu \in \mathbb{Z}. \tag{68}$$

Following Bentvelsen and Lazarus (2018), Guillot et al. (2020), the system of equations (68) is truncated to a sufficiently large value H of ν. Since each Fourier coefficient p_ν is a 6-dimensional array, the truncation order must satisfy $H \geq 6$. The truncated version of Eq. (68) is then a finite-dimensional eigenvalue problem and can be recast in block-wise form as

$$\begin{bmatrix} \mathsf{J}_0 + iH\Omega & \mathsf{J}_{-1} & 0_{6\times6} & 0_{6\times6} & \cdots & 0_{6\times6} \\ \mathsf{J}_{+1} & \mathsf{J}_0 + i(H-1)\Omega & \mathsf{J}_{-1} & 0_{6\times6} & \cdots & 0_{6\times6} \\ 0_{6\times6} & \mathsf{J}_{+1} & \mathsf{J}_0 + i(H-2)\Omega & \mathsf{J}_{-1} & \cdots & 0_{6\times6} \\ \vdots & \ddots & \vdots & \vdots & \ddots & \vdots \\ 0_{6\times6} & \cdots & \mathsf{J}_{+1} & \mathsf{J}_0 - i(H-2)\Omega & \mathsf{J}_{-1} & 0_{6\times6} \\ 0_{6\times6} & \cdots & 0_{6\times6} & \mathsf{J}_{+1} & \mathsf{J}_0 - i(H-1)\Omega & \mathsf{J}_{-1} \\ 0_{6\times6} & \cdots & 0_{6\times6} & 0_{6\times6} & \mathsf{J}_{+1} & \mathsf{J}_0 - iH\Omega \end{bmatrix} \begin{Bmatrix} \mathsf{p}_{-H} \\ \mathsf{p}_{-(H-1)} \\ \mathsf{p}_{-(H-2)} \\ \vdots \\ \mathsf{p}_{+(H-2)} \\ \mathsf{p}_{+(H-1)} \\ \mathsf{p}_{+H} \end{Bmatrix} = \lambda \begin{Bmatrix} \mathsf{p}_{-H} \\ \mathsf{p}_{-(H-1)} \\ \mathsf{p}_{-(H-2)} \\ \vdots \\ \mathsf{p}_{+(H-2)} \\ \mathsf{p}_{+(H-1)} \\ \mathsf{p}_{+H} \end{Bmatrix}. \tag{69}$$

The tridiagonal $6(2H+1)\times6(2H+1)$ matrix on the left-hand side is called the *truncated Hill matrix of order H* (Bentvelsen and Lazarus, 2018). The $6(2H+1)\times1$ array $\{\mathsf{p}_{-H} \cdots \mathsf{p}_{+H}\}^{\mathrm{T}}$ is the generic eigenvector associated with the eigenvalue λ in Eq. (69).

The characteristic polynomial of the truncated Hill matrix has $6(2H+1)$ complex roots $\lambda_1, \dots, \lambda_{6(2H+1)}$, for each $H \geq 6$. For a sufficiently large value of H, the imaginary part of only six of these roots belongs to the *fundamental frequency interval* $[-\Omega/2, +\Omega/2[$, see the *eigenvalue sorting* done by Bentvelsen and Lazarus (2018). These roots are denoted by $\lambda_{f1}, \dots, \lambda_{f6}$ and are such that $\mathrm{Im}[\lambda_{f\alpha}] = r_{f\alpha}\Omega$ belongs to the interval $[-\Omega/2, +\Omega/2[$ for $\alpha = 1, \dots, 6$. Therefore, it is concluded that $r_{f\alpha} \in [-1/2, +1/2[$.

The sawtooth map establishes a one-to-one correspondence between $r_{f\alpha} \in [-1/2, +1/2[$ and $\mathfrak{m}(r_{f\alpha}) \in [0, 1[$. Therefore, instead of selecting the six fundamental roots such that $r_{f\alpha} \in [-1/2, +1/2[$, one may equivalently select them so that $r_{f\alpha} \in [0, 1[$, for $\alpha = 1, \dots, 6$. For these roots, it holds automatically that $r_{f\alpha} \equiv \mathfrak{m}(r_{f\alpha})$.[2]

The above discussion justifies the representation of $\mathsf{Y}(t)$ provided in Eq. (62), where the sawtooth wave was used, and explains the loss of periodicity of $\mathsf{Y}(t)$ due to the factor $e^{i\mathfrak{m}(r)\Omega t}$. In the following, results are presented by considering the six fundamental roots $\lambda_{f1}, \dots, \lambda_{f6}$ with imaginary parts $\mathrm{Im}[\lambda_{f\alpha}] \in [-\Omega/2, +\Omega/2[$, for each $\alpha = 1, \dots, 6$, as suggested by Bentvelsen and Lazarus (2018).

In the limit for $H \to +\infty$, the roots $\lambda_{f1}, \dots, \lambda_{f6}$ converge to the six *fundamental Floquet exponents* of the infinite-dimensional problem in Eq. (68). To 'simulate' numerically such infinite dimensionality, a sufficiently large value of H is considered.

After the six fundamental Floquet exponents are computed, the solution $\mathsf{Y}(t)$ to the linear system given in Eq. $(54)_1$ can be obtained as (Bentvelsen and Lazarus, 2018)

$$\mathsf{Y}(t) = \sum_{\alpha=1}^{6} y_\alpha e^{\lambda_{f\alpha} t}\sum_{\nu=-\infty}^{+\infty}\mathsf{p}_{\nu,\alpha}e^{i\nu\Omega t} = \sum_{\alpha=1}^{6} y_\alpha e^{\mathrm{Re}[\lambda_{f\alpha}]t} e^{i\,\mathrm{Im}[\lambda_{f\alpha}]t}\sum_{\nu=-\infty}^{+\infty}\mathsf{p}_{\nu,\alpha}e^{i\nu\Omega t}, \tag{70}$$

where $y_1, \dots, y_6$ are real constants.

The preceding discussion provides the general framework for treating the problem under study when the linearized governing equations, written in state-variable form, have time-dependent coefficients. However, one important feature of our problem is that the presence of the

[2] Having set $\mathrm{Im}[\lambda_f] = r_f\Omega$, the inequality $-\Omega/2 \leq \mathrm{Im}[\lambda_f] < +\Omega/2$ can be rewritten as $-1/2 \leq r_f < +1/2$. We use now the property of the sawtooth wave $\mathfrak{m}(x) = 1 - \mathfrak{m}(-x)$ for all $x \in \mathbb{R} \setminus \mathbb{Z}$ to map $r_f \in [-1/2, +1/2[$ into $[0, 1[$. If $r_f \in [-1/2, 0[$, then $\mathfrak{m}(r_f) = 1 - \mathfrak{m}(-r_f) = 1 + r_f \in [1/2, 1[$; if $r = 0$, then $\mathfrak{m}(0) = 0$; if $r_f \in]0, 1/2[$, then $\mathfrak{m}(r_f) = r_f \in]0, 1/2[$. In conclusion, the interval $r_f \in [-1/2, +1/2[$ is mapped into $\mathfrak{m}(r_f) \in [0, 1[$, and vice versa.

terms J_{-1} and J_{+1}, which represent the time variability of $\mathsf{J}(t)$ induced by the Lorentz force through $B_h(t)$ and $\dot{B}_h(t)$, *does not contribute* to the value of the fundamental Floquet exponents. Therefore, apart from the choice of their representation, the exponents coincide with those obtained from the eigenvalues of the associated problem in the absence of the Lorentz force, as shown in Remark 7 below. This property is limited to the type of problems analyzed here, but it provides a relevant result following from the way in which the Lorentz force couples with the other interactions of the system in the linearized dynamic equations (47a)–(47d) (see also Remark 4, and Section B of the Supplementary Material). This result can be formalized through the following theorem.

Theorem 2 (*Lorentz force does not affect the Floquet exponents*).

Given the extended eigenvalue problem (68), the Floquet exponents are independent of the Fourier coefficients J_{-1} and J_{+1} that account for the time dependence of the Jacobian $J(t)$ in Eq. (54)$_1$. Rather, they depend solely on J_0 and, thus, on the matrices N and Z.

Proof. The transformation matrix Σ is applied to the extended eigenvalue problem (68). Thus, by introducing, for each $\nu \in \mathbb{Z}$, the transformed array $\tilde{\mathsf{p}}_\nu := \Sigma\mathsf{p}_\nu$, Eq. (68) is rewritten as

$$\tilde{\mathsf{J}}_{+1}\tilde{\mathsf{p}}_{\nu-1} + (\tilde{\mathsf{J}}_0 - i\nu\Omega\,\mathsf{I}_{6\times6})\tilde{\mathsf{p}}_\nu + \tilde{\mathsf{J}}_{-1}\tilde{\mathsf{p}}_{\nu+1} - \lambda\tilde{\mathsf{p}}_\nu = 0, \qquad \nu \in \mathbb{Z}, \tag{71}$$

where the transformed Fourier coefficients $\tilde{\mathsf{J}}_{+1} = \Sigma\mathsf{J}_{+1}\Sigma^{-1}$, $\tilde{\mathsf{J}}_0 = \Sigma\mathsf{J}_0\Sigma^{-1}$, and $\tilde{\mathsf{J}}_{-1} = \Sigma\mathsf{J}_{-1}\Sigma^{-1}$ are

$$\tilde{\mathsf{J}}_{-1} = \begin{bmatrix} \mathsf{O}_{2\times2} & \mathsf{O}_{2\times4} \\ \mathsf{B}_{-1} & \mathsf{O}_{4\times4} \end{bmatrix}, \; \tilde{\mathsf{J}}_0 = \begin{bmatrix} \mathsf{N} & \mathsf{O}_{2\times4} \\ \mathsf{O}_{4\times2} & \mathsf{Z} \end{bmatrix}, \; \tilde{\mathsf{J}}_{+1} = \begin{bmatrix} \mathsf{O}_{2\times2} & \mathsf{O}_{2\times4} \\ \mathsf{B}_{+1} & \mathsf{O}_{4\times4} \end{bmatrix}. \tag{72}$$

Here, B_{-1} and $\mathsf{B}_{+1} \equiv \overline{\mathsf{B}_{-1}}$ are two 4×2 matrices representing the -1 and $+1$ Fourier coefficients of the matrix $\mathsf{B}(t)$ introduced in Eq. (56b).

By letting ν vary over $\mathbb{Z}$ from $\nu = -H$ to $\nu = +H$, dropping the terms involving $\tilde{\mathsf{p}}_{-H-1}$ and $\tilde{\mathsf{p}}_{+H+1}$, and introducing the notation $\sigma_\nu := \lambda + i\nu\Omega$, Eq. (71) can be rewritten as

$$(\tilde{\mathsf{J}}_0 - \sigma_{-H}\,\mathsf{I}_{6\times6})\tilde{\mathsf{p}}_{-H} + \tilde{\mathsf{J}}_{-1}\tilde{\mathsf{p}}_{-H+1} = 0, \qquad \nu = -H, \tag{73a}$$

$$\tilde{\mathsf{J}}_{+1}\tilde{\mathsf{p}}_{\nu-1} + (\tilde{\mathsf{J}}_0 - \sigma_\nu\,\mathsf{I}_{6\times6})\tilde{\mathsf{p}}_\nu + \tilde{\mathsf{J}}_{-1}\tilde{\mathsf{p}}_{\nu+1} = 0, \qquad \nu \in]-H, +H[\, \cap \mathbb{Z}, \tag{73b}$$

$$\tilde{\mathsf{J}}_{+1}\tilde{\mathsf{p}}_{+H-1} + (\tilde{\mathsf{J}}_0 - \sigma_{+H}\,\mathsf{I}_{6\times6})\tilde{\mathsf{p}}_{+H} = 0, \qquad \nu = +H. \tag{73c}$$

Now the matrices in Eq. (72) are substituted into Eqs. (73a)–(73c), and $\tilde{\mathsf{p}}_\nu$ is written as $\tilde{\mathsf{p}}_\nu = \{\tilde{\mathsf{r}}_\nu \; \tilde{\mathsf{s}}_\nu\}^{\mathrm{T}}$, for $\nu = -H, \ldots, +H$, where each $\tilde{\mathsf{r}}_\nu$ is a 2×1 array and each $\tilde{\mathsf{s}}_\nu$ is a 4×1 array. All the resulting equations are then *reordered* in the block-wise system

$$\left[\begin{array}{c|c} \mathrm{diag}_0[\mathsf{N} - \sigma_\nu\mathsf{I}_{2\times2}]_\nu & \mathsf{O}_{2(2H+1)\times4(2H+1)} \\ \hline \mathrm{diag}_{-1}[\mathsf{B}_{+1}] + \mathrm{diag}_{+1}[\mathsf{B}_{-1}] & \mathrm{diag}_0[\mathsf{Z} - \sigma_\nu\mathsf{I}_{4\times4}]_\nu \end{array}\right] \left\{\begin{array}{c} \{\tilde{\mathsf{r}}_\nu\}_\nu \\ \hline \{\tilde{\mathsf{s}}_\nu\}_\nu \end{array}\right\} = \left\{\begin{array}{c} \{0_{2\times1}\}_\nu \\ \hline \{0_{4\times1}\}_\nu \end{array}\right\}, \tag{74}$$

which consists of $6(2H+1)$ equations. The matrix $\mathrm{diag}_0[\mathsf{N} - \sigma_\nu\mathsf{I}_{2\times2}]_\nu$ is a block matrix of dimension $2(2H+1)\times2(2H+1)$ with square blocks, among which the only non-null elements are the blocks $[\mathsf{N} - \sigma_\nu\mathsf{I}_{2\times2}]$ allocated along the principal diagonal from $\nu = -H$ to $\nu = +H$. The matrix $\mathrm{diag}_0[\mathsf{Z} - \sigma_\nu\mathsf{I}_{4\times4}]_\nu$ has exactly the same structure as the previous one, the only difference being that the generic ν-th block of the principal diagonal is a 4×4 matrix. Finally, $\mathrm{diag}_{-1}[\mathsf{B}_{+1}]$ is a rectangular block matrix of dimension $4(2H+1)\times2(2H+1)$, in which each block is a 4×2 matrix, and the only non-null blocks are given by the 4×2 matrix B_{+1}, 'repeated' along the first lower-diagonal (note that, viewed in terms of blocks, $\mathrm{diag}_{-1}[\mathsf{B}_{+1}]$ is a $(2H+1)\times(2H+1)$ square matrix). The matrix $\mathrm{diag}_{+1}[\mathsf{B}_{-1}]$ shares the same properties, but the non-null blocks are obtained by 'repeating' B_{-1} along the first upper-diagonal.

Let us now denote by D_H the $6(2H+1)\times6(2H+1)$ matrix on the left-hand side of Eq. (74). For an arbitrary value of $H \geq 6$, the Floquet exponents are obtained as the eigenvalues of the eigenvalue problem (74), and are computed as the roots of the characteristic polynomial $\mathcal{P}_H(\lambda)$ of degree $6(2H+1)$ provided by the determinant of D_H. By applying again the theorems on lower-triangular block matrices used in Theorem 1 to obtain Eq. (57), one finds

$$\begin{aligned} \mathcal{P}_H(\lambda) &\equiv \det\mathsf{D}_H \\ &= \det\{\mathrm{diag}_0[(\mathsf{N} - i\nu\Omega\mathsf{I}_{2\times2}) - \lambda\mathsf{I}_{2\times2}]_\nu\} \\ &\quad \cdot \det\{\mathrm{diag}_0[(\mathsf{Z} - i\nu\Omega\mathsf{I}_{4\times4}) - \lambda\mathsf{I}_{4\times4}]_\nu\}. \end{aligned} \tag{75}$$

The consequence of Eq. (75) is that the Fourier components of the Lorentz force contributions, accounting for its explicit variation in time and entering D_H through the matrices B_{+1} and B_{-1}, are irrelevant for the determination of $\mathcal{P}_H(\lambda)$ and, thus, for the calculation of its roots, which coincide with the Floquet exponents of the theory. □

Theorem 2 displays an interesting additional property: since the matrices N and Z are exactly the same as those in the problem by Cazzolli et al. (2020), the six fundamental Floquet exponents are computable analytically for any $\nu \in \mathbb{Z}$, and are 'equivalent' to the six eigenvalues found in Cazzolli et al. (2020) (see also Sections B and C of the Supplementary Material). This statement is further expanded in the following corollary and remark.

Corollary 1 (*Floquet exponents and eigenvalues in the absence of the Lorentz force*).

Let $\lambda_1, \ldots, \lambda_6$ be the eigenvalues of the Jacobian matrix $\tilde{J}(t)$, or $J(t)$, i.e., the six roots of the polynomial $P(\lambda)$, as computed in Eq. (57) of Theorem 1 (these eigenvalues are independent of the Lorentz force contributions). For arbitrary values of $H \in \mathbb{N}$, the characteristic polynomial $\mathcal{P}_H(\lambda)$ given in Eq. (75) can be factorized into a product of $2H+1$ polynomials, each of degree 6 and characterized by the same coefficients as $P(\lambda)$, provided that, for each $\nu = -H, \ldots, +H$, the change of variables $\lambda \mapsto \sigma_\nu = \lambda + i\nu\Omega$ is made. Moreover, when $H = 0$, $\mathcal{P}_0(\lambda) = P(\lambda)$, and the Floquet exponents coincide with the six roots of $\mathcal{P}_0(\lambda)$, which are trivially equal to $\lambda_1, \ldots, \lambda_6$; for $H > 0$, the roots of $\mathcal{P}_H(\lambda)$ can be computed by first determining the roots $\sigma_{1,\nu}, \ldots, \sigma_{6,\nu}$ of the generic ν-th factor of $\mathcal{P}_H(\lambda)$, which are identical to $\lambda_1, \ldots, \lambda_6$ for each $\nu = -H, \ldots, +H$, and finally through $\lambda_{\alpha,\nu} = \sigma_{\alpha,\nu} - i\nu\Omega$, for all $\alpha = 1, \ldots, 6$.

Proof. Using Eqs. (58a) and (58b) into Eq. (75), $\mathcal{P}_H(\lambda)$ can be rewritten as

$$\begin{aligned} \mathcal{P}_H(\lambda) &= \prod_{\nu=-H}^{+H} \det[\mathsf{N} - (\lambda + i\nu\Omega)\mathsf{I}_{2\times2}]\,\det[\mathsf{Z} - (\lambda + i\nu\Omega)\mathsf{I}_{4\times4}] \\ &= \prod_{\nu=-H}^{+H} (\lambda + i\nu\Omega)^2\, Q(\lambda + i\nu\Omega) = \prod_{\nu=-H}^{+H} P(\lambda + i\nu\Omega). \end{aligned} \tag{76}$$

By setting $\sigma_\nu := \lambda + i\nu\Omega$, for each $\nu = -H, \ldots, +H$, one can obtain $\mathcal{P}_H(\lambda) = \prod_{\nu=-H}^{+H} P(\sigma_\nu)$, meaning that $\mathcal{P}_H(\lambda)$ is factorized in the product of $2H+1$ polynomials. For each $\nu = -H, \ldots, +H$, the polynomial $P(\sigma_\nu)$ has degree six and the same coefficients as $P(\lambda)$ in Eq. (57), evaluated at σ_ν.

If $H = 0$, the only factor of $\mathcal{P}_0(\lambda)$ is $P(\lambda)$, and thus $\mathcal{P}_0(\lambda) \equiv P(\lambda)$, whence $\sigma_{\alpha,0} = \lambda_\alpha$, for all $\alpha = 1, \ldots, 6$.

If $H > 0$, for each $\nu = -H, \ldots, +H$, the roots of $P(\sigma_\nu)$ are $\sigma_{\alpha,\nu} \equiv \lambda_\alpha$, for all $\alpha = 1, \ldots, 6$, and the roots of $\mathcal{P}_H(\lambda)$ are $\lambda_{\alpha,\nu} = \sigma_{\alpha,\nu} - i\nu\Omega = \lambda_\alpha - i\nu\Omega$. Therefore, in the limit $H \to +\infty$, one obtains the infinite sequence of Floquet exponents $\{\lambda_{\alpha,\nu}\}_{\nu\in\mathbb{Z}}$, with $\lambda_{\alpha,\nu} = \lambda_\alpha - i\nu\Omega$. Thus, each $\lambda_{\alpha,\nu}$ differs from λ_α by the purely imaginary offset $-i\nu\Omega$ determined by the frequency Ω of $B_h(t)$ and $\dot{B}_h(t)$ featuring in the Lorentz force, while λ_α itself is independent of the Lorentz force. □

Remark 7 (*Construction of the fundamental Floquet exponents*).

Given the frequency $\Omega > 0$, and for varying values of the dead load $F > 0$, each Floquet exponent $\lambda_{\alpha,\nu} = \lambda_\alpha - i\nu\Omega$, with $\alpha = 1, \ldots, 6$ and $\nu \in \mathbb{Z}$, is to be regarded as a function of F. Hence, we write $\lambda_{\alpha,\nu}(F) = \lambda_\alpha(F) - i\nu\Omega$. Let us then consider the rescaled imaginary part

$\mathrm{Im}[\lambda_{\alpha,\nu}(F)/\Omega] = \mathrm{Im}[\lambda_\alpha(F)/\Omega] - \nu$. Because of the properties of the floor function and of the sawtooth wave, the following relations hold:

$$\lfloor \mathrm{Im}[\lambda_{\alpha,\nu}(F)/\Omega] \rfloor = \lfloor \mathrm{Im}[\lambda_\alpha(F)/\Omega] - \nu \rfloor = \lfloor \mathrm{Im}[\lambda_\alpha(F)/\Omega] \rfloor - \nu, \qquad \alpha = 1,\dots,6, \tag{77a}$$

$$\mathfrak{m}\big(\mathrm{Im}[\lambda_{\alpha,\nu}(F)/\Omega]\big) = \mathfrak{m}\big(\mathrm{Im}[\lambda_\alpha(F)/\Omega] - \nu\big) = \mathfrak{m}\big(\mathrm{Im}[\lambda_\alpha(F)/\Omega]\big), \qquad \alpha = 1,\dots,6. \tag{77b}$$

Therefore, the offset $-\nu$ in $\mathrm{Im}[\lambda_{\alpha,\nu}(F)/\Omega]$ is unessential for the calculation of $\mathfrak{m}\big(\mathrm{Im}[\lambda_{\alpha,\nu}(F)/\Omega]\big)$, which, indeed, coincides with $\mathfrak{m}\big(\mathrm{Im}[\lambda_\alpha(F)/\Omega]\big)$. Hence, we can write

$$\begin{aligned}\mathrm{Im}[\lambda_{\alpha,\nu}(F)] &= \mathrm{Im}[\lambda_{\alpha,\nu}(F)/\Omega]\Omega = \big\{ \lfloor \mathrm{Im}[\lambda_{\alpha,\nu}(F)/\Omega] \rfloor + \mathfrak{m}\big(\mathrm{Im}[\lambda_{\alpha,\nu}(F)/\Omega]\big) \big\}\Omega \\ &= \big\{ \lfloor \mathrm{Im}[\lambda_\alpha(F)/\Omega] \rfloor - \nu + \mathfrak{m}\big(\mathrm{Im}[\lambda_\alpha(F)/\Omega]\big) \big\}\Omega \\ &= \lfloor \mathrm{Im}[\lambda_\alpha(F)/\Omega] \rfloor \Omega - \nu\Omega + \mathfrak{m}\big(\mathrm{Im}[\lambda_\alpha(F)/\Omega]\big)\Omega. \end{aligned} \tag{78}$$

As discussed after Eq. (62), the integer numbers $\lfloor \mathrm{Im}[\lambda_\alpha(F)/\Omega] \rfloor - \nu$ cannot contribute to the fundamental Floquet exponents and can, thus, be disregarded. By definition, $\mathfrak{m}\big(\mathrm{Im}[\lambda_\alpha(F)/\Omega]\big)$ belongs to the interval $[0,1[$ (accordingly, $\mathfrak{m}\big(\mathrm{Im}[\lambda_\alpha(F)/\Omega]\big)\Omega \in [0,\Omega[$). However, since the characterization of the fundamental Floquet exponents is done with respect to the rescaled interval $[-1/2,+1/2[$ (thus, with respect to $[-\Omega/2,+\Omega/2[$, when $\mathfrak{m}\big(\mathrm{Im}[\lambda_\alpha(F)/\Omega]\big)\Omega$ is used), the construction of the fundamental Floquet exponents for each value of F proceeds as follows (see footnote 2):

$$\text{If } \mathfrak{m}\big(\mathrm{Im}[\lambda_\alpha(F)/\Omega]\big) \in \left[0,\tfrac{1}{2}\right[, \quad \text{then } \mathrm{Im}[\lambda_{\mathrm{f}\alpha}(F)/\Omega] := \mathfrak{m}\big(\mathrm{Im}[\lambda_\alpha(F)/\Omega]\big) \in \left[0,\tfrac{1}{2}\right[, \tag{79a}$$

$$\text{if } \mathfrak{m}\big(\mathrm{Im}[\lambda_\alpha(F)/\Omega]\big) \in \left[\tfrac{1}{2},1\right[, \quad \text{then } \mathrm{Im}[\lambda_{\mathrm{f}\alpha}(F)/\Omega] := \mathfrak{m}\big(\mathrm{Im}[\lambda_\alpha(F)/\Omega]\big) - 1 \in \left[-\tfrac{1}{2},0\right[. \tag{79b}$$

Therefore, the fundamental Floquet exponents are the complex numbers $\lambda_{\mathrm{f}1}(F),\dots,\lambda_{\mathrm{f}6}(F)$, with imaginary parts obtained by multiplying the right-hand sides of Eqs. (79a) and (79b) by Ω. Their real parts are identified with the real parts $\mathrm{Re}[\lambda_\alpha(F)]$, for $\alpha = 1,\dots,6$, of the eigenvalues of the Jacobian matrix $\tilde{\mathsf{J}}(t)$, or $\mathsf{J}(t)$.

In conclusion, for each $\alpha = 1,\dots,6$, the fundamental Floquet exponents are constructed as

$$\begin{aligned}\lambda_{\mathrm{f}\alpha}(F) &= \mathrm{Re}[\lambda_{\mathrm{f}\alpha}(F)] + i\,\mathrm{Im}[\lambda_{\mathrm{f}\alpha}(F)] \\ &= \begin{cases} \mathrm{Re}[\lambda_\alpha(F)] + i\,\mathfrak{m}\big(\mathrm{Im}[\lambda_\alpha(F)/\Omega]\big)\Omega, & \text{if } \mathfrak{m}\big(\mathrm{Im}[\lambda_\alpha(F)/\Omega]\big) \in [0,\tfrac{1}{2}[, \\ \mathrm{Re}[\lambda_\alpha(F)] + i\,\big(\mathfrak{m}\big(\mathrm{Im}[\lambda_\alpha(F)/\Omega]\big) - 1\big)\Omega, & \text{if } \mathfrak{m}\big(\mathrm{Im}[\lambda_\alpha(F)/\Omega]\big) \in [\tfrac{1}{2},1[. \end{cases}\end{aligned} \tag{80}$$

For all the Floquet exponents, the representation $\lambda_{\alpha,\nu}(F) = \lambda_\alpha(F) - i\nu\Omega$, with $\alpha = 1,\dots,6$ and $\nu \in \mathbb{Z}$, is now available and can be used to assess the stability of the system under analysis and the onset of bifurcations.

It should be emphasized that it is *not* always possible to express the fundamental Floquet exponents as in Eq. (80); in such cases, algorithms are needed to determine them (Bentvelsen and Lazarus, 2018; Guillot et al., 2020). Yet, due to the weak coupling of the Lorentz force with the structure under study in the linearized case, our problem has the intrinsic advantage of allowing for a determination of such exponents in closed form, as shown in Remark 7. Therefore, when the procedure based on the truncated Hill matrix is employed, as in Eq. (69), the value of H for which the numerically computed fundamental Floquet exponents match those determined in closed form can be identified by direct inspection, depending on the problem parameters (see the caption of Fig. 4).

4.3. Flutter instability, secondary Hopf bifurcations, and 'phase-locking'

From the computation of $\lambda_{\mathrm{f}1},\dots,\lambda_{\mathrm{f}6}$ for selected values of the parameters c, F, B_M, and Ω, a parametric study is developed with the objective of performing the stability analysis of the system under investigation. Two main cases are addressed: the *undamped case* ($c = 0$) and the *damped case* ($c > 0$). We begin with $c = 0.1$ for the damped case, because this is one of the (dimensionless) damping coefficients that were used also by Cazzolli et al. (2020), without Lorentz force.

Before presenting the results, it is observed that Eq. (75) implies that variations in B_M do not affect the stability of the system. Indeed, although B_M influences the dynamical behavior of the system, as shown in Section 5, it does not alter the main qualitative stability results around the equilibrium configuration reported in Eq. (43). Hence, in this section, the dimensionless amplitude of the magnetic induction is fixed coherently with the 'virtual' experiment described in Section 5. In particular, $B_\mathrm{M} = 0.003$ is selected and the frequency of $B_\mathrm{h}(t)$ and $\dot{B}_\mathrm{h}(t)$ featuring in the Lorentz force is set as $\Omega = 0.5$.

4.3.1. Flutter and 'phase-locking' regimes

The real and imaginary parts of the fundamental Floquet exponents $\lambda_{\mathrm{f}1},\dots,\lambda_{\mathrm{f}6}$ are analyzed as functions of the dead load F both in the undamped case (Fig. 4(a)) and in the damped case (Fig. 4(b), with $c = 0.1$). The present findings are compared with those of Cazzolli et al. (2020), who showed that, for their structure (Fig. 1), which is subjected neither to a Lorentz force nor to any other external stimulus varying periodically in time, three distinct *stability regimes* arise, depending on the value of the dead load F (Ziegler, 1977; Bigoni and Kirillov, 2019; Cazzolli et al., 2020). These three regimes are defined by two critical values of F, which are referred to as *critical load for flutter* F_flu and *critical load for divergence* F_div, and are further particularized depending on whether or not damping is considered. While the term 'critical load for flutter' is retained in the present context, the term 'critical load for divergence' is used when no external periodic stimulus is considered and the imaginary parts of the eigenvalues vanish both in the undamped and in the damped case (see Figs. S2a and S2b in Section B of the Supplementary Material, together with the corresponding discussion).

Since $B_\mathrm{h}(t)$ and $\dot{B}_\mathrm{h}(t)$ require the tentative solution $\mathsf{Y}(t) = \mathrm{e}^{\lambda t}\mathsf{p}(t)$ introduced in Eq. (62), the notion of 'critical load for divergence' should be reformulated. As shown below, both in the undamped and in the damped case, there exists a value of F above which the imaginary parts of all the six fundamental Floquet exponents vanish, $\mathrm{Im}[\lambda_{\mathrm{f}\alpha}] = 0$, for $\alpha = 1,\dots,6$. They therefore lie within the fundamental frequency interval $[-\Omega/2,+\Omega/2[$. Bentvelsen and Lazarus (2018) termed this behavior *'locking-in'* of the fundamental Floquet exponents. Following Kuznetsov (2023), we instead refer to it as *'phase-locking'*, although we use here this term with a slightly different meaning. Accordingly, the 'critical load for divergence' is replaced by the *critical load for phase-locking* (Kuznetsov, 2023), denoted by F_loc. In spite of this change of the symbol used, it holds that $F_\mathrm{loc} = F_\mathrm{div}$. For $F \geq F_\mathrm{loc}$,

$$\mathrm{Im}[\lambda_{\mathrm{f}\alpha}] = 0, \qquad \alpha = 1,\dots,6, \tag{81}$$

whereas the corresponding non-fundamental Floquet exponents satisfy

$$\mathrm{Im}[\lambda_{\mathrm{f}(\alpha+k)}] = k\Omega, \qquad k \in \mathbb{Z}\setminus\{0\}, \qquad |k| \geq 7. \tag{82}$$

Equivalently, if the sawtooth wave is used and the fundamental frequency interval is $[0,\Omega[$, then Eq. (81) reads $\lfloor \mathrm{Im}[\lambda_{\mathrm{f}\alpha}]/\Omega \rfloor = 0$ and $\mathfrak{m}(\mathrm{Im}[\lambda_{\mathrm{f}\alpha}/\Omega]) = 0$, for $\alpha = 1,\dots,6$.

Therefore, for $F \geq F_\mathrm{loc}$, $\mathsf{Y}(t)$ becomes

$$\mathsf{Y}(t) = \textstyle\sum_{\alpha=1}^{6} y_\alpha \mathrm{e}^{\mathrm{Re}[\lambda_{\mathrm{f}\alpha}]t} \sum_{\nu=-\infty}^{+\infty} \mathsf{p}_{\nu,\alpha} \mathrm{e}^{i\nu\Omega t}, \tag{83}$$

so that the real parts of the fundamental Floquet exponents are the sole responsible for the lack of periodicity of $\mathsf{Y}(t)$.

In the undamped case, besides the two fundamental Floquet exponents that are identically zero, two exponents have negative real parts and two have positive real parts. These pairs are symmetric with respect to the F-axis, implying that $\mathsf{Y}(t)$ is unbounded as $t \to +\infty$. The damped case exhibits the same qualitative behavior, although the symmetry between the pairs with negative and positive real parts is lost.

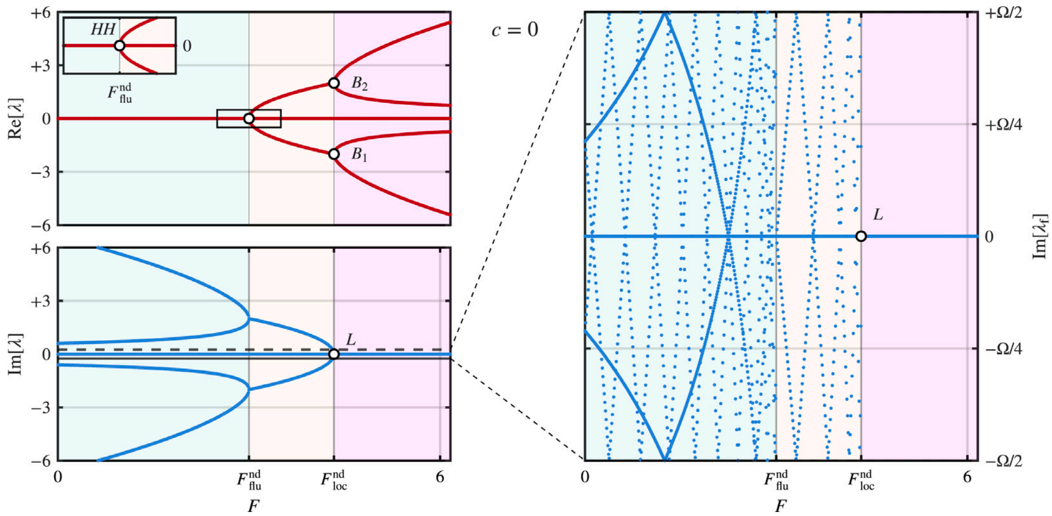

(a) *Undamped case.* (Left panel) Real parts (Re[λ]) and imaginary parts (Im[λ]) of the eigenvalues $\lambda_1, \ldots, \lambda_6$ as functions of the dimensionless dead load F, and for the dimensionless parameters $c = 0$, $B_{\rm M} = 0.003$, and $\Omega = 0.5$. (Right panel) Imaginary parts of the *fundamental Floquet exponents*.

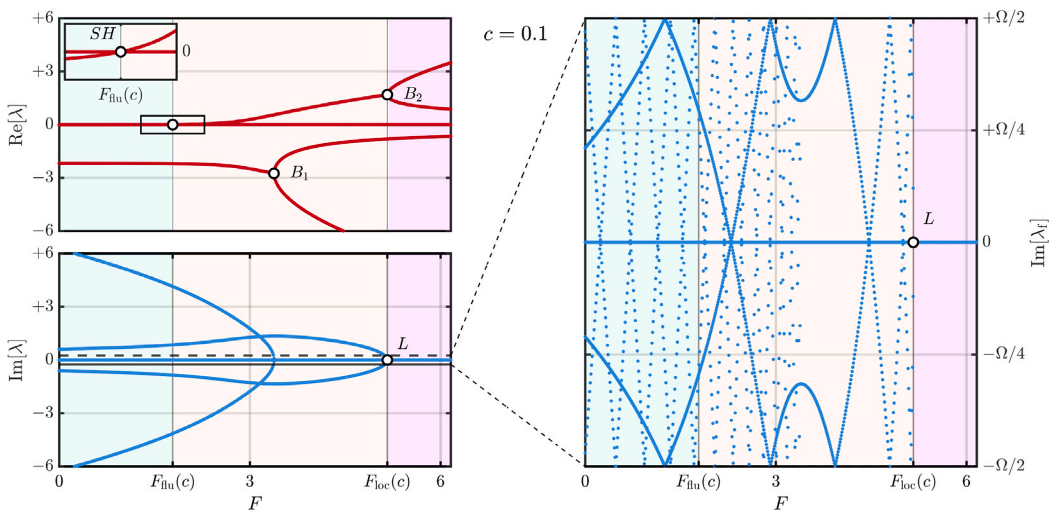

(b) *Damped case.* (Left panel) Real parts (Re[λ]) and imaginary parts (Im[λ]) of the eigenvalues $\lambda_1, \ldots, \lambda_6$ as functions of the dimensionless dead load F, and for the dimensionless parameters $c = 0.1$, $B_{\rm M} = 0.003$, and $\Omega = 0.5$. (Right panel) Imaginary parts of the *fundamental Floquet exponents*.

Fig. 4. (Left panels) The Re[λ]-F curves and Im[λ]-F curves coincide with those obtained in the absence of the Lorentz force. Here, $B_{\rm M}$ and Ω play no role. In the Re[λ]-F curves, the points HH (Hamiltonian Hopf bifurcation, undamped case) and SH (secondary Hopf bifurcation, damped case), as well as B_1 and B_2, coincide with those obtained in the absence of the Lorentz force. In the Im[λ]-F curves, the point L, corresponding to the onset of the phase-locking regime, coincides with the lower bound of the divergence regime in (Cazzolli et al., 2020). (Right panels) The magnified panels *do not represent zoomed-in views* of the values of Im[λ] within the interval $[-\Omega/2, +\Omega/2[$. Rather, they enlarge this interval to show the distribution of the imaginary parts of the *fundamental Floquet exponents*, computed as described in Remark 7. Both figures are generated using values of F spaced by $\Delta F = 0.01$. When the Hill method is employed, the same plots are obtained with $H = 14$ in the undamped case and with $H = 13$ in the damped case.

Looking at the right panel of Fig. 4(a) (undamped case, $c = 0$), we notice that, for each value of $F \in [0, F_{\rm flu}^{\rm nd}[$, five distinct points are found (the superscript 'nd' means 'non-dissipative'). The point on the horizontal axis, Im[λ] = 0, is associated with the eigenvalues $\lambda_5 = \lambda_6 = 0$ of the Jacobian $\mathsf{J}(t)$, and must thus be counted twice. The remaining four distinct points, instead, are associated with the imaginary parts of the eigenvalues $\lambda_1, \lambda_2, \lambda_3, \lambda_4$, which are distinct from one another, as shown in the bottom-left panel of Fig. 4(a). Moreover, for $F \in [F_{\rm flu}^{\rm nd}, F_{\rm div}^{\rm nd}[= [F_{\rm flu}^{\rm nd}, F_{\rm loc}^{\rm nd}[$, only three distinct points are found for each value of F. This is because, besides the point on the horizontal axis (which has to be counted twice for the reason explained above), also the other two points correspond to overlapping imaginary parts of the eigenvalues of $\mathsf{J}(t)$; see, again, the bottom-left panel of Fig. 4(a). Finally, for $F > F_{\rm div}^{\rm nd} = F_{\rm loc}^{\rm nd}$, each value of F yields only one point in the right panel of Fig. 4(a) because the imaginary parts of all the eigenvalues are zero. This occurrence is consistent with the *'phase-locking'* regime (Bentvelsen and Lazarus, 2018; Kuznetsov, 2023). Analogous considerations apply also for the damped case ($c = 0.1$, Fig. 4(b)), although the eigenvalues of $\mathsf{J}(t)$ overlap for different values of $F \in [F_{\rm flu}(c), F_{\rm loc}(c)[$.

Remark 8 (*A relevant property of the Lorentz force*).

A consequence of Corollary 1 is that the real parts of the fundamental Floquet exponents coincide with those of the eigenvalues of the Jacobian matrix associated with the mechanical device studied by Cazzolli et al. (2020). Therefore, the flutter regime begins at the same critical values of the dead load F found by Cazzolli et al. (2020), both in the undamped and in the damped case. In the work by Cazzolli et al. (2020), the onset of flutter is associated with a Hamiltonian Hopf bifurcation for $c = 0$ and with a Hopf bifurcation for $c > 0$; see Section B of the Supplementary Material. Our results predict the same bahaviors because both bifurcations occur when the same specific conditions on the real parts of the eigenvalues of the Jacobian matrix are satisfied.

The same argument applies to the 'phase-locking' regime, which begins at the same values of the dead load F as the divergence regime identified by Cazzolli et al. (2020), both for $c = 0$ and for $c > 0$ (specifically, $c = 0.1$). This equivalence is a notable consequence of the Lorentz force and, in particular, of the way in which its associated matrix L_e enters the problem through the effective damping and stiffness matrices, $\mathsf{C}_{\rm eff}$ and $\mathsf{K}_{\rm eff}$, defined in Eqs. (51a) and (51b). A detailed calculation of the eigenvalues is provided in Section B of the Supplementary Material. Moreover, Fig. S1 of the Supplementary Material provides a heuristic explanation of why the sparsity of L_e does not affect the eigenvalues and, consequently, the onset of flutter or phase-locking.

As reported above, in the undamped case ($c = 0$, Fig. 4(a)) the *critical load for flutter* and the *critical load for phase-locking* are denoted as $F^{\rm nd}_{\rm flu}$ and $F^{\rm nd}_{\rm loc}$, with 'nd' standing for 'non-dissipative'. The system is *marginally stable* for $F \in [0, F^{\rm nd}_{\rm flu}[$, experiences *flutter instability* for $F \in [F^{\rm nd}_{\rm flu}, F^{\rm nd}_{\rm loc}[$, and enters the *phase-locking regime* for $F \in [F^{\rm nd}_{\rm loc}, +\infty[$.

The values $F^{\rm nd}_{\rm flu}$ and $F^{\rm nd}_{\rm loc}$ are

$$F^{\rm nd}_{\rm flu} = 3, \qquad F^{\rm nd}_{\rm loc} = 13/3 \simeq 4.3333. \tag{84}$$

In the damped case ($c > 0$), the critical load for flutter and the critical load for phase-locking can both be expressed as functions of the damping parameter c. These functions are denoted as $F_{\rm flu}(c)$ and $F_{\rm loc}(c)$, respectively, and, for any fixed $c > 0$, we observe a region of *stability* for $F \in [0, F_{\rm flu}(c)[$, a region of *flutter instability* for $F \in [F_{\rm flu}(c), F_{\rm loc}(c)[$, and the appearance of *phase-locking* (Kuznetsov, 2023) for $F \in [F_{\rm loc}(c), +\infty[$. In agreement with Remark 8, $F_{\rm flu}(c)$ and $F_{\rm loc}(c)$ correspond to the same threshold loads characterizing the case in which the Lorentz force is absent, provided that the 'phase locking' regime is identified with the 'divergence' regime. Specifically, the value $F_{\rm flu}(c)$ is determined by the analytical expression (Ziegler, 1977; Bigoni and Kirillov, 2019; Cazzolli et al., 2020)

$$F_{\rm flu}(c) = \frac{39}{22} + \frac{4c^2}{3}, \tag{85}$$

and $F_{\rm loc}(c)$ is the analogue of $F_{\rm div}(c)$, defined when the forces do not vary explicitly in time.

As depicted in Fig. 4(b) for $c = 0.1$, $F_{\rm flu}(c)$ and $F_{\rm loc}(c)$ are

$$F_{\rm flu}(c = 0.1) \simeq 1.7861, \qquad F_{\rm loc}(c = 0.1) \simeq 5.1623. \tag{86}$$

The derivation of the critical loads, Eqs. (85) and (86), is reported in Section B of the Supplementary Material.

Remark 9 (*The Ziegler paradox*).

The *Ziegler paradox* (Kirillov and Verhulst, 2010; Kirillov, 2013; Bigoni and Kirillov, 2019) is found in the structure under analysis. It consists in $F^{\rm nd}_{\rm flu}$ exceeding the infimum of $F_{\rm flu}(c)$ for $c > 0$,

$$F^{\rm nd}_{\rm flu} = 3 > F^{0^+}_{\rm flu} := \lim_{c\to 0^+} F_{\rm flu}(c) = \inf_{c>0} F_{\rm flu}(c) = \frac{39}{22} \approx 1.7727\,. \tag{87}$$

Therefore, there exist values of $c > 0$ such that $F_{\rm flu}(c) \in]F^{0^+}_{\rm flu}, F^{\rm nd}_{\rm flu}]$. Thus, for positive damping coefficients, flutter may occur at dead loads lower than or equal to the critical load of the non-dissipative system.

4.3.2. Characterization of the bifurcations: Secondary Hopf bifurcations and quasi-periodicity

The parametric analysis of the real parts of the fundamental Floquet exponents as F increases reveals the occurrence of a Hopf-type bifurcation marking the onset of flutter. The corresponding imaginary parts provide additional insight into the system dynamics and allow for a more detailed characterization of the bifurcation (Guskov and Thouverez, 2012; Bentvelsen and Lazarus, 2018; Guillot et al., 2020).

Following Guillot et al. (2020), each Floquet exponent $\lambda_{\alpha,\nu} = \lambda_\alpha - i\nu\Omega$, where $\alpha = 1,\dots,6$ and $\nu \in \mathbb{Z}$, is associated with the *Floquet multiplier* $\zeta_{\alpha,\nu} := e^{(2\pi/\Omega)\lambda_{\alpha,\nu}}$. It is obtained by evaluating the factor $e^{\lambda t}$ in Eq. (62) for $\lambda = \lambda_{\alpha,\nu}$ and over one period of $B_{\rm h}(t)$ and $\dot{B}_{\rm h}(t)$, namely at $t = T = 2\pi/\Omega$,

$$\begin{aligned}\zeta_{\alpha,\nu} &:= e^{\frac{2\pi}{\Omega}\lambda_{\alpha,\nu}} = e^{\frac{2\pi}{\Omega}\{{\rm Re}[\lambda_\alpha]+i({\rm Im}[\lambda_\alpha]-\nu\Omega)\}}\\ &= e^{\frac{2\pi}{\Omega}{\rm Re}[\lambda_\alpha]}\left\{\cos\left(\tfrac{2\pi}{\Omega}{\rm Im}[\lambda_\alpha]\right) + i\sin\left(\tfrac{2\pi}{\Omega}{\rm Im}[\lambda_\alpha]\right)\right\}.\end{aligned} \tag{88}$$

Since cosine and sine are periodic functions, only six Floquet multipliers are uniquely defined and are in a one-to-one relation with the roots $\lambda_1,\dots,\lambda_6$ of the characteristic polynomial $P(\lambda)$, Eq. (57). Therefore, the subscript 'ν' can be dropped from $\zeta_{\alpha,\nu}$, which is rewritten as ζ_α. Moreover, the following relation holds

$$|\zeta_\alpha| = e^{\frac{2\pi}{\Omega}{\rm Re}[\lambda_\alpha]}, \qquad \alpha = 1,\dots,6. \tag{89}$$

In fact, since each λ_α has to be interpreted as a function of the dead load F, Figs. 4(a) and 4(b) (left panels), the Floquet multiplier can be rewritten as $\zeta_\alpha(F) = e^{(2\pi/\Omega)\lambda_\alpha(F)}$ and can be interpreted as a reparameterization of the diagram of the corresponding α-th root $\lambda_\alpha(F)$ of the characteristic polynomial $P(\lambda)$ in the complex plane. The introduction of $\zeta_\alpha(F)$ is useful to visualize the bifurcations occurring in the problem under analysis.

The real and the imaginary parts of $\zeta_1,\dots,\zeta_6$ are reported in Fig. 5(a) for the undamped case, $c = 0$. To facilitate the visualization, only the semi-axis of the non-negative real parts of $\zeta_1,\dots,\zeta_6$ is shown for F varying in a neighborhood of $F^{\rm nd}_{\rm flu}$, such that F is sufficiently smaller than $F^{\rm nd}_{\rm loc}$. In the following, $\mathscr{U}^-(F^{\rm nd}_{\rm flu})$ and $\mathscr{U}^+(F^{\rm nd}_{\rm flu})$ denote the left and the right neighborhood of $F^{\rm nd}_{\rm flu}$, respectively, and it is assumed that $\mathscr{U}^-(F^{\rm nd}_{\rm flu}) \cap \mathscr{U}^+(F^{\rm nd}_{\rm flu}) = \{F^{\rm nd}_{\rm flu}\}$. The point at which the unit circle intersects the positive real axis corresponds to the identically zero roots $\lambda_5 = \lambda_6 = 0$; indeed, $\zeta_5 = \zeta_6 = e^{(2\pi/\Omega)0} = 1 + i0$.

The points on the unit circle correspond to the values of $F \in \mathscr{U}^-(F^{\rm nd}_{\rm flu})$. For these values, ${\rm Re}[\lambda_\alpha] = 0$ for $\alpha = 1,\dots,4$, and, since λ_1 and λ_4 as well as λ_2 and λ_3 are both pairs of complex conjugate eigenvalues, it follows that ${\rm Im}[\lambda_1]$ and ${\rm Im}[\lambda_2]$ are strictly positive, while ${\rm Im}[\lambda_3]$ and ${\rm Im}[\lambda_4]$ are strictly negative (see Fig. S2a of the Supplementary Material). Hence, the points in the complex plane associated with $\zeta_1 = e^{(2\pi/\Omega)\lambda_1}$ and $\zeta_2 = e^{(2\pi/\Omega)\lambda_2}$ lie on the quarter-circle in the first quadrant, whereas those associated with $\zeta_3 = e^{(2\pi/\Omega)\lambda_3}$ and $\zeta_4 = e^{(2\pi/\Omega)\lambda_4}$ lie on the quarter-circle in the fourth quadrant. Note the conjugacy relations $\zeta_1 = \bar{\zeta}_4$ and $\zeta_2 = \bar{\zeta}_3$.

A more distinctive configuration of the points occurs for $F \in \mathscr{U}^+(F^{\rm nd}_{\rm flu})$, as it is associated with the onset of flutter through a *Hamiltonian Hopf bifurcation*, as discussed below.

For $F \in \mathscr{U}^+(F^{\rm nd}_{\rm flu})$, the eigenvalues λ_1 and λ_4 (see Fig. S2a of the Supplementary Material) have negative real part, which implies that $e^{(2\pi/\Omega){\rm Re}[\lambda_1]}$ and $e^{(2\pi/\Omega){\rm Re}[\lambda_4]}$ are both smaller than unity. In Fig. 5(a), the points lying inside the unit semicircle in the complex plane correspond to ζ_1 and ζ_4. Moreover, because λ_1 and λ_4 are complex conjugates, their imaginary parts have opposite signs. Accordingly, as F increases beyond $F^{\rm nd}_{\rm flu}$, the corresponding multipliers ζ_1 and ζ_4 move symmetrically away from the real axis and toward the origin in Fig. 5(a). Note that, because λ_1 and λ_4 are a complex conjugate pair, the corresponding Floquet multipliers $\zeta_1 = e^{(2\pi/\Omega)\lambda_1}$ and $\zeta_4 = e^{(2\pi/\Omega)\lambda_4}$ are also complex conjugates.

The eigenvalues λ_2 and λ_3 (see Fig. S2a of the Supplementary Material) have positive real parts for $F \in \mathscr{U}^+(F^{\rm nd}_{\rm flu})$, and imply that $e^{(2\pi/\Omega){\rm Re}[\lambda_2]}$ and $e^{(2\pi/\Omega){\rm Re}[\lambda_3]}$ are both greater than unity, which is why the corresponding points in Fig. 5(a), namely $\zeta_2 = e^{(2\pi/\Omega)\lambda_2}$ and $\zeta_3 =$

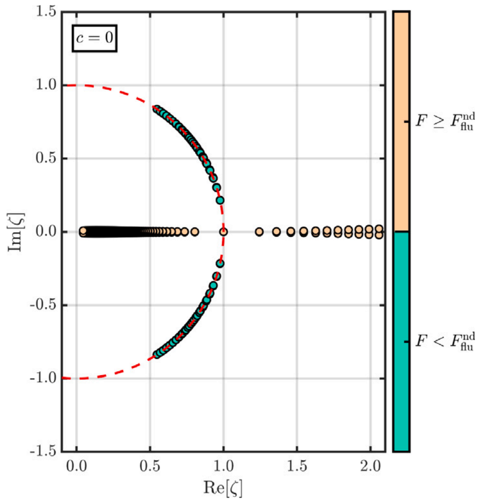

(a) Real and imaginary parts of the Floquet multipliers as F varies in a neighborhood of the critical flutter load $F_{\text{flu}}^{\text{nd}}$ in the undamped case. The trajectories of the Floquet multipliers characterize a Hamiltonian Hopf bifurcation.

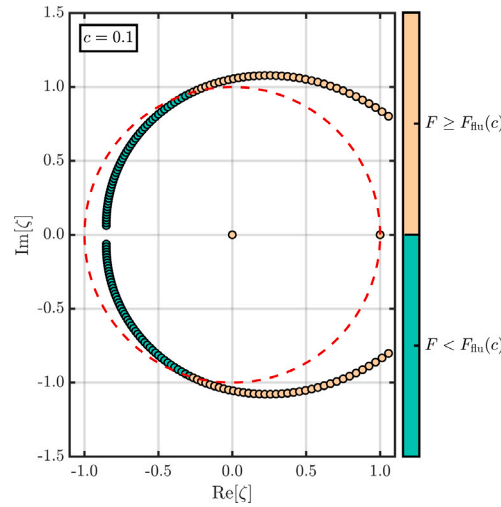

(b) Real and imaginary parts of the Floquet multipliers as F varies in a neighborhood of the critical flutter load $F_{\text{flu}}(c = 0.1)$ in the damped case. The trajectories of the Floquet multipliers characterize a secondary Hopf bifurcation.

Fig. 5. The Floquet multipliers in the complex plane for the undamped case (a) and the damped case (b).

$\mathrm{e}^{(2\pi/\Omega)\lambda_3}$, move away from the unit circle toward its exterior. Also in this case, because λ_2 and λ_3 are complex conjugates, their imaginary parts have opposite signs. Consequently, as F increases beyond $F_{\text{flu}}^{\text{nd}}$, the corresponding multipliers ζ_2 and ζ_3 separate symmetrically in the complex plane. The multipliers ζ_2 and ζ_3 are themselves complex conjugates.

The real and the imaginary parts of $\zeta_1, \ldots, \zeta_6$ are reported in Fig. 5(b) for the damped case, $c = 0.1$. For this value of damping, the point $1 + i0$ corresponds to the Floquet multipliers $\mathrm{e}^{(2\pi/\Omega)\lambda_5} = \mathrm{e}^{(2\pi/\Omega)\lambda_6}$, because the eigenvalues λ_5 and λ_6 are both identically zero.

For $F \in \mathscr{U}^-(F_{\text{flu}}(c))$, the complex-conjugate eigenvalues λ_1 and λ_4 have equal negative real parts, $\text{Re}[\lambda_1] = \text{Re}[\lambda_4]$, which are more negative than the equal real parts of the complex-conjugate pair λ_2 and λ_3, $\text{Re}[\lambda_2] = \text{Re}[\lambda_3]$; see Fig. S2b of the Supplementary Material. Consequently, the Floquet multipliers ζ_1 and ζ_4 have smaller moduli and lie close to the origin of the complex plane.

More importantly, since the real part of λ_2 and λ_3 is negative for $F \in \mathscr{U}^-(F_{\text{flu}}(c)) \setminus \{F_{\text{flu}}(c)\}$ and zero for $F = F_{\text{flu}}(c)$, the complex conjugate pair ζ_2 and ζ_3, defined by Eq. (88) for $\alpha = 2, 3$, traces two loci in the complex plane that originate inside the unit circle and intersect it at $F = F_{\text{flu}}(c)$.

For $F \in \mathscr{U}^+(F_{\text{flu}}(c))$, the real parts of λ_1 and λ_4 become increasingly negative, causing the corresponding Floquet multipliers ζ_1 and ζ_4 to move toward the origin of the complex plane. However, the real parts of λ_2 and λ_3 become positive. Consequently, the corresponding Floquet multipliers ζ_2 and ζ_3 cross the unit circle and trace two symmetric spiral branches: the branch associated with λ_2 evolves counterclockwise, whereas that associated with λ_3 evolves clockwise. This crossing of the unit circle by ζ_2 and ζ_3 characterizes the occurrence of a *secondary Hopf bifurcation* (Guskov and Thouverez, 2012; Bentvelsen and Lazarus, 2018; Guillot et al., 2020).

The nature of the system and of the applied forces prevents the emergence of the limit cycles and periodic asymptotic solutions associated with a standard Hopf bifurcation. Instead, the occurrence of a secondary Hopf bifurcation leads to quasi-periodic asymptotic solutions, which are observed after sufficiently long times.

5. Post-critical behavior: the Lorentz force influences the nonlinear dynamics

In this section, we aim to assess how the Lorentz force can influence the post-critical behavior of the device both in Case I and in Case II.

As anticipated in the preamble of Section 4, we now restore the physical dimensions to the quantities that we made dimensionless. We do this to provide context for the following numerical test.

5.1. The scenario of a soft bodied microrobot for biological applications

Among the various designs that are often employed in microrobotics (Xu and Xu, 2024), we model our microrobot as a continuous rod (discretized by the double pendulum) attached to a small mass (the cart), having both viscous and elastic material properties (the viscoelastic hinges), and a concentrated electric charge at one end (the point charge $\mathfrak{e}$ in D). Specifically, we assume the rod to be made of an idealized rubber-like material with density $\rho = 10^3\,\text{kg/m}^3$ and Young modulus $E_{\text{Y}} = 10^6\,\text{Pa}$ (Kim et al., 2019).

The device's geometry is characterized by slender bars, with length $\ell = 10\,\mu\text{m}$, width $w = 1\,\mu\text{m}$, and thickness $\tau = 0.1\,\mu\text{m}$, so that their volumes and moments of inertia read $V = \ell w \tau$ and $J = (1/12)\tau^3 w$, respectively (the aspect ratio of the bars and the notation are taken from Alouges et al. (2015)). Consequently, the mass of one bar reads $m = \rho V$, while the stiffness coefficient k is computed as $k = E_{\text{Y}} J/\ell$ (Alouges et al., 2015). Once k is obtained, the damping coefficient c (modeling the overall viscous behavior of the robot) is selected coherently with the work by Cazzolli et al. (2020). Hence, c is chosen in such a way that the dimensionless damping coefficient of Eq. $(45\text{b})_2$ is $c/(\ell\sqrt{mk}) = 0.1$ (cfr. Section 4).

The value of the dead load F is in line with the typical thrust and propulsion forces reported for microrobots in biological applications (Zhang et al., 2009). Specifically, we choose the value $F = 1.6\,\text{pN}$, for which flutter can occur, since $F \simeq 1.1\,F_{\text{flu}}(c)$.

The solenoid is assumed to be sufficiently long, with height at least four times its diameter (Rousseaux et al., 2008), and radius $R_{\text{s}} = 5\,\text{cm}$, and capable of generating a magnetic induction field of maximum amplitude $B_{\text{M}} = 1\,\text{T}$. We emphasize that this value of B_{M} is higher than those typically used to study, for instance, the motility of micro-

Table 1
Numerical values used for the simulations.

Parameter	Symbol	Value	Unit	Ref.
Length of each bar	ℓ	10	μm	Zhang et al. (2009), Shen et al. (2023)
Mass of each bar	m	0.001	ng	Kim et al. (2019)
Mass of the cart	m_c	0.01	ng	–
Spring stiffness	k	10	pN μm	Alouges et al. (2015)
Damping coefficient	c	$\{0.05, 0.10, 0.20\} \times 10^{-3}$	pN μm s^{-1}	Cazzolli et al. (2020)
Dead load	F	1.6	pN	Zhang et al. (2009)
Electric charge	$\mathfrak{c}$	0.03	pC	Brown and Poon (2014)
Solenoid radius	R_s	5	cm	Montgomery (1969), Xu et al. (2025)
Magnetic amplitude	B_M	$\{0.1, 1\}$	T	Martel et al. (2007), Xu et al. (2025)
Magnetic frequency	Ω	$\{5, 10\}$	kHz	Rousseaux et al. (2008)

or nano-robots in biological environments (usually around the order of magnitude of 10^{-3} T (Zhang et al., 2009)). Although the value $B_M = 1$ T may be considered extreme, we adopt it to make the Lorentz force comparable to the propulsion forces (dead load) considered by Zhang et al. (2009) and to the follower force. In fact, solenoids with relatively small diameters can reach MRI-level magnetic induction fields (Montgomery, 1969; Xu et al., 2025), and can be used for micro-motility applications (Martel et al., 2007). Nevertheless, as a precautionary measure, a numerical test is also performed, using a lower value of the magnetic induction field and we find that the results are qualitatively the same as those obtained for $B_M = 1$ T, Table 1.

The magnetic induction field is assumed to be sinusoidal in time as reported in Eq. (59a). In the following sections, we examine the cases $\Omega = 5$ kHz and $\Omega = 10$ kHz, consistent with the frequency range adopted by Rousseaux et al. (2008) to justify the low-frequency approximation for the vector potential $\boldsymbol{A}$.

The point charge concentrated at the skate is in agreement with the effective net charge of micro-metric entities in aqueous media, as documented in the electrokinetic study by Brown and Poon (2014). We select $\mathfrak{c} = 0.03$ pC rather than the more natural value $\mathfrak{c} = 0.01$ pC to amplify the influence of the Lorentz force, without allowing the magnetic field amplitude to exceed 1 T.

Remark 10 (*Implementation details*).
The simulations are performed by numerically solving the Cauchy problem defined by

$$\dot{\mathsf{Y}} = \mathsf{f}(\mathsf{Y}, t; F), \qquad \mathsf{Y}(t = 0) = \mathsf{Y}_0 = \{0\ 0\ X_{c0}\ 0\ 0\ 0\}^{\mathrm{T}}, \tag{90}$$

where Y_0 is an array of initial conditions (see also Eq. (S38) of Section C of the Supplementary Material). The derivation of Eq. (90) follows that of Eq. (54). However, the Schur complement procedure is applied to the nonlinear problem defined by Eqs. (34a)–(34c) and (36), rather than to the linearized equations. The resulting expressions are then recast in state-variable form. Details are reported in Section C of the Supplementary Material. In Case I, X_{c0} is chosen as a small deviation from X_{ce} in Eq. (43), while in Case II it is $X_{c0} > R_s$. Null initial velocities are assumed. Numerical simulations are performed in MATLAB (The MathWorks, Inc., 2024) by using the adaptive Runge–Kutta (4,5) scheme implemented in the `ode45` function for time integration (Shampine and Reichelt, 1997).

5.2. Case I: Lorentz force, flutter, and confinement of the device's horizontal motion

We consider the case in which the device is fully contained within the solenoid and the cart is initially positioned at $X_{c0} = -1.5\ell$ with zero initial velocities. For this initial state, corresponding to $|X_{c0} - X_{ce}| = 0.5\ell$, flutter occurs under the action of the dead load F as induced by the nonzero torque exerted by the electric part of the Lorentz force. This phenomenon does not arise in the problem studied by Cazzolli et al. (2020), where flutter is triggered only by perturbations of the angles θ_1 or θ_2, or of their associated angular velocities, provided that the dead load F, applied to the cart, is sufficiently strong. Indeed, if the initial condition Y_0 specified in Eq. $(90)_2$ were imposed on the system studied by Cazzolli et al. (2020), the system would remain at equilibrium and no motion would occur (see Remark 2). Note that the state Y_0 is obtained from that portrayed in Fig. 3(b) by placing the concentrated mass of the second bar at the origin of the reference frame.

We begin with the frequency $\Omega = 5$ kHz, represented in Fig. 6 by the solid blue line marked with diamonds. Fig. 6(a) shows that for $\Omega = 5$ kHz the motion of the cart, described by X_c, exhibits oscillations around a *main, roughly linear, trend*. In spite of the different setting considered in our work, this result is similar to what was found in the paper by Cazzolli et al. (2020), in which the cart advances on a large scale with a mean velocity, but it experiences oscillations around such mean velocity on a smaller scale (see the top left panel of Fig. 12 of Cazzolli et al. (2020)). Regarding the large scale motion, the Lorentz force seems not to affect significantly the dynamics of the cart: the cart moves away from the solenoid center with a comparatively large and approximately constant mean velocity of about 260 μm s^{-1}, thereby covering about 13 body lengths (2ℓ) per second. However, while the cart's small scale oscillations in our work and in that by Cazzolli et al. (2020) are comparable to each other in the first instants of our simulation (see the zoomed-in region labeled with 'A' in Fig. 6(a)), they are modified by the Lorentz force over time, as the device advances into regions in which the Lorentz force is stronger (see the zoomed-in regions B and C in Fig. 6(a)).

Figs. 6(b) and 6(c) show the phase portraits of θ_1 and θ_2 for the case $\Omega = 5$ kHz and over the time windows [0 s, 0.2 s] and [0 s, 7 s], respectively. For brevity, the phase portraits corresponding to the intermediate time interval [0 s, 2 s] are not shown.

The increasing amplitude of the oscillations of X_c should be compared with the phase plots of θ_1 and θ_2 in Figs. 6(b) and 6(c), and, in particular, with the progressive clustering of the orbits, as time goes by, from Fig. 6(b) (corresponding to the region A) to Fig. 6(c) (corresponding to the region C). Our conclusion is that the secondary Hopf bifurcation, rather than resulting into a stable limit cycle, is characterized by an almost quasi-periodic behavior.

A different situation occurs for $\Omega = 10$ kHz. At this frequency, and with reference to the solid red line marked with circles in Fig. 6(a), the device no longer experiences a motion similar to that reported by Cazzolli et al. (2020). Indeed, although the cart initially advances as in the case $\Omega = 5$ kHz (and thus as predicted by Cazzolli et al. (2020)), exhibiting micro-oscillations in the evolution of X_c (see the zoomed-in regions D, E, and F of Fig. 6(a)), the increasing Lorentz force causes a qualitative change in the motion. The zoomed-in regions D, E, and F in Fig. 6(a) show that X_c oscillates around a *non-linear trend* and that, in this case, the oscillations gain a much more marked two-scale character with increasing time (from D to F). For $t \geq 7$ s, the cart swings in a bounded region of space, without appreciable further advancement, thereby suggesting an average-in-time balance among the dead load, the follower force, and the Lorentz force. This behavior implies a confinement of the device in space. Also in this case, the oscillations of the cart are to be compared with the progressive

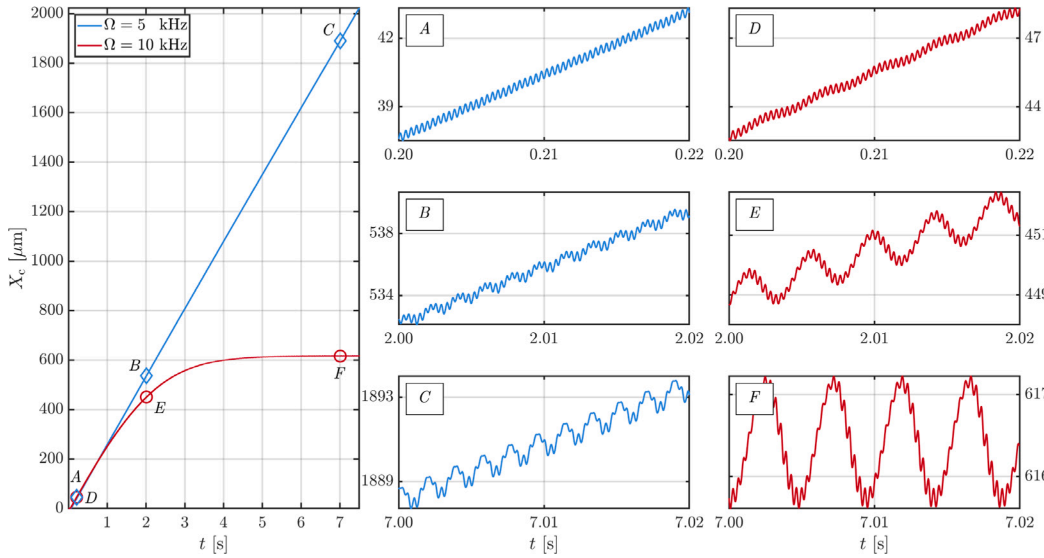

(a) Time history of X_c for $\Omega = 5\,\text{kHz}$ (blue line with diamonds) and for $\Omega = 10\,\text{kHz}$ (red line with circles).

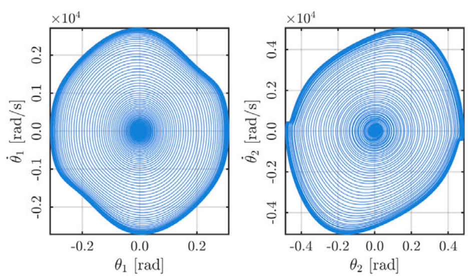

(b) Phase portraits of θ_1 and θ_2, for $\Omega = 5$ kHz, over the interval $[0\ \text{s}, 0.2\ \text{s}]$, ending with the zoomed-in region A.

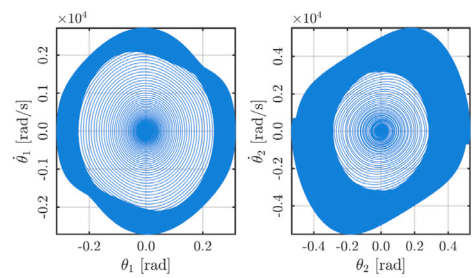

(c) Phase portraits of θ_1 and θ_2, for $\Omega = 5\,\text{kHz}$, over the interval $[0\ \text{s}, 7\ \text{s}]$, ending with the zoomed-in region C.

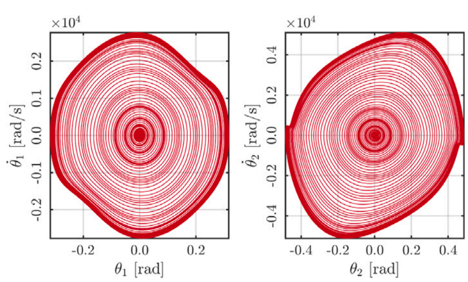

(d) Phase portraits of θ_1 and θ_2, for $\Omega = 10\,\text{kHz}$, over the interval $[0\ \text{s}, 0.2\ \text{s}]$, ending with the zoomed-in region D.

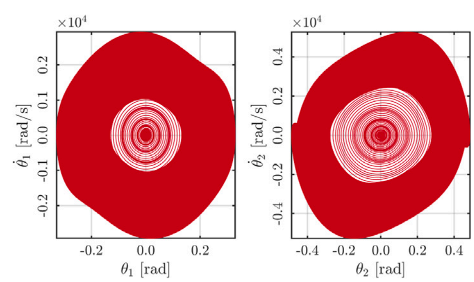

(e) Phase portraits of θ_1 and θ_2, for $\Omega = 10$ kHz, over the interval $[0\ \text{s}, 7\ \text{s}]$, ending with the zoomed-in region F.

Fig. 6. Time history of X_c and phase portraits of θ_1 and θ_2 concerning the parametric study for variable Ω conducted for Case I and representing the motion induced by flutter instability on a movable double pendulum with electrically charged nonholonomic constraint and embedded in a magnetic field.

thickening of the clusters of orbits reported in Figs. 6(d) and 6(e), which show the phase portraits of θ_1 and θ_2 for the case $\Omega = 10\,\text{kHz}$ and over the time windows $[0\ \text{s}, 0.2\ \text{s}]$ and $[0\ \text{s}, 7\ \text{s}]$, respectively. Again, the agglomeration of orbits seems to indicate the tendency of the system towards quasi-periodicity rather than towards limit cycles.

The increasing impact of the Lorentz force on the flutter instability is also reflected in the phase diagrams of θ_1 and θ_2. Figs. 6(c) and 6(e) show that, in contrast to the behavior reported by Cazzolli et al. (2020), the phase portraits of θ_1 and θ_2 do not converge to single closed orbits, as is the case when stable limit cycles exist. As time progresses, the simulations predict the formation of progressively larger regions, or 'bands', of trajectories in the corresponding phase spaces. This behavior is likely due to the modulations induced by the Lorentz force (Figs. 6(c) and 6(e)), and is more pronounced in the case with $10\,\text{kHz}$, since the oscillations of the cart around the main trend are stronger than for $\Omega = 5\,\text{kHz}$.

Lastly, we find it worth mentioning that, both for $\Omega = 5\,\text{kHz}$ (region C, corresponding to $t = 7$ s) and for $\Omega = 10\,\text{kHz}$ (regions D, E, and F) the Lorentz force seems to induce three-scale dynamics: a main trend, which is linear for $\Omega = 5\,\text{kHz}$ and nonlinear for $\Omega = 10\,\text{kHz}$, 'slow' oscillations, and 'fast' oscillations. The regions C and E of Fig. 6(a) are those in which this phenomenon is best displayed.

Lowering the amplitude of the magnetic induction field. In the simulations presented so far, the amplitude of the magnetic induction field was assumed to be $B_M = 1$ T. Now the post-critical behavior of the device is

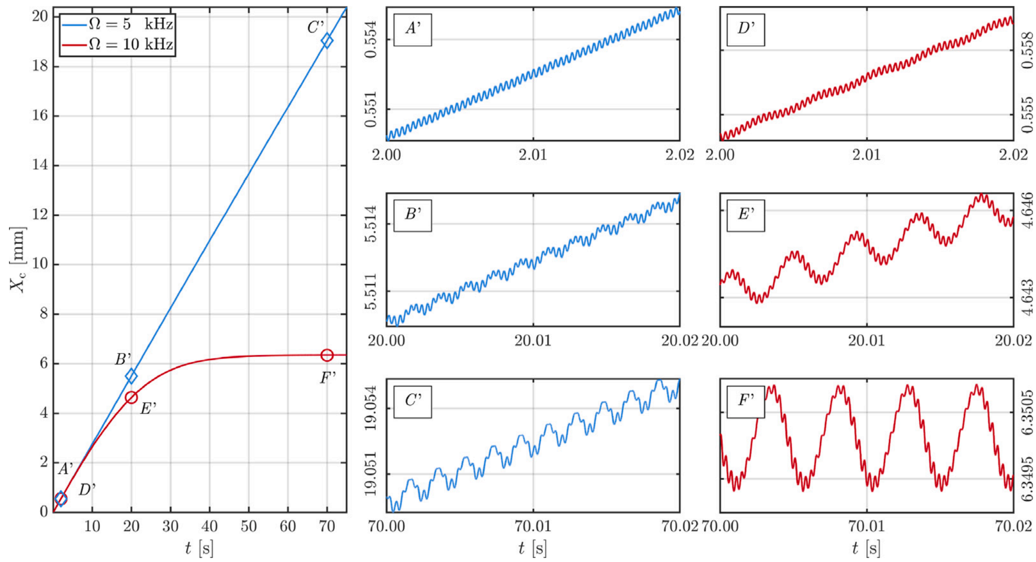

Fig. 7. Time history of X_c concerning the same parametric study as conducted in Fig. 6. Here, the strength of the magnetic induction field is selected to be $B_M = 0.1$ T, from which it follows that the global behavior of the device is maintained. However, it occurs on increased length- and time-scales.

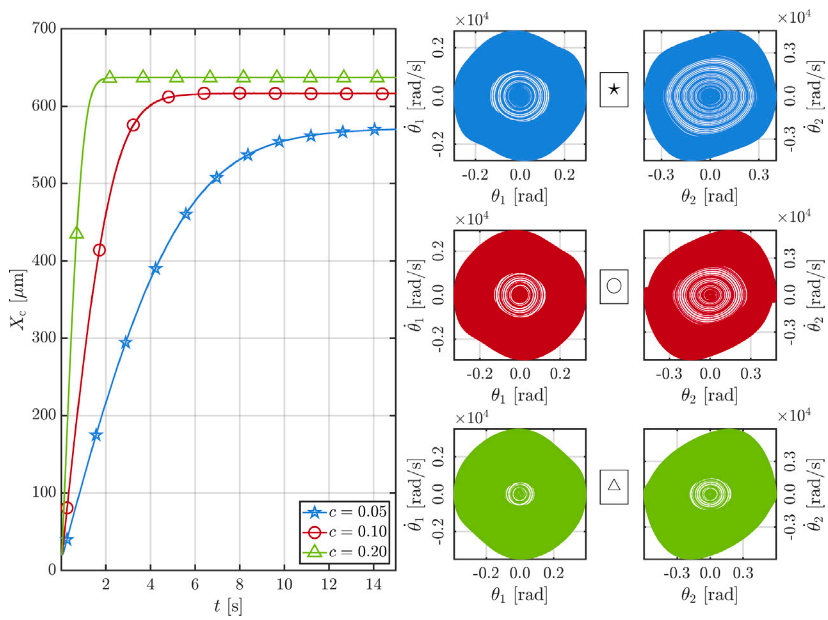

Fig. 8. Time history of X_c and phase portraits of θ_1 and θ_2 over the time interval [0 s, 14 s] for the same parametric study as conducted in Fig. 6. Here, the strength of the magnetic induction field is selected to be $B_M = 1$ T; other values of parameters are $\Omega = 10$ kHz and $F = 1.6$ pN.

analyzed for a smaller value of B_M. Specifically, $B_M = 0.1$ T is selected and the corresponding simulations are reported in Fig. 7. Comparison of Figs. 6 and 7 reveals that the post-critical behavior of the system shares the same main qualitative features observable for $B_M = 1$ T, such as the presence of micro-oscillations in the cart's trajectory, the onset of quasi-periodic orbits (data not shown), and the nonlinear motion of the cart for $\Omega = 10$ kHz. However, such behaviors are observed for time- and length-scales different from those characterizing the case $B_M = 1$ T. In fact, since switching from $B_M = 1$ T to $B_M = 0.1$ T implies decreasing the magnitude of the Lorentz force by a factor of 10, the time- and length-scales needed by the system to start exhibiting the behaviors shown in Fig. 6(c)–6(e) have to increase by a factor of 10. Although $B_M = 0.1$ T is *still* two orders of magnitude above the values found in the literature for microrobots (Zhang et al., 2009), Fig. 7 seems to suggest that, qualitatively, the behaviors reported in Fig. 6(c)–6(e) could be achieved for lower values of B_M just by increasing the simulation time. Further investigations could either confirm or rebut this claim.

Parametric investigation of the damping coefficient. In Fig. 8, the post-critical behavior is investigated for three choices of the dimensionless damping coefficient, $c \in \{0.05, 0.10, 0.20\}$, while setting $\Omega = 10$ kHz, $B_M = 1$ T, and $F = 1.6$ pN. Such value of F implies $F/F_{flu}(c = 0.05) \simeq 1.106$, $F/F_{flu}(c = 0.10) \simeq 1.100$, and $F/F_{flu}(c = 0.20) \simeq 1.076$, thereby ensuring that the system finds itself in the flutter regime in all the three considered cases. Note that the three dimensionless damping coefficients given above correspond to the physical values (Table 1)

$$c = 0.05 \times 10^{-3}\ \mathrm{pN\,\mu m\,s^{-1}}, \qquad c = 0.10 \times 10^{-3}\mathrm{pN\,\mu m\,s^{-1}},$$
$$c = 0.20 \times 10^{-3}\mathrm{pN\,\mu m\,s^{-1}}. \tag{91}$$

It is observed that, for increasing values of the damping parameter from $c = 0.05$ to $c = 0.20$, the constant position around which the cart tends to oscillate increases and is reached at earlier times. Hence, the cart covers longer distances in shorter times, but then starts being confined at earlier times, see the X_c-t curves in the left panel of Fig. 8. Note that the curve corresponding to $c = 0.10$ (marked with circles) in Fig. 8 is the same as the curve marked with circles in Fig. 6(a), but plotted over the 'stretched' time window [0 s, 14 s] to emphasize the presence of a 'plateau' (we recall that this is an average plateau, about which the cart undergoes two-scale micro-oscillations). Also in the current set of simulations, the phase portraits of θ_1 and θ_2 (see the right panel of Fig. 8) exhibit quasi-periodicity, which seems to be a robust feature of the system under consideration, and an increasing clustering of the orbits for increasing value of the dimensionless damping coefficient.

5.3. Case II: the Maxwell–Lodge effect in the dynamics of the microrobot

We now consider Case II, in which the device is located outside the solenoid. To characterize the overall motion of the device, we examine the time evolution of the cart position. We analyze two placements: one on the left of the solenoid and one on the right, equidistant from the origin.

Fig. 9(a) illustrates the case in which the cart is positioned on the left of the solenoid. Each of the branches in Fig. 9(a) represents the motion of the cart for different initial conditions X_{c0}, with the upper branch (marked with circles) associated with $X_{c0} = -13.20\,\text{cm}$ and the lower branch (marked with squares) corresponding to $X_{c0} = -13.60\,\text{cm}$. We recall that outside the solenoid any initial position X_{c0} of the cart is of non-equilibrium and therefore Fig. 9(a) shows how the cart evolves, either moving away from the solenoid's boundary (curve marked with circles) or moving towards it (curve marked with squares). Moreover, even if the device is initially in a straight configuration, with $\theta_1(0) = \theta_2(0) = 0$ and $\dot{\theta}_1(0) = \dot{\theta}_2(0) = 0$, the Lorentz force acting on the skate generates an unbalanced torque that induces angular motion of the bars, ultimately leading to flutter, as discussed in Section 4.1. The observed dynamic behavior is argued to be a consequence of the Maxwell–Lodge effect, according to which, even in the absence of the magnetic induction field (see Remark 1 and Eqs. (16b), (19b) and (21)), the Lorentz force acting on the skate remains non-null.

In addition, both mean positions of the cart — one with initial position at $-13.20\,\text{cm}$ (circles) and the other at $-13.60\,\text{cm}$ (squares) — tend asymptotically toward a position at approximately $-13.38\,\text{cm}$, about which they oscillate. In view of this behavior, and with a slight abuse of terminology, we refer to the point $(-13.38\,\text{cm}, 0.00\,\text{cm})$ as an 'attractor'. Complementary to the trajectories of the cart X_c converging to the attractor, Figs. 9(d) and 9(e) also present the phase portraits of the angles θ_1 and θ_2 when the cart is at the attractor, together with a zoomed-in view of the cart displacement and the trajectory of point D. The dynamical regime in which the device now operates, as observed from the phase portraits, appears to lead to limit cycles. This is further illustrated in the zoomed-in view of X_c, where no micro-oscillations are observed to disturb the motion. We believe that, in this case, the Lorentz force acting at the tip of the pendulum is the dominant contribution.

Analogous considerations apply to Fig. 9(b), although the opposite behavior is observed. For symmetry, we place the cart at two initial positions near the point $(13.38\,\text{cm}, 0.00\,\text{cm})$, on the right-hand side of the solenoid: $X_{c0} = 13.36\,\text{cm}$ (corresponding to the curve marked with circles) and $X_{c0} = 13.41\,\text{cm}$ (corresponding to the curve marked with squares). The mean trajectories of the cart are now repelled from this point: the one with initial position $X_{c0} = 13.36\,\text{cm}$ moves back toward the solenoid, whereas the one with initial position $X_{c0} = 13.41\,\text{cm}$ moves away from it. Accordingly, we refer to the point $(13.38\,\text{cm}, 0.00\,\text{cm})$ as a 'repeller'.

Consistent with the discussion above, we emphasize that the device may also undergo backward motion in order to approach the 'attractor' or move away from the 'repeller', as shown in Fig. 9. Such behavior is not achievable in the problem studied by Cazzolli et al. (2020).

Sensitivity to the initial position of the skate. It is also informative to examine the post-critical behavior of the system in Case II when the initial position of the device is such that $x_{D2}(t = 0) \neq 0$, that is, with the skate located away from the x_1-axis, Fig. 10. To attain this initial configuration, $\theta_1(t = 0) = \pi/8$ and $\theta_2(t = 0) = \pi/4$ are selected, which yield $x_{D2}(t = 0) = 10.8979\,\mu\text{m}$. The effects of this different initial data are examined by comparing the simulation for $x_{D2}(t = 0) = 10.8979\,\mu\text{m}$ (right panel of Fig. 10) with the simulation for $x_{D2}(t = 0) = 0\,\mu\text{m}$ (left panel of Fig. 10). After a relatively short transient of about 20 time steps, corresponding to 0.02 s and during which the initial skate position affects the response, the skate exhibits qualitatively similar behavior in both simulations. By contrast, marked differences appear in the phase portraits of θ_1 and θ_2 during the transient, although these differences vanish at sufficiently long times.

6. Discussion and conclusions

A mechanical structural system has been proposed and analyzed that is capable of generating propulsion from an applied conservative force and a magnetic field by exploiting flutter instability and Hopf-type bifurcations. The system provides a simple model of a microrobot suitable for operating in magnetically controlled environments, without relying on conventional propulsion mechanisms. Note that, when viscosity is absent, the sole responsible for the variation of energy is the electric part of the Lorentz force. When the latter is switched off, the system becomes conservative.

Our design has coupled a Ziegler double pendulum with a movable cart subjected to a dead load and to an electrically charged nonholonomic constraint. Electromagnetic interactions provide a Lorentz force applied on the constraint when placed either inside or outside an ideal solenoid. Our setup differs from previously analyzed devices based on electric dipoles or magnetic torques (Alouges et al., 2015).

An important outcome of the presented theoretical framework is that the Maxwell–Lodge effect (Lodge, 1889; Rousseaux et al., 2008) can arise in systems such as the microrobot considered here. Given its fundamental relevance in both theoretical and experimental physics — Rousseaux et al. (2008) describe it as the *'classical equivalent'* of the *'Aharonov–Bohm effect [...] within quantum physics'* — the effect has been re-examined in the present setting, with particular attention to its influence on the device dynamics.

Two 'virtual' experimental configurations, denoted Case I and Case II and formulated as dedicated Cauchy problems, have been introduced as potential benchmarks for future studies of the post-critical dynamics of related systems. The magnetic induction was set to $B_M = 1\,\text{T}$, a value attainable in MRI-based and electron-beam experiments and sufficiently large for the Lorentz force to be comparable with the dead load F typically considered in microrobotic Ziegler double pendulum models. A systematic analysis for smaller values of B_M would be desirable to further delineate the range of validity of the present results. In this respect, the study reported in Fig. 7 represents a first step in this direction.

The analysis shows that the Lorentz force acting outside the solenoid, generated solely by the induced electric field, may either attract or repel the microrobot depending on whether its initial position lies below or above a critical distance from the solenoid boundaries.

For selected frequencies of the magnetic induction field, the device also exhibits confinement, with the cart oscillating about a position determined by the system parameters. Because the magnetic induction levels considered are, at most, comparable with those used in human-safe medical procedures such as MRI, this confinement mechanism could be exploited in biomedical applications, for instance to enhance localized drug delivery. The desired confinement position could be

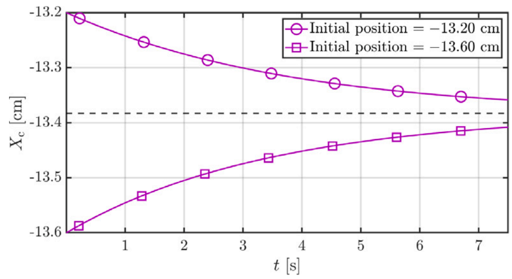

(a) Time history of X_c, for Ω = 10 kHz, when the cart is placed outside of the solenoid on its left, at a position of −13.20 cm (circles) and −13.60 cm (squares).

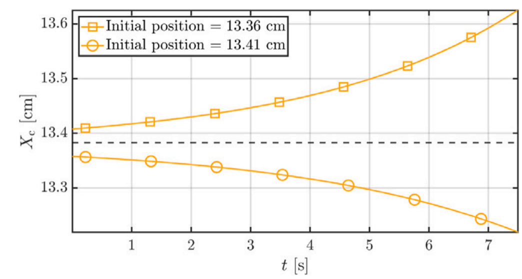

(b) Time history of X_c, for Ω = 10 kHz, when the cart is placed outside of the solenoid on its right, at a position of 13.36 cm (circles) and 13.41 cm (squares).

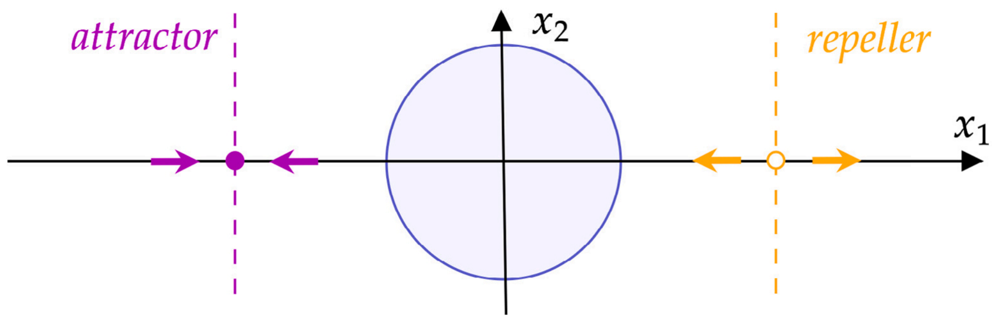

(c) Graphical depiction of the 'attractor' point and 'repeller' point. The picture is not in scale.

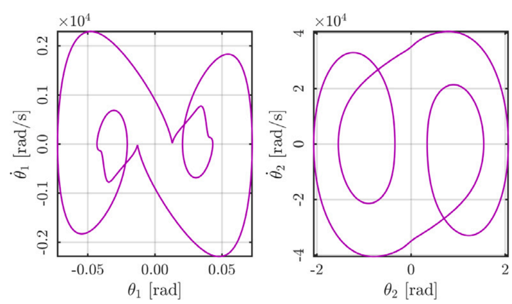

(d) Phase plots of θ_1 and θ_2, at when the device is placed at the point attractor (−13.38 cm, 0.00 cm).

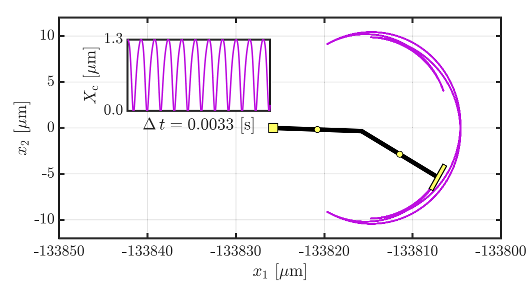

(e) Trace of the position of D alongside the cart oscillations (zoomed section) at the point attractor (−13.38 cm, 0.00 cm).

Fig. 9. Time history of X_c (a) and (b), picture of the 'attractor' and 'repeller' points (c), phase portraits of θ_1 and θ_2 (d), and trajectory of the point D (e) for the parametric study of Case II and representing the dynamic motion induced by flutter instability on a movable double pendulum with electrically charged nonholonomic constraint, embedded in a magnetic field.

determined through an inverse-design procedure and then used as the target location for topical drug release.

The present study aims to contribute to the analysis of the stability of microrobots and of structures inspired by the Ziegler double pendulum, particularly when interactions beyond purely mechanical effects are taken into account. Such analysis, of course, should be accompanied by dedicated experiments, which, however, we have not designed yet. Indeed, at the moment, we have no experimental evidences that can corroborate or confute the predictions reported in our work. However, we are thinking of possible experiments of the system studied in our work, which could stimulate further research in the field. For the time being, our results may hopefully provide a reference for investigations based on experimental set-ups that are 'richer' than those concerning purely mechanical phenomena (see, e.g., Dreyfus et al., 2005; Alouges et al., 2015; Shen et al., 2023; Boiardi and Noselli, 2024).

CRediT authorship contribution statement

Andrea Pastore: Writing – review & editing, Writing – original draft, Visualization, Validation, Software, Methodology, Investigation, Formal analysis, Data curation, Conceptualization. **Joel C. Harrop:** Writing – review & editing, Writing – original draft, Visualization, Validation, Software, Methodology, Investigation, Formal analysis, Data curation, Conceptualization. **Davide Bigoni:** Writing – review & editing, Writing – original draft, Visualization, Validation, Supervision, Software, Resources, Project administration, Methodology, Investigation, Funding acquisition, Formal analysis, Data curation, Conceptualization. **Alfio Grillo:** Writing – review & editing, Writing – original draft, Visualization, Validation, Supervision, Software, Resources, Project administration, Methodology, Investigation, Funding acquisition, Formal analysis, Data curation, Conceptualization.

Use of generative Artificial Intelligence (AI)

The authors have *not* used any generative AI tool for writing this work.

Declaration of competing interest

The authors declare that they have no known competing financial interests or personal relationships that could have appeared to influence the work reported in this paper.

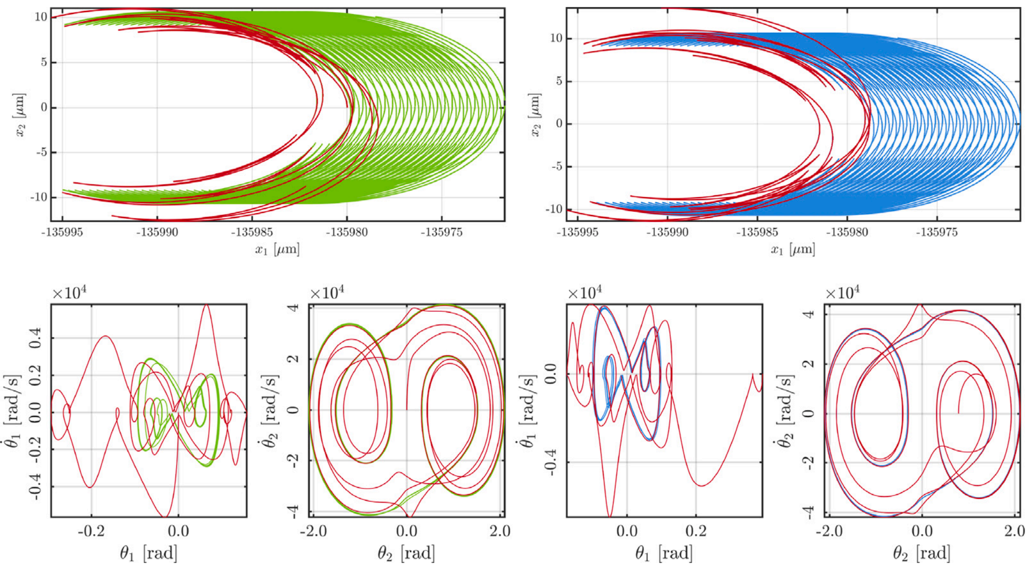

Fig. 10. Path traced by a non-slipping skate positioned at the end of the pendulum alongside its phase plots for two simulations with the device situated outside of the solenoid. (Left panel) The three images on the left refer to a simulation carried out with the initial conditions $\mathsf{Y}_0 = \{0\ 0\ -13.6\,\text{cm}\ 0\ 0\ 0\}^T$. Since the initial angles of the two bars are both zero, $x_{D2}(t=0)=0$. (Right panel) The three images on the right refer to a simulation carried out with the initial conditions $\mathsf{Y}_0 = \{\pi/8\ \pi/4\ -13.6\ \text{cm}\ 0\ 0\ 0\}^T$. Since the initial angles are $\theta_1(t=0)=\pi/8$ and $\theta_2(t=0)=\pi/4$, $x_{D2}(t=0)=10.8979\,\mu\text{m}$. In both cases the first 20 time steps (0.02 s) are highlighted in red showing the transient phase.

Acknowledgments

A.P. and A.G. have been partially funded by the research project 'Innovative multiscale approaches, possibly based on Fractional Calculus, for the effective constitutive modeling of cell mechanics, engineered tissues, and metamaterials in Biomedicine and related fields', PRIN PNRR P2022KHFNB. D.B. and J.H. acknowledge financial support from the European Research Council (ERC) under the European Union's Horizon Europe research and innovation programme (Grant agreement No. ERC-ADG-2021-101052956-BEYOND). The methodologies developed in this work fall within the aims of the GNFM (Gruppo Nazionale per la Fisica Matematica) of the INDAM (Istituto Nazionale di Alta Matematica).

Appendix A. Supplementary data

Supplementary material related to this article can be found online at https://doi.org/10.1016/j.apples.2026.100345.

Data availability

No data was used for the research described in the article.

References

Agúndez, A., García-Vallejo, D., Freire, E., 2021. Linear stability analysis of nonholonomic multibody systems. Int. J. Mech. Sci. 198, 106392.

Alouges, F., De Simone, A., Giraldi, L., Zoppello, M., 2015. Can magnetic multilayers propel artificial microswimmers mimicking sperm cells? Soft Robot. 2, 117–128.

Ashcroft, N., Mermin, N., 1976. Solid State Physics. Holt-Saunders.

Bentvelsen, B., Lazarus, A., 2018. Modal and stability analysis of structures in periodic elastic states: application to the Ziegler column. Nonlinear Dynam. 91, 1349–1370. http://dx.doi.org/10.1007/s11071-017-3949-4.

Bigoni, D., Kirillov, O. (Eds.), 2019. Dynamic stability and bifurcation in nonconservative mechanics. In: CISM International Centre for Mechanical Sciences, vol. 586, Springer International Publishing, Cham.

Bigoni, D., Noselli, G., 2011. Experimental evidence of flutter and divergence instabilities induced by dry friction. J. Mech. Phys. Solids 59, 2208–2226.

Boiardi, A.S., Noselli, G., 2024. Minimal actuation and control of a soft hydrogel swimmer from flutter instability. J. Mech. Phys. Solids 191, 105753. http://dx.doi.org/10.1016/j.jmps.2024.105753.

Brown, A.T., Poon, W.C.K., 2014. Ionic effects in self-propelled pt-coated janus swimmers. Phys. Chem. Chem. Phys. 16, 2446–2458.

Cazzolli, A., Dal Corso, F., Bigoni, D., 2020. Non-holonomic constraints inducing flutter instability in structures under conservative loadings. J. Mech. Phys. Solids 138, 103919.

D'Annibale, F., Rosi, G., Luongo, A., 2015. Controlling the limit-cycle of the Ziegler column via a tuned piezoelectric damper. Math. Probl. Eng. 2015, 1–9.

Dreyfus, R., Baudry, J., Roper, M.L., Fermigier, M., Stone, H.A., Bibette, J., 2005. Microscopic artificial swimmers. Nature 437, 862–865.

Felsager, B., 1998. Geometry, particles, and fields. Springer.

Gantmacher, F., 1975. Lectures in Analytical Mechanics. MIR Publishers, Moscow.

Guillot, L., Lazarus, A., Thomas, O., Vergez, C., Cochelin, B., 2020. A purely frequency based Floquet-Hill formulation for the efficient stability computation of periodic solutions of ordinary differential systems. J. Comput. Phys. 416, 109477. http://dx.doi.org/10.1016/j.jcp.2020.109477.

Guskov, M., Thouverez, F., 2012. Harmonic balance-based approach for quasi-periodic motions and stability analysis. J. Vib. Acoust. 134, 031003. http://dx.doi.org/10.1115/1.4005823.

Haller, K., 1987. Quantum electrodynamics in the temporal gauge. Phys. Rev. D 36, 1830–1838.

Katzmeier, F., Simmel, F.C., 2023. Microrobots powered by concentration polarization electrophoresis (cpep). Nat. Commun. 14.

Kim, Y., Parada, G.A., Liu, S., Zhao, X., 2019. Ferromagnetic soft continuum robots. Nature 573, 82–87.

Kirillov, O., 2010. Structural optimization of the ziegler's pendulum: singularities and exact optimal solutions.

Kirillov, O., 2013. Nonconservative stability problems of modern physics. In: De Gruyter Studies in Mathematical Physics, vol. 14.

Kirillov, O., Verhulst, F., 2010. Paradoxes of dissipation-induced destabilization or who opened Whitney's umbrella? ZAMM - J. Appl. Math. Mech. / Z. Angew. Math. Mech. 90, 462–488.

Kuznetsov, Y.A., 2023. Elements of applied bifurcation theory, fourth ed. In: Applied Mathematical Sciences, vol. 112, Springer Cham.

Lanczos, C., 1970. The Variational Principles of Mechanics. Dover Publications, Inc. New York.

Lodge, O., 1889. On an electrostatic field produced by varying magnetic induction. Proc. Phys. Soc. Lond. 10, 116–128.

Martel, S., et al., 2007. MRI-based medical nanorobotics: the modulation of magnetic gradients for propulsion and navigation of ferromagnetic core nanocapsules. Appl. Phys. Lett. 90, 114105.

Maruskin, J., Bloch, A., Marsden, J., Zenkov, D., 2012. A fiber bundle approach to the transpositional relations in nonholonomic mechanics. J. Nonlinear Sci. 22, 431–461.
Montgomery, D.B., 1969. Solenoid Magnet Design: The Magnetic and Mechanical Aspects of Resistive and Superconducting Systems. Wiley-Interscience, New York.
Neimark, J., Fufaev, N., 1972. Dynamics of Nonholonomic Systems. American Mathematical Society, Rhode Island.
Pars, L.A., 1965. A Treatise on Analytical Dynamics. Heinemann, London.
Pastore, A., Giammarini, A., Grillo, A., 2024. Reconciling Kozlov's vakonomic method with the traditional non-holonomic method: solution of two benchmark problems. Acta Mech. 235, 2341–2379.
Rousseaux, G., Kofman, R., Minazzoli, O., 2008. The Maxwell-Lodge effect: significance of electromagnetic potentials in the classical theory. Eur. Phys. J. D 49, 249–256.
Shampine, L., Reichelt, M., 1997. The MATLAB ODE suite. SIAM J. Sci. Comput. 18.
Shen, H., Cai, S., Wang, Z., Ge, Z., Yang, W., 2023. Magnetically driven microrobots: Recent progress and future development. Mater. Des. 227, 111735.
The MathWorks, Inc., 2024. MATLAB. MathWorks, Natick, Massachusetts, Version R2024b.
Wang, X., Fan, C., Yang, S., Yang, Z., Yang, Y., Sinapius, M., 2024. Flutter instability characteristics and mechanisms of Ziegler double pendulum with arbitrary masses, stiffness and damping. Nonlinear Dynam. 112, 20771–20792.
Xu, T., Duncan, C.J.R., Denham, P., Schaap, B.H., Kulkarni, A., Garcia, D., Anderson, S.D., Musumeci, P., England, R.J., 2025. Focusing of relativistic electron beams with permanent magnetic solenoid. Phys. Rev. Accel. Beams 28, 082401.
Xu, R., Xu, Q., 2024. A survey of recent developments in magnetic microrobots for micro-/nano-manipulation. Micromachines 15, 468.
Zampieri, G., 2000. Nonholonomic versus vakonomic dynamics. J. Differential Equations 163, 335–347.
Zhang, L., Peyer, K.E., Nelson, B.J., 2009. Artificial bacterial flagella: Fabrication and magnetic control. Nano Lett. 9, 3663–3667.
Ziegler, H., 1977. Principles of Structural Stability, Lehr- und Handbücher der Ingenieurwissenschaften. Birkhäuser Basel.